ADDITIVE MANUFACTURING OF

MULTI-FUNCTIONAL SOFT ACTIVE DEVICES

By

DAEHOON HAN

A dissertation submitted to the

School of Graduate Studies

Rutgers, The State University of New Jersey

In partial fulfillment of the requirements

For the degree of

Doctor of Philosophy

Graduate Program in Mechanical and Aerospace Engineering

Written under the direction of

Howon Lee

And approved by

_____

_____

_____

_____

_____

New Brunswick, New Jersey

January, 2020

ABSTRACT OF THE DISSERTATION

Additive Manufacturing of Multi-Functional Soft Active Devices

by DAEHOON HAN

Dissertation Director:

Howon Lee

Unique functions of living organisms in nature inspire a broad spectrum of engineering systems. Since biological living systems are often composed of multiple soft active materials with micro-scale three-dimensional (3D) structures, fundamental understanding on soft active materials and development of micro 3D manufacturing techniques are essential for effective implementations of their characteristics and functionalities. Hydrogels are soft polymeric materials that undergo volumetric changes upon solvent absorption. Some hydrogels exhibit such changes in response to external environmental conditions, such as temperature, pH, light, magnetic field, electric field, and chemical triggers, which are referred to as stimuli-responsive hydrogels. They have played an important role in a variety of applications, such as soft robotics, soft electronics, and biomedical engineering. Despite the growing attention to stimuli-responsive hydrogels and their diverse applications, manufacturing techniques for stimuli-responsive hydrogels have

been limited to simple two-dimensional (2D) fabrication methods which restrict full utilization of their unique material behavior.

This dissertation focuses on the development and application of a high-resolution multi-material 3D digital fabrication technology, multi-material projection micro-stereolithography (MM-PμSL), in order to engineer stimuli-responsive hydrogels into 3D multi-functional soft active devices. Specifically, it consists of development of MM-PμSL, studies of fundamental physics for various stimuli-responsive hydrogels, including electroactive hydrogels, thermo-responsive hydrogels, and photo-active hydrogels, micro 3D printing of stimuli-responsive hydrogels, and development of multi-functional soft active devices, such as soft robots actuated by temperature changes or electric fields, and light-driven camouflage skin.

ACKNOWLEDGEMENTS

deeply grateful to my beautiful wife, Eun Youp Rha, for her tremendous love. All of my achievements and honors during my Ph.D. program came from her sacrifice, support, and dedication, for which I am indebted forever.

Finally, I give thanks to God. I am so grateful that my Father shepherd my whole life and walk with me as He always did, does, and will. I believe that He always has much better plans than me, and I sincerely hope that I will live my life according to His will. "I thank Christ Jesus our Lord, who has given me strength, that he considered me trustworthy, appointing me to his service."

TABLE OF CONTENTS

6.2. Future work

LIST OF TABLES

Chapter 1

Introduction

1. Introduction

1.1. Background and motivation

Soft materials, including polymers, colloids, granular materials, liquid crystals, and a number of biological materials, are types of materials that can be easily deformed or structurally altered by thermal, chemical, mechanical, or other environmental conditions. Soft materials have been receiving a great deal of attention in a wide range of science and engineering fields, for instance, tissue engineering, drug delivery, biomedical devices, microfluidics, optics, stretchable electronics, and soft robotics, because of their unique characteristics, such as multi-functionality, adaptability, flexibility, lightweight, and biocompatibility.

Hydrogels, one of the well-known soft materials, are polymeric networks that undergo abrupt changes in volume upon solvent absorption [1]. The hydrogel networks retain the hydrophilic nature of the polymer chains, but the physical or chemical crosslinking of the chains restrains the hydrogel from dissolving in water. Water molecules can penetrate in between the polymer chains, which causes large swelling and formation of hydrogels. Hydrogels show physical properties similar to living tissue due to their high water content, porosity, soft consistency, and low interfacial tension with water or biological fluids, which results in appealing to biological and biomedical applications, such as tissue engineering [2], drug delivery [3], and bio-nanotechnology [4].

Some hydrogels exhibit conformational and chemical changes in response to external environmental conditions, such as temperature [5-7], pH [3, 6, 7], light [8, 9],

magnetic field [10], electric field [11], and chemical triggers [12], similar to living systems. These hydrogels are referred to as stimuli-responsive hydrogels [13] or smart hydrogels [14]. The stimuli-responsive properties of hydrogels are mainly comprised of polymer-polymer and polymer-solvent interaction [15]. Specifically, the fundamental interactions are ionic interactions [16], hydrophobic interactions [17], hydrogen bonding [18], and van der Waals forces [19]. These interactions occur either independently or simultaneously to exhibit stimulus-responsive behavior of hydrogels. Such distinct properties lead stimuli-responsive hydrogels to play an important role as the materials for a variety of applications, such as smart and self-healing coatings, bio-interfaces and bio-separation, micro- and nano-actuation, and sensors [13].

Despite the growing attention to stimuli-responsive hydrogels and their diverse applications, manufacturing techniques for stimuli-responsive hydrogels have been limited to simple two-dimensional (2D) fabrication methods, such as cutting, molding, and lithography, which hinders full utilization of their unique material behavior. Thus, three-dimensional (3D) fabrication of stimuli-responsive hydrogels will suggest new opportunities to develop and improve devices and applications based on new features that have not been realized with existing technologies to date. For example, living creatures that have complex 3D micro-structures made of multiple soft active materials can be the actual sources inspiring engineering of functional materials. It will be fascinating to observe how certain living creatures seemingly perform their tasks that look impossible; for instance, binding of gecko's feet to various surfaces, manipulation of octopus's arm with almost unlimited degree of freedom, generation of color of butterfly's wing without

pigments, etc. Therefore, fabrication and control of soft active materials in the 3D space is critical for implementing such novel features of living creatures.

Some efforts have been put on creating a 3D structure from a 2D stimuli-responsive hydrogel sheet using an origami approach [20-24]. However, achieving a complex, high resolution, and high aspect ratio geometry using stimuli-responsive hydrogels still remains challenging. More recently, additive manufacturing (AM), also known as 3D printing, of stimuli-responsive hydrogels has been examined. The Lewis group reported the 3D shape-morphing systems with composite hydrogel structures that are encoded with localized, anisotropic swelling behavior controlled by the alignment of cellulose fibrils [25]. The Spinks group demonstrated a 3D printed thermo-responsive valve, fabricated with temperature sensitive hydrogel, for control of water flow according to water temperature [26]. The Nelson group also presented 3D printing of triple stimuli-responsive hydrogel that respond to three different stimuli, temperature, pressure, and UV light [27]. These studies have contributed to developing more complex and higher resolution of 3D stimuli-responsive hydrogel devices and various applications, using such 3D devices. However, since the AM technologies have been designed to produce structures from a single material, they are still limited in implementing a wider range of functionalities inspired by multiple soft materials of living creatures. Therefore, multi-material fabrication in 3D space with soft materials is necessary for achieving multi-functional soft devices.

1.2. Recent advances in multi-material additive manufacturing

AM refers to a set of manufacturing processes where 3D objects are produced by directly joining constituent materials, often in a layer-by-layer manner. Each layer representing a thin cross-section of the object is digitally derived from a 3D computer-aided design (CAD) model and physically created by adding raw materials directly at the desired location. Since its first invention in 1984 [28], the focus of AM has long been on quickly creating a part representation before final release or commercialization, or rapid prototyping. However, the remarkable advances in AM technologies and materials development in the past few years have shifted the paradigm of AM to direct manufacturing of end products. In addition to its traditional use in automotive, aerospace and defense, with the fast-growing demands for product customization and personalization, AM is rapidly expanding its footprint to new areas including medical, dental, and consumer electronics, to name a few [29, 30].

Individual AM processes differ depending on the machine technology and material used. While AM for metals and ceramics holds its own significance for its industrial applications, polymers have been dominant AM materials due to wide material selection, processing methods available, and broad spectrum of materials properties achievable. Furthermore, employing new functional polymers with novel physical, chemical, mechanical, and biological properties, new branches of AM has also emerged, such as bio-printing [31, 32] and four-dimensional (4D) printing [25, 33, 34]. Figure 1.1 shows several major AM techniques including direct ink writing (DIW), fused deposition modeling (FDM), material jetting (MJ), stereolithography (SLA), and digital light processing (DLP). In DIW, a viscous material in a material container (usually syringe) is extruded through a nozzle which moves in a programmed way in 3D space to build a 3D object. In FDM, a

thermoplastic polymer is continuously supplied as a filament into a heated nozzle through which a melted polymer is extruded in 3D, followed by subsequent cooling and solidification. MJ uses an array of individually addressable printhead nozzles to deposit fine droplets of a photo-curable polymer resin, which are cured with UV light upon arrival on the substrate. These three techniques typically use three-axis translational motion control to transfer the materials selectively to desired volume elements of a 3D object. In contrast, SLA and DLP deliver light energy to a liquid-state photo-curable polymer in a vat to create a solid part. In SLA, a laser beam is directed to a spot on a photo-curable resin and raster-scanned point-by-point, while DLP projects a patterned UV light generated by a digital dynamic mask to solidify an entire layer.

Most of initially developed AM techniques print an object with a single material only. However, the demand for high complexity and enhanced functional performance of 3D printed objects has raised tremendous interest in development of multi-material additive manufacturing (MMAM) technique. By integrating different materials together in one object, one can rapidly manufacture an object with a wide range of properties and functionalities (e.g., mechanical, electrical, chemical, optical). Many MMAM technologies have been recently developed and actively used in various fields. Since material processing principle varies for each AM method, different approaches have been taken for MMAM depending on the base AM technique used. Herein, we review the latest MMAM techniques based on DIW, FDM, MJ, SLA, DLP, and hybrid methods employing multiple AM methods simultaneously. We also review key applications enabled by MMAM in three areas of growing interest; biomedical engineering, soft robotics, and electronics.
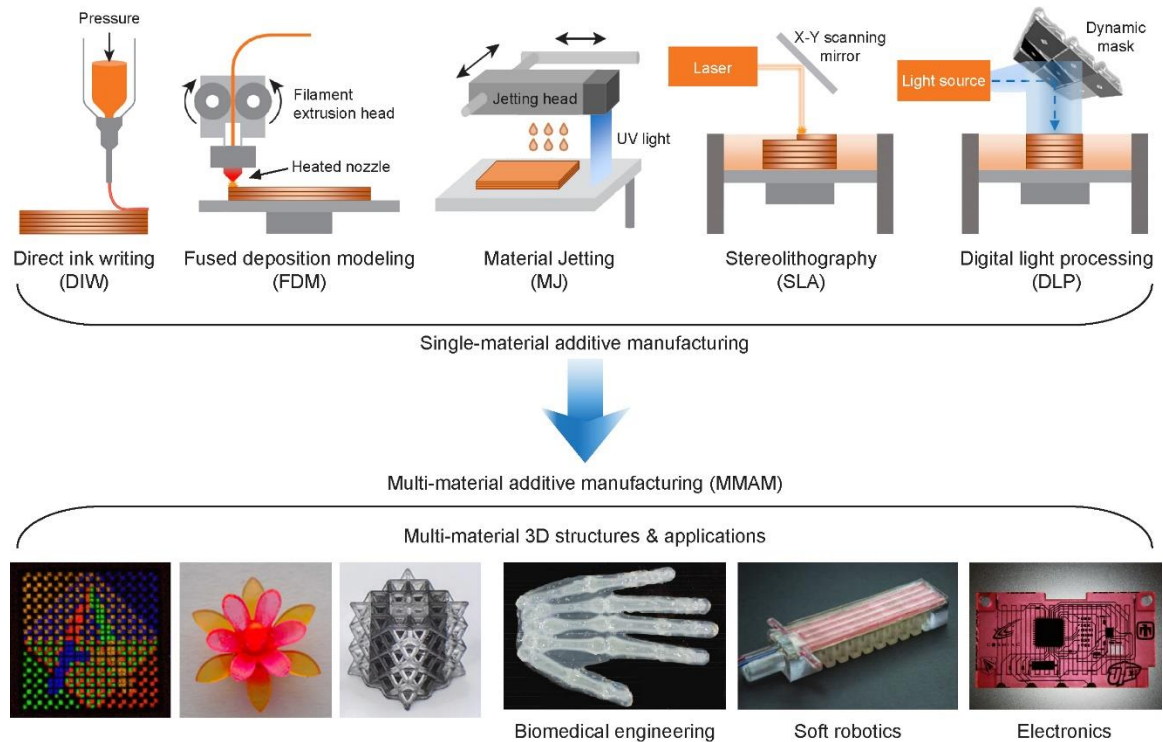
Figure 1.1. Schematics of five different additive manufacturing techniques including direct ink writing (DIW), fused deposition modeling (FDM), material jetting (MJ), stereolithography (SLA), and digital light processing (DLP). Schematic images adapted from [30]. Multi-material additive manufacturing (MMAM) enables direct manufacturing of multi-material 3D structures for applications in many areas, including biomedical engineering, soft robotics, and electronics. Images are from [42, 55, 60, 62, 65, 77].

1.2.1. Multi-material additive manufacturing methods

1.2.1.1. Direct ink writing

The simplest method to realize MMAM is to add as many printing nozzles as the number of materials used in a DIW platform (Figure 1.2(a)). This method provides a simple and easily accessible printing process with access to a wide range of materials, including structural [35, 36], electrical [37, 38], and biological [32, 39] materials. However, this approach often involves sequential printing process for individual materials, which slows down overall printing process. It also requires a careful alignment for each nozzle as well as precise material flow control, especially when printing materials have different rheological properties. To address these issues, single nozzle designs with multiple material containers have been developed for continuous printing with multiple materials [40-42]. A microfluidic printhead [40] and some nozzle designs including a material mixer before the nozzle [41, 42] have been proposed to rapidly switch between materials within a single nozzle. The material mixer also allows for printing of a mixture of different materials. Furthermore, a mixing ratio can be varied to desired concentration by precise material flow control through individual pressure lines, which enables 3D printing of functionally gradient materials with a tailored property (e.g., mechanical, chemical). High cross-contamination between materials going through the same nozzle is still a challenge to be addressed.

1.2.1.2. Fused deposition modeling

In the earlier stage of FDM, the printing potential was limited by a small selection of thermoplastic filament materials. With increasing variety of filament materials offering a wide range of physical, mechanical, and electronic properties [43], MMAM with FDM draws growing interest. In addition, multi-material printing capability for FDM is essential to print sacrificial support structures for printing parts with overhang features. Similar to multi-material DIW technology, multi-material FDM is easily achieved by employing multiple extrusion heads where nozzle temperature, printing speed, and resolution can be individually control as necessary [44]. Due to the expiration of the major FDM patents in the early 2010s, multi-head FDM systems has become relatively affordable and accessible compared to other MMAM techniques [45]. However, some drawbacks of multi-head FDM still exist, such as inherent poor surface finish with ridges, limited printing resolution, slow build speed, and low interfacial bonding strength. In particular, low interfacial bonding is a critical issue in producing 3D parts with dissimilar materials. Recently, a bi-extruder head, which can print two filaments through a single nozzle, has been reported (Figure 1.2(b)) [46]. This bi-extruder includes an intermixer having thick blades, creating passive mixing of two melted filaments. The mixing also enabled printing of functionally gradient materials as well as improving interfacial bonding strength between two different materials by enhancing the mechanical interlocking of the materials at the interface. Printing with a filament coated with carbon nanotubes (CNTs) and microwave heating after printing has been shown to enhance interfacial bonding, but it has not been applied to bond different materials [47]. Other shortcomings inherited from FDM such as poor surface

finish and limited printing resolution still need to be overcome to improve 3D printed part quality.

1.2.1.3. Material jetting

MJ 3D printing is derived from the conventional inkjet printing technology where printing with multiple inks with different colors is already well established. Therefore, multi-material printing with MJ has been easily implemented following the same approach using multiple jetting heads [48, 49]. Instead of color inks, multiple photo-curable materials and support materials are processed through jetting heads. Each head has hundreds or thousands of nozzles, enabling a rapid 3D printing with parallel material deposition. Printing resolution is determined by the nozzle density in the jetting head, which is limited by current nozzle manufacturing techniques. To improve the printing resolution with a given nozzle density, a machine vision system has been employed to monitor the printing quality in real-time and provide a feedback to correct inaccuracies during printing process [50]. With this system, MMAM with MJ with ~35 μm resolution has been demonstrated (Figure 1.2(c)) [49]. Another challenge in multi-material MJ is the difficulty in processing materials having a viscosity higher than 40 cP due to the use of small inkjet nozzles. To overcome the problem, a piezoelectric actuated jetting system has been reported which can dispense materials having a viscosity range of 50 - 200,000 cP [51]. In this work, MMAM of electronics with a highly viscous conductive carbon paste and photo-curable polymers was demonstrated.

1.2.1.4. Stereolithography

Compared to other AM methods, SLA has many advantages including high printing resolution, high quality surface finish, and wide material selection. Since a part is created in a vat of a liquid photo-polymer, however, MMAM with SLA requires material exchange from one liquid to another in the vat. Due to this difficulty, SLA was not considered as a good candidate for MMAM until recently. The simplest MMAM with SLA is to manually change a liquid polymer in the vat [52]. However, manual material change is extremely laborious, interrupts the process for every material change, and therefore significantly reduces throughput. Hence, it is not practical for producing parts that require frequent material change. Later, a rotating vat carousel system was used to automate material change [53]. The system includes multiple vats for different materials mounted on a rotating platform. When material change is needed, the platform rotates to remove the current vat from the printing area and place another vat with a different material in the printing area. However, the material change step is still interruptive and takes the majority of the total printing time. Also, rinse-cleaning of a printing part between material change to prevent cross-contamination not only adds substantial process time but also increases material consumption. Recently, an aerosol jetting system has been employed in SLA to directly supply different materials (Figure 1.2(d)) [54]. The aerosol system has multiple material containers and atomizers that transform liquid material into small droplets. The droplets are deposited at desired locations and locally cured with a UV laser, resulting in higher material efficiency. However, the time-consuming material deposition process further adds printing time to SLA which already suffers from slow raster scanning. MMAM has been

also achieved at micro-scale using two-photon laser stereolithography combined with a microfluidic chamber that supplies multiple materials [55].

1.2.1.5. Digital light processing

While having the same advantages of SLA, DLP provides higher printing speed by using a scanning-free projection lithography. Many innovative AM methods have been recently developed based on DLP technology for rapid, layer-free, and scalable AM [56-58], but they are still limited to one material. Various attempts have been made to achieve MMAM with DLP with different material change methods such as a rotational platform [59, 60] or a microfluidic material delivery system [61]. However, these methods also require a time-consuming cleaning process, which slows down the overall printing speed. To reduce the cleaning time, a vat-free, droplet-based MMAM with an air jet blower was developed (Figure 1.2(e)) [62]. In this method, printing materials are supplied as an array on droplets. Once a layer is cured, the remaining liquid drop is rapidly blown away from the printing area using a high-pressure air jet. Next droplet to be supplied may be of different material as needed. On the other hand, conceptually different approaches for DLP MMAM have been also reported. Using orthogonal photo-chemistries that undergo independent cross-linking reactions (radical and cationic crosslinking), multiple polymers that are mixed in the same vat were selectively cured using light with different wavelengths without the need for physical material change [63]. The radical curing takes place by both blue light (470 nm) and green light (530 nm), whereas cationic curing occurs only by blue light. By selectively projecting images with two wavelengths of light, printing of multi-material 3D objects with predefined and spatially resolved mechanical and chemical properties can be

effectively achieved. The same principle has been also used for multi-material 4D printing [64].

1.2.1.6. Hybrid additive manufacturing

Each AM technique has its own advantages and disadvantages, and the range of materials available is different. To compensate for the shortcomings of each AM system and to use a wider variety of materials for multi-material 3D objects, two or more complimentary AM methods can be incorporated into a single AM system. DIW was the most widely used method that is combined with other AM method due to its simplicity. Since DIW is suitable for printing relatively high viscous materials, it has been used with other AM techniques where processing high viscous materials is challenging. For example, hybrid AM techniques combining DIW with MJ [65] or DLP [66] have been developed to fabricate electronics that require printing of high viscous conductive materials containing high concentrations of metal particles or carbon-based materials. DIW has also been used together with a vacuum nozzle to integrate electronic components via a pick-and-place method [67]. Pre-fabricated surface mount electrical components, including light emitting diodes (LEDs), registers, and capacitors, were placed on target positions using a vacuum nozzle, followed by printing conductive materials with DIW to create electrical interconnects. Recently, more AM methods including DIW, FDM, and MJ and two complementary techniques (robotic arms for pick-and-place and photonic curing system for intense pulsed light sintering) have been integrated into one system for multi-functional MMAM (Figure 1.2(f)) [68].
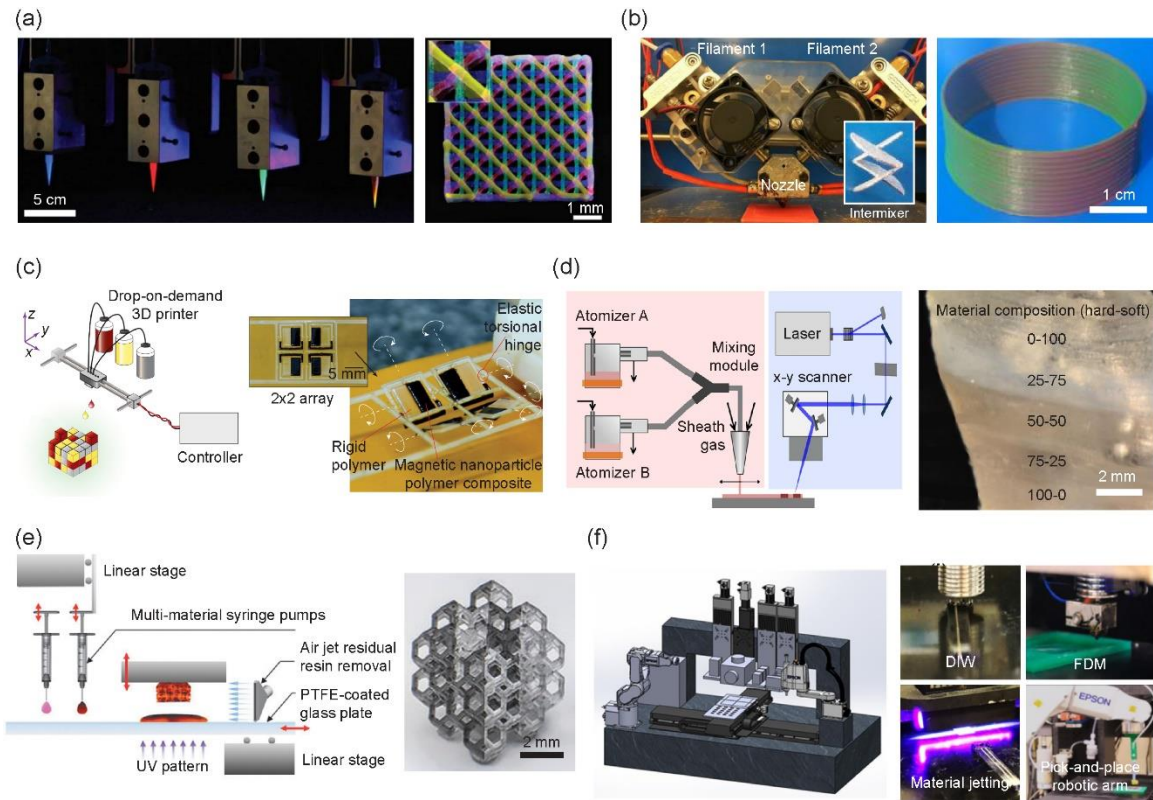
Figure 1.2. Recent advance in MMAM techniques. (a) Multi-material DIW using multiple nozzles (images adapted from [32]). (b) Multi-material FDM using a bi-extruder head which can print two filaments through a single nozzle (images adapted from [46]). (c) MJ-based MMAM with improved printing resolution through a machine vision system (images adapted from [49]). (d) Vat-free multi-material SLA using an aerosol jetting system (images adapted from [54]). (e) Vat-free DLP-based MMAM using air jet cleaning system (images adapted from [62]). (f) Hybrid MMAM system combining DIW, FDM, MJ, and two complementary techniques (robotic arms and photonic curing system) (images adapted from [68]).

1.2.2. Applications using multi-material additive manufacturing

1.2.2.1. Biomedical engineering

AM industry for biomedical application is projected to reach \$3.7 billion by 2026 [69]. With strong market potential, many biomedical applications have been developed with MMAM. Creating 3D engineered tissue constructs that mimic biological systems has attracted much attention in tissue engineering. Since natural tissues are structurally complex consisting of multiple cell types, MMAM is essential to create an engineered tissue construct. Recently, a 3D spinal cord tissue-like structure has been reported with 3D printing of neuronal and glial progenitor cells (Figure 1.3(a)) [39]. MMAM has also been used to create biomedical devices such as microneedle arrays [70] and diagnostic devices [71]. Typical transdermal microneedle arrays consist of two parts (microneedle bodies and a substrate) playing different roles (drug delivery or biofluid collection, structural support and skin protection) (Figure 1.3(b)). Therefore, using two materials having different properties improves the performance of microneedle arrays. Similarly, diagnostic microfluidic devices for measuring pharmaceuticals in biological fluids with multiple functional parts, including an optically transparent main body for visual detection, electrodes for electrokinetic transport, and membranes for screening target molecules, were fabricated using MMAM (Figure 1.3(c)). MMAM is also used for fabrication of 3D artificial models for preclinical or preoperative surgical training (Figure 1.3(d)) [72, 73]. With the printed models recapitulating various characteristics of different biological tissues in a body, complex operating procedures can be effectively planned for lowering the risk of errors during surgery.

1.2.2.2. Soft robotics

Soft robots are defined by their compliant and flexible body which enables complex actuations and motions that would not be possible to achieve with conventional robots with rigid bodies and joints [74]. AM has enabled the design and fabrication of sophisticated geometries and internal features required for soft robotic actuation by providing an excellent tool to fabricate a 3D mold for elastomeric materials or to directly manufacture them [75]. With the recent evolution of AM and rapid expansion of printable material sets, there has been a trend shifting towards direct manufacturing of soft robots using MMAM, which dramatically simplifies manufacturing procedures without compromising functional complexity. The first example is pneumatically driven elastomeric actuators, comprising an elastomeric body whose surface is decorated with a stiff reinforcing material aligned at a designed orientation through DIW (Figure 1.3(e)) [35]. The orientation of reinforcement determines the local anisotropic deformation developed throughout the soft actuators during inflation, resulting in a variety of motions such as elongation, contraction, and twisting. Printing-driven programming of reinforcement via DIW was also used to control complex swelling of a hydrogel for 4D printing [25]. MMAM also allows for direct integration of different functional components necessary for actuation. For example, DIW and MJ hybrid MMAM was used to print a silver-nanoparticle ink as a resistive heating element on a stimuli-responsive liquid crystal elastomer (LCE) that exhibits shape change with temperature for reversible soft robotic actuation (Figure 1.3(f)) [76]. Also, the same hybrid approach was used to directly print a stiffness-tunable soft actuator consisting of a soft elastomeric body connected with pneumatic system, a shape memory polymer (SMP) layer for stiffness control, and silver nanoparticle ink for resistive heating (Figure 1.3(g))

[65]. The SMP shows a capability of reversibly changing the stiffness by a few orders of magnitude spanning from MPa (at high temperatures) to GPa (at low temperatures) through glass transition [34]. By controlling pneumatic pressure and electric current independently, soft robotic actuation and passive locking are both possible, extending the capability of soft robot to higher load and more energy efficient applications.

1.2.2.3. Electronics

MMAM is critical for direct manufacturing of 3D electronic devices where electrically dissimilar materials including conductors, semiconductors, and dielectrics are integrated together. By adding the third dimension, 3D electronics can be further miniaturized to a smaller footprint and formfactor. For example, a 3D magnetic sensor with integrated electronic components and conductive paths has been 3D printed, demonstrating the improvement of volume utilization by taking full advantage of the design in all three dimensions (Figure 1.3(h)) [77]. Additional functionalities such as flexibility and stretchability can be also imparted in electronics by employing various printable materials. Stretchable strain or pressure sensors have been created with MMAM of thermoplastic polyurethane as a matrix and thermoplastic polyurethane with silver flakes as a conductive material [67]. Recently, a highly stretchable electronic LED board has been demonstrated by printing a stretchable conductive hydrogel on elastomer (Figure 1.3(i)) [78]. Given stretchability of hydrogel up to 1300%, the electric circuit can maintain electric conductivity even under large deformation. In addition, the freeform fabrication capability of AM provides an excellent tool to manufacture electronic devices conformable to an arbitrary shape, which has the potential for wearable electronics. High design and

manufacturing flexibility afforded by AM also allows for exploration for new designs of energy storage device for higher capacity. A fully 3D printed and packaged Li-ion battery has shown to have high areal capacity (Figure 1.3(j)) [37]. Moreover, interconnected photodetector arrays printed on both planar and hemispherical surfaces exhibited high sensitivity and wide field-of-view (Figure 1.3(k)) [38]. Five different materials including a photoactive layer, a transparent anode, a silver nanoparticle interconnect, an electrical insulating layer, and a cathode were concurrently printed on substrates with arbitrary geometries using MMAM.
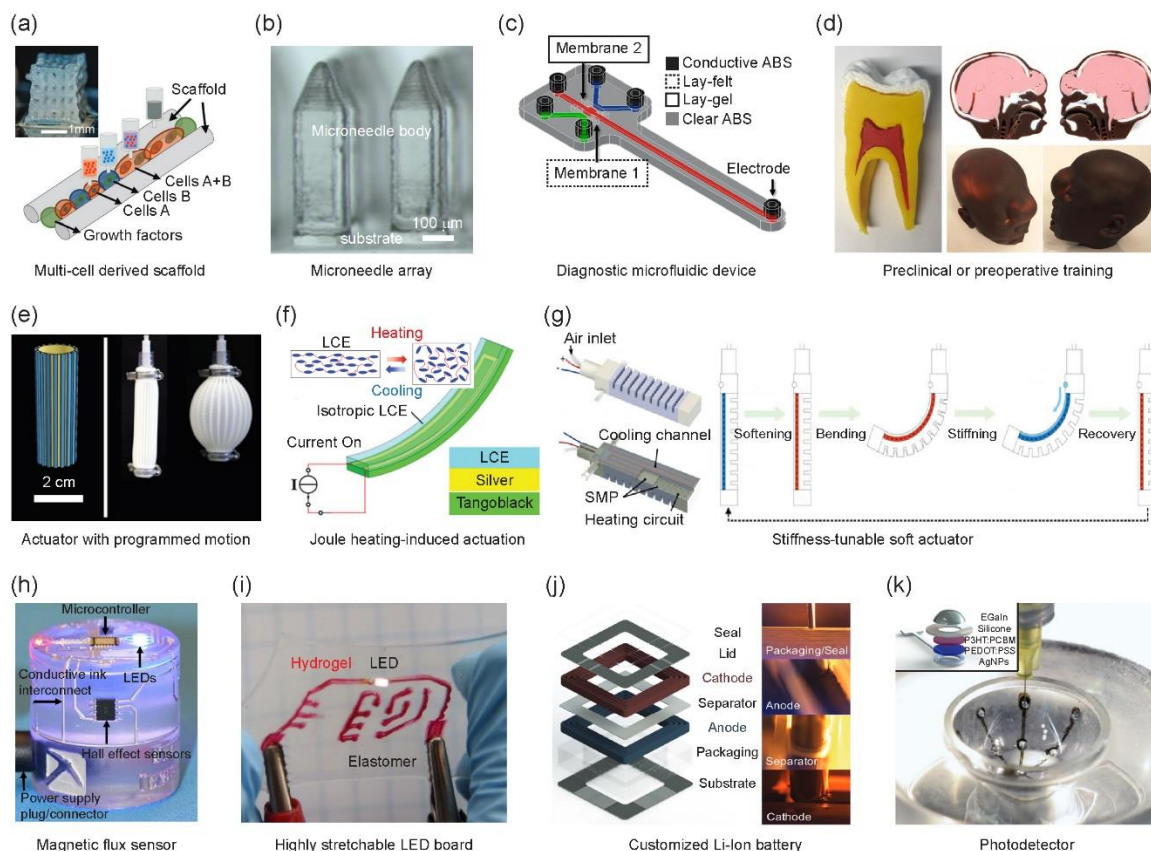
Figure 1.3. Recent applications enabled by MMAM in three areas; biomedical engineering (a-d), soft robotics (e-g), and electronics (h-k). (a) 3D spinal cord tissue-like structure with 3D printing of multiple cells (image adapted from [39]). (b) Transdermal microneedle array made of two parts; microneedle bodies and a substrate (image adapted from [70]). (c) Diagnostic microfluidic device fabricated with four different materials (image adapted from [71]). (d) 3D printed artificial models for preclinical or preoperative surgical training (images adapted from [72, 73]). (e) Programmed motion of elastomeric actuator through surface decoration with a stiff reinforcing material (image adapted from [35]). (f) Reversible soft robotic actuation with a resistive heating element (silver-nanoparticle ink) and stimuli-responsive liquid crystal elastomer (LCE) (image adapted from [76]). (g) Stiffness-tunable soft actuator consisting of soft elastomeric body, shape memory polymer

(SMP) layer, and resistive heating element (image adapted from [65]). (h) 3D magnetic flux sensor with integrated electronic components and conductive paths (image adapted from [77]). (i) Fabrication of highly stretchable electronic LED board by 3D printing of stretchable conductive hydrogel material on elastomer (image adapted from [67]). (j) Fully 3D printed and packaged Li-ion battery showing high areal capacity (image adapted from [37]). (k) 3D printing of photodetector arrays with five different materials on hemispherical surface (image adapted from [38]).

1.3. Dissertation organization

DLP-based projection stereolithography AM has distinctive advantages, such as high-resolution, scanning-free parallel process, low cost, and support-structure-free 3D printing. Also, it provides a wide range of material selection, including stimuli responsive hydrogels. Accordingly, this study encompasses the development of a novel DLP-based MMAM technique (multi-material projection micro-stereolithography, MM-PµSL) that shows cleaning process-free material exchange, 3D printing of soft active materials (stimuli-responsive hydrogels), characterization and quantification of dynamic behavior of soft active materials and devices, and implementation of bio-inspired design principles in soft active devices. Figure 1.4 presents how each of the specific research focuses are integrated with each other under this dissertation study.
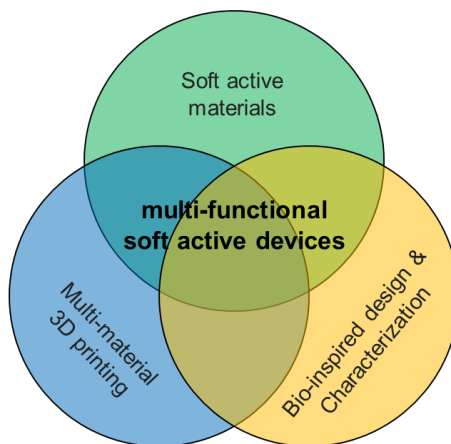
Figure 1.4. Schematic Venn diagram of this study

The main theme of this dissertation is the development of multi-functional soft active devices using multi-material 3D printing and soft active materials (stimuli-responsive hydrogels). The dissertation consists of six chapters; each of them describes a research process and results on a specific topic.

Chapter 1 provides a background of soft materials, systematic and comprehensive reviews on multi-material 3D printing techniques and their applications, and motivations of this dissertation.

Chapter 2 introduces the heterogeneous multi-material 3D printing system, MM-PµSL, developed and used for all of the researches in this dissertation. Fabrication of highly complex multi-material 3D micro-structures is demonstrated using an active material exchange process. Also, material exchange efficiency, the effects of energy dosage on curing depth, the degree of cross-contamination between different materials in a 3D printed multi-material structure are studied.

Chapter 3 presents micro 3D printing of a soft electroactive hydrogel which exhibits large deformation in response to an electric field. With 3D printed electroactive hydrogel micro-structures, soft robotic manipulation and locomotion are demonstrated. Based on 3D design and precise dimensional control enabled by our micro 3D printing technique, complex 3D actuations of EAH are achieved.

Chapter 4 is dedicated to demonstrating micro 3D printing of a soft thermo-responsive hydrogel which shows a large and reversible volume change in response to temperature change. Control of the temperature-dependent deformation of 3D printed thermo-responsive hydrogel structures is achieved by controlling manufacturing process parameters as well as polymer resin composition. Also demonstrated is a sequential deformation of a 3D printed thermo-responsive hydrogel structure by selective incorporation of ionic monomer that shifts the swelling transition temperature of the thermo-responsive hydrogel.

Chapter 5 presents a bio-inspired adaptive camouflage skin, which employs 3D printed multi-material artificial chromatophores composed of three components, photo-active muscles (material: photo-active hydrogel), a stretchable sac (material: acrylic acid hydogel), and a rigid frame (material: PEGDA 250). The photo-thermal effect of photo-active hydrogel, stretchability of AA hydrogel, and bonding strengths between materials are studied to design the artificial chromatophore. With printed artificial chromatophore, dynamic color change of the artificial skin is demonstrated.

Finally, Chapter 6 summarizes the studies presented in this dissertation and provides potential future studies.

Chapter 2

Rapid Multi-Material 3D Printing

with Projection Micro-Stereolithography

2. Rapid Multi-Material 3D Printing with Projection Micro-Stereolithography

2.1. Introduction

Additive manufacturing (AM), also referred to as three-dimensional (3D) printing, is a set of manufacturing techniques of directly building 3D physical objects by additively joining raw materials. Since the first invention of AM in 1980's [79], various AM technologies have been developed, such as direct ink writing (DIW) [80, 81], fused deposition modeling (FDM) [82], material jetting [83], stereolithography (SLA) [28, 84] and two-photon polymerization (2PP) [85, 86]. A variety of materials including polymers [87], metals [88], ceramics [89, 90], and biomaterials [91] have been used in AM for a wide range of applications, ranging from rapid prototyping to metamaterials [92, 93], medical devices [94], electronics [95], and tissue engineering [96, 97]. Although a growing number of materials have become available for AM, most of the existing AM techniques build an object with a single material only, which is a critical barrier to achieving advanced functionalities in 3D printed parts.

Among previously reported multi-material 3D printing techniques, many of them are based on an extrusion-based AM, such as DIW [32, 98, 99] and FDM [44, 100], or material jetting [48, 101]. Since these techniques deposit materials directly to the desired voxel, multi-material printing could be easily implemented by simply adding as many printing nozzles or inkjet heads as the number of materials being processed. However, multi-material 3D printing with a vat polymerization technique such as SLA and 2PP still remains challenging because an object is built by selectively solidifying a liquid material

that is already placed in a vat. To switch a printing material, the whole material in the vat has to be exchanged during the printing, which significantly interrupts and slows down the process, and consequently, increases the overall manufacturing time. In addition, a time-consuming cleaning process between material exchange may be required to remove and rinse out the un-crosslinked material around the object to avoid cross-contamination between materials.

Digital light processing (DLP)-based projection stereolithography AM has distinctive advantages such as high-resolution, scanning-free parallel process, wide material sets available, low cost, and support-structure-free 3D printing. Among a few recently reported projection stereolithography multi-material 3D printing techniques, the simplest method is to manually change material in the vat [102] or to switch between multiple vats containing different materials [60, 70, 103]. However, the printing process has to be stopped for a certain period of time in the middle of the process for material cleaning and change, making the entire production time extremely long. This problem becomes even more apparent when frequent material change is needed for hundreds of layers as material complexity of the part increases. Some groups implemented an automatic material change sequence using a rotational platform where multiple vats for different materials and a cleaning solution were placed [59, 92, 104, 105]. However, the majority of the production time was still spent on material change because of their long material change time (minutes) compared to the actual time for curing a layer (or curing time, seconds).

Here, we present design and development of a multi-material projection micro-stereolithography (MM-PμSL) system which is capable of rapidly and heterogeneously integrating multiple materials into a 3D structure using dynamic fluidic control of liquid

photopolymers within an integrated fluidic cell. The present system can quickly exchange materials without interrupting the process, enabling rapid high-resolution multi-material 3D printing. To achieve this, we characterized material volume flow rate in the fluidic cell, material exchange efficiency, and curing kinetics for various photopolymers with different properties. In addition, we evaluated material cross-contamination occurring during material change to assess the quality of the multi-material printing. Based on the results, we demonstrated 3D printing of a multiple-particles-loaded structure and a multi-responsive hydrogel micro-structure that responds to multiple external stimuli.

2.2. Materials and Methods

2.2.1. Materials

1,6-Hexanediol diacrylate (HDDA), Poly(ethylene glycol) diacrylate (PEGDA), Acrylic acid (AA), N,N'-Methylenebis(acrylamide) (BIS), Phenylbis(2,4,6-trimethylbenzoyl) phosphine oxide (photo-initiator, PI), Sudan I (photo-absorber, PA), 3,3´-Diethyloxacarbocyanine iodide (DiOC$_2$), Rhodamine B (RHB), Triton X-100 (surfactant), and Phosphate-buffered saline (PBS) were purchased from Sigma-Aldrich. N-Isopropylacrylamide (NIPAAm), Copper (Cu) nano-powder (70 nm), and Alumina (Al$_2$O$_3$) powder (BMA 15, 150 nm) were purchased from Fisher Scientific, US Research Nanomaterials, Inc., and Baikowski, respectively. All materials were used as received. Table 2.1 provides the chemical components of the solutions used in each study and their concentrations.

Table 2.1. Material composition of different printing solutions. Ethanol was used as a solvent for NIPAAm solution.

Study	Material composition							
	Monomer (M)	Cross-linker (mM)	PI (mM)	PA (mM)	DiOC$_2$ (μM)	RhB (μM)	Particles (vol. %)	Triton X-100 (mM)
Flow control (Sec.2.3.2)	Ethanol (control)	-	-	-	-	-	-	-
	HDDA	-	-	-	-	-	-	-
	PEGDA250	-	-	-	-	-	-	-
	PEGDA575	-	-	-	-	-	-	-
Material exchange process (Sec.2.3.3)	Ethanol (control)	-	-	-	-	-	-	-
	HDDA	-	-	-	0.8	-	-	-
	PEGDA250	-	-	-		-	-	-
	PEGDA575	-	-	-	-	-	-	-
Curing kinetics (Sec. 2.3.4)	PEGDA250	47.8	-	-	-	-	-	-
			-	-	0.8	-	-	-
			-	-	-	0.8	-	-
			-	-	1000	-	-	-
			-	-	-	1000	-	-
			-	-	-	-	Cu (0.45)	3.2
			-	-	-	-	Al$_2$O$_3$ (0.45)	3.2
Cross-contamination (Sec.2.3.5)	PEGDA250	47.8	-	-	0.8	-	-	-
		47.8	-	-	-	0.8	-	-
Multi-material 3D micro-structures (Sec.2.3.6.1)	PEGDA250	47.8	-	-	1000	-	-	-
			-	-	-	1000	-	-
Multi-particles-loaded structure (Sec.2.3.6.2)	PEGDA250	47.8	-	-	-	-	-	-
			-	-	-	-	Cu (0.45)	3.2
			-	-	-	-	Al$_2$O$_3$ (0.45)	3.2
			-	-	-	-	Cu (16)	3.2
			-	-	-	-	Al$_2$O$_3$ (16)	3.2
Multi-responsive hydrogel structure (Sec.2.3.6.3)	NIPAAm (6.2)	BIS (324)		12	-	-	-	-
	AA (13.3)	PEGDA250 (404)	47.8	-	-	-	-	-

2.2.2. Multi-material projection micro-stereolithography (MM-PμSL) system

The MM-PμSL system was built with the following major components: a UV LED (405 nm, Innovations in Optics), custom-built collimation optics (Thorlabs), a beam splitter (Thorlabs), a digital dynamic mask (liquid crystal on silicon, LCoS) extracted from a commercial digital projector (Cannon), a projection lens (Carl Zeiss), a linear stage (Newport Corporation), a custom-built fluidic cell, a pump (Parker), and 2-way pinch valves in each fluidic path (Reet Corp.). The fluidic cell consists of a cylindrical printing chamber with integrated microfluidic inlet and outlet channels, a cylindrical build platform with an embedded pumping channel, and a top plate with a circular hole to clamp a glass/PDMS window. Detailed drawings of each component and assembly is included in Figure 2.1. In this chapter, we used 3 material containers for 3 different materials, but it can be easily extended for as many materials as needed. All components of the system are controlled by a custom-written LabVIEW (National Instruments) script.
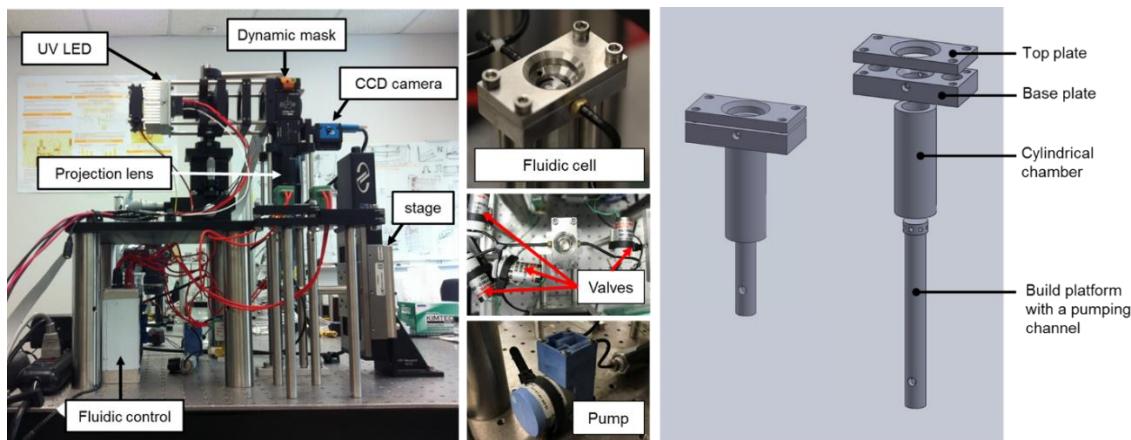
Figure 2.1. The photographs of multi-material projection micro-stereolithography (MM-PμSL) and a detailed design drawing of fluidic cell

2.2.3. Fluid flow measurement in MM-PμSL

In order to measure a volume flow rate of a liquid material in the MM-PμSL system, a material container was first connected into the fluidic cell. After filling in the container with the material to be tested, we started the pump to create a pressure-driven flow through the fluidic cell. The material discharged from the outlet of the pump for a given pumping time was collected and weighed using a digital balance. Discharged volume was calculated using a density of the material (Table 2.2).

Table 2.2. Material properties of liquid material samples

Property	Ethanol	HDDA	PEGDA 250	PEGDA 575
Viscosity (cP)	1	6.3	13.4	58.7
Density (kg m^{-3})	782	1,010	1,110	1,120

2.2.4. Viscosity measurement

Viscosity of four different materials, namely, ethanol, HDDA, PEGDA 250, and PEGDA 575, was measured at room temperature by viscometer (DV-II+ Pro, Brookfield Engineering Lab) with a cone-and-plate geometry (Table 2.2). 1 mL of each material was loaded between a cone with 48 mm diameter and a plate, and a shear stress was measured to calculate the viscosity. A shear rate of 20 rpm was used for all materials.

2.2.5. Fluorophore concentration measurement using a plate reader

Fluorescent intensity of $DiOC_2$ solutions were measured using a plate reader (Infinite M200 Pro, Tecan). Fluorescence filters with an excitation wavelength of 482 nm and an

emission wavelength of 513 nm were used. 100 μL of sample fluorescent solutions were pipetted into the wells of a standard 96-well plate. The fluorescent intensity was measured from the bottom of the plate. Fluorophore concentration of $DiOC_2$ solutions were calculated using the calibration curves showing the relationship between fluorophore concentration and fluorescent intensity (Figure. 2.2). To obtain the calibration curves, five solutions with predetermined fluorophore concentrations (0, 0.1, 0.2, 0.4, and 0.8 μM) were prepared and the intensity of each solution was measured using a plate reader.
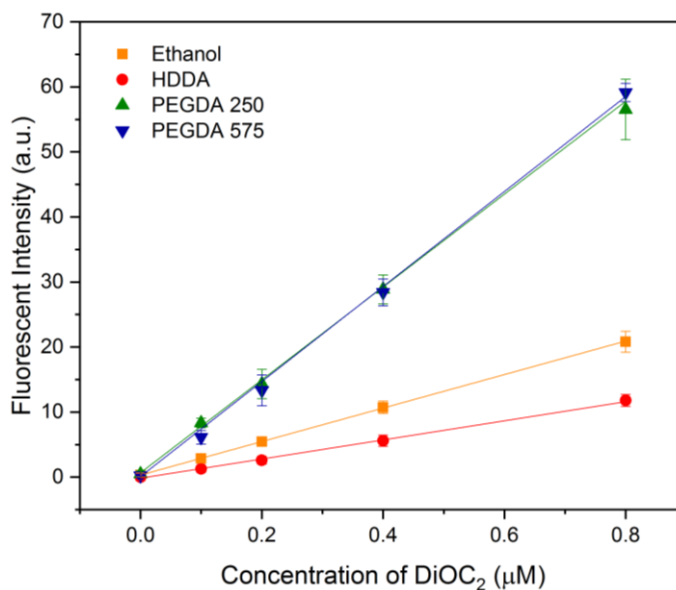
Figure 2.2. Calibration curves of DiOC2 solutions prepared with ethanol, HDDA, PEGDA 250, or PEGDA 575.

2.2.6. Fluorescent microscope imaging for cross-contamination study

Imaging of the printed structures containing fluorophores was performed using an inverted fluorescent microscope (IX81, Olympus). To quantify a degree of material cross-

contamination in a printed sample, green and red fluorescent microscope images of the sample were individually taken with two different filters. The green and red fluorescent intensities were extracted along a line at the center of the image (Figure 2.3(a)) using image analysis software, Image J. Then the obtained intensities were normalized to their respective maximum intensity (Figure 2.3(b) for green and Figure 2.3(c) for red). The area under each peak was calculated using data analysis software, Origin, and *cross-contamination index* and *purity index* were determined based on these areas (see sec. 2.3.5 for details).
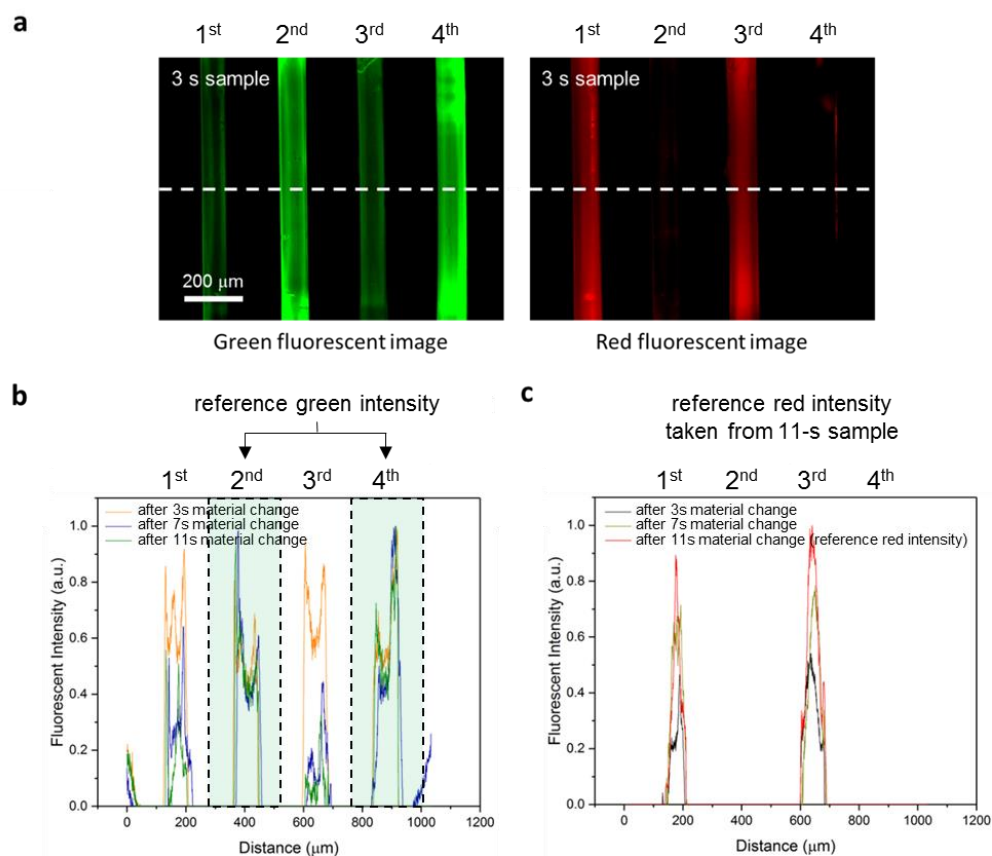
Figure 2.3. (a) Green and red fluorescent microscope images of the 3-second sample. The normalized fluorescent intensities extracted from green fluorescent image (b) and red fluorescent image (c).

2.2.7. Confocal fluorescent microscope imaging

A sample to be imaged was tightly attached to a glass slide using super glue. The glass slide on which the sample was placed was put on the inverted laser scanning confocal microscope (LSM 780, Zeiss). The green and red confocal fluorescent microscope images of the sample were individually taken with two different filters, and then two separate images were analyzed and merged using Image J.

2.2.8. X-ray micro computed tomography (CT) imaging

The 3D printed multi-material helix was prepared inside a pipette tip to immobilize the structure. The tip was, then, placed on the sample holder in the Skyscan 1172 Micro-CT system (Bruker). The structure was scanned at 6.5 μm resolution. Afterwards, the images were reconstructed to generate cross-sectional images and a 3D image of the structure with the Skyscan image reconstruction software, NRecon.

2.2.9. Multi-responsive hydrogel swelling experiment

The bilayer hydrogel beam was printed using MM-PμSL with two different hydrogels, thermo-responsive hydrogel and electroactive hydrogel. After printing, the sample was stored in deionized water (DI water) overnight for rinsing. Then the sample was put into a 0.05 M PBS solution and stored at 5 $^{\circ}$C for 24 hours. To test responsive swelling with varying temperature and electric field, the bilayer hydrogel beam was placed between two platinum wire electrodes separated by 5 cm in a temperature-controlled chamber filled with

0.05 M PBS solution. After setting the temperature, an electric field was applied for 10 s using a DC power supply (voltage of 30 V). In order to let it return to its original shape, the sample was left in the chamber at the same temperature for 10 min with no electric field applied. The reverse electric field was then applied for 10 s at the same electric field strength. All deformations of the sample were recorded with a digital camera.

2.3. Results and Discussion

2.3.1. MM-PµSL system and process overview

Projection micro-stereolithography (PµSL) is a high-resolution vat polymerization AM technique which uses a digital micro display as a dynamic mask generator [60, 106-112]. As shown in Figure 2.4(a), a 3D model created by computer aided design (CAD) software is digitally sliced into a series of cross-sectional images. Ultraviolet (UV) light from a UV light emitting diode (LED) is first guided to the dynamic mask generator which displays a digital image. Then, the spatially patterned UV light is projected through a projection lens and focused on the surface of a liquid photopolymer. Upon UV exposure, the liquid photopolymer is converted to solid, rapidly forming a layer in a desired pattern in seconds. Then the build platform on which a printed object sits is lowered vertically, and the next image is projected to form a new layer on the proceeding one. This process is repeated for all the layers until the 3D object is completed. PµSL is compatible with a variety of photopolymers including shape memory polymers [60, 113] and hydrogels [110, 111, 114]. Metal and ceramic 3D printing has been also achieved through PµSL by using metallic

[92] and ceramic [112] particles suspended in a liquid photopolymer solution or using polymer-derived ceramics [115].
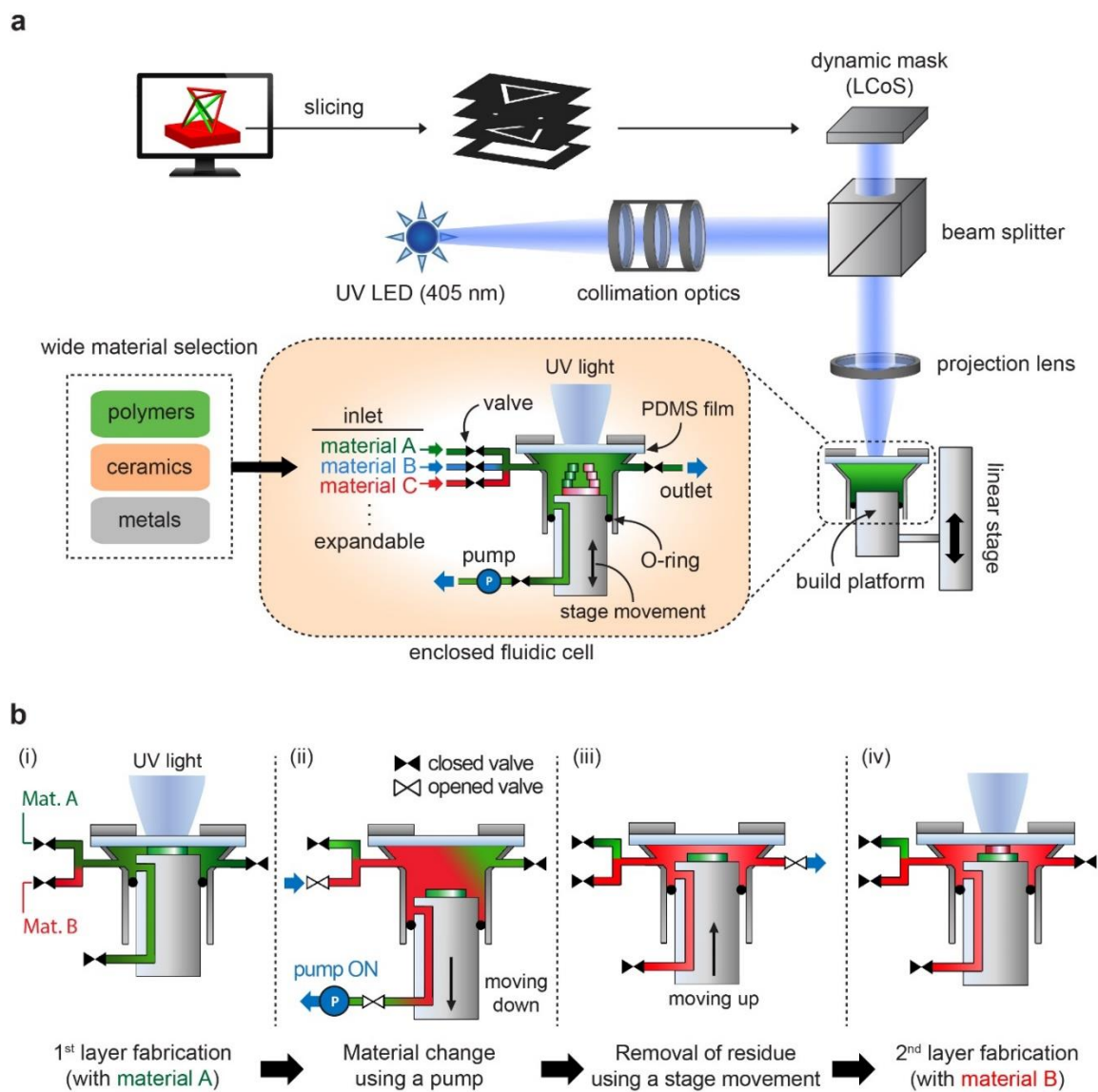
Figure 2.4. Schematic illustration of the MM-PµSL overall process (a) and material exchange process (b).

In this chapter, we present a multi-material PμSL system that can rapidly switch photocurable materials. To achieve quick and active material exchange, we designed and fabricated an integrated pressure-tight fluidic cell in place of an open vat. Schematic diagram of the system is shown in Figure 2.4(a). A transparent glass window coated with polydimethylsiloxosane (PDMS) is tightly clamped to the top of the fluidic cell. Being optically transparent, the PDMS coating allows the UV light (λ = 405 nm) to pass through and reach a photocurable polymer solution in the fluidic cell. Oxygen permeability of PDMS helps to create a thin inhibition layer at the PDMS-photopolymer interface, facilitating separation of a polymerized layer from the PDMS when the printing platform is lowered for the next cycle [116, 117]. In addition, elastic PDMS coating serves as a gasket, ensuring tight sealing of the fluidic cell to prevent material leaking or gas bubble forming during the pressure-driven material exchange process. Multiple UV-protected material containers and a pump are connected to the fluidic cell through tubing and internal fluidic channels of the fluidic cell. Through a computer-controlled valve and pump operation sequence, the fluidic cell is filled with a material to be printed. When material change is needed, a new material in a respective container is quickly pumped to the fluidic cell to replace the previous material in the printing chamber. Once the chamber is completely filled with a liquid material in the beginning, no air bubble that could scatter projection light is generated inside the fluidic cell because of the tight sealing achieved by elastic PDMS coating. The custom-built multi-material PμSL system is shown in Figure 2.1. With the current configuration, the optical system can deliver light irradiance of up to 200 mWcm^{-2} with a lateral resolution of 5 μm on the projection plane.

Figure 2.4(b) illustrates the material change process. A material in the fluidic cell is replaced by a pressure-driven flow of a new material. The following sequence is to change the printing material from material A (green) used for the previous layer (i in Figure 2.4(b)) to material B (red) for the subsequent layer. First, the valve for material B opens when the build platform moves down. This process creates a negative pressure inside the fluidic cell, driving the flow of material B into the fluidic cell. Once the platform completes descending, the pump connected to the fluidic cell through the center channel is turned on to flush the fluidic cell with material B while drawing the remaining material A out of the fluidic cell (ii in Figure 2.4(b)). While doing so, the structure being printed on the build platform in the fluidic cell is vigorously rinsed with material B, eliminating the need for a separate cleaning process which would be otherwise necessary to remove uncured material around the structure. When material change is completed, the pump is turned off, and the build platform pushes the residual material through the outlet channel of the fluidic cell while moving up to the position for the next layer (iii in Figure 2.4(b)). Then, the outlet channel of the fluidic cell is closed, leaving the fluidic cell now filled with material B for the next layer to be cured on top of or next to the previous layer upon UV exposure (iv in Figure 2.4(b)). Not only can this process build layers of different materials on top of each other, it can also integrate different materials side-by-side within the same layer. By performing this automated process whenever material change is necessary, different materials can be three-dimensionally (vertically and horizontally) joined together, resulting in a true multi-material 3D object.

2.3.2. Flow control in the fluidic cell for material change

In the material change process described above, the time required for the material to be completely replaced varies depending on the volume flow rate, which is closely related to the viscosity of the material when an applied pressure is given [118]. Since different liquid feedstock materials may have different viscosity, the relationship between the viscosity of the material and the material flow rate through the fluidic cell can help to predict the minimum material exchange time required. For this study, we used four different liquid material samples with different viscosity, namely ethanol, HDDA, PEGDA 250, and PEGDA 575 (Table 2.2) and measured their respective flow rates during pumping. As shown in Figure 2.5(a), the average flow rate of ethanol, HDDA, PEGDA 250, and PEGDA 575 is 1.8, 1.5, 1.3, and 0.5 cm^3 s^{-1}, respectively.

With any of these volume flow rates, the fluidic cell having an internal chamber volume of ~1 cm^3 can be filled in a matter of seconds. The result shows that viscosity and volume flow rate are inversely proportional, as predicted by Hagen-Poiseuille law [118]. Since different materials would need different material change times, the overall printing time to complete a multi-material 3D structure can be minimized by giving a material exchange time tailored to the viscosity of the material being processed.
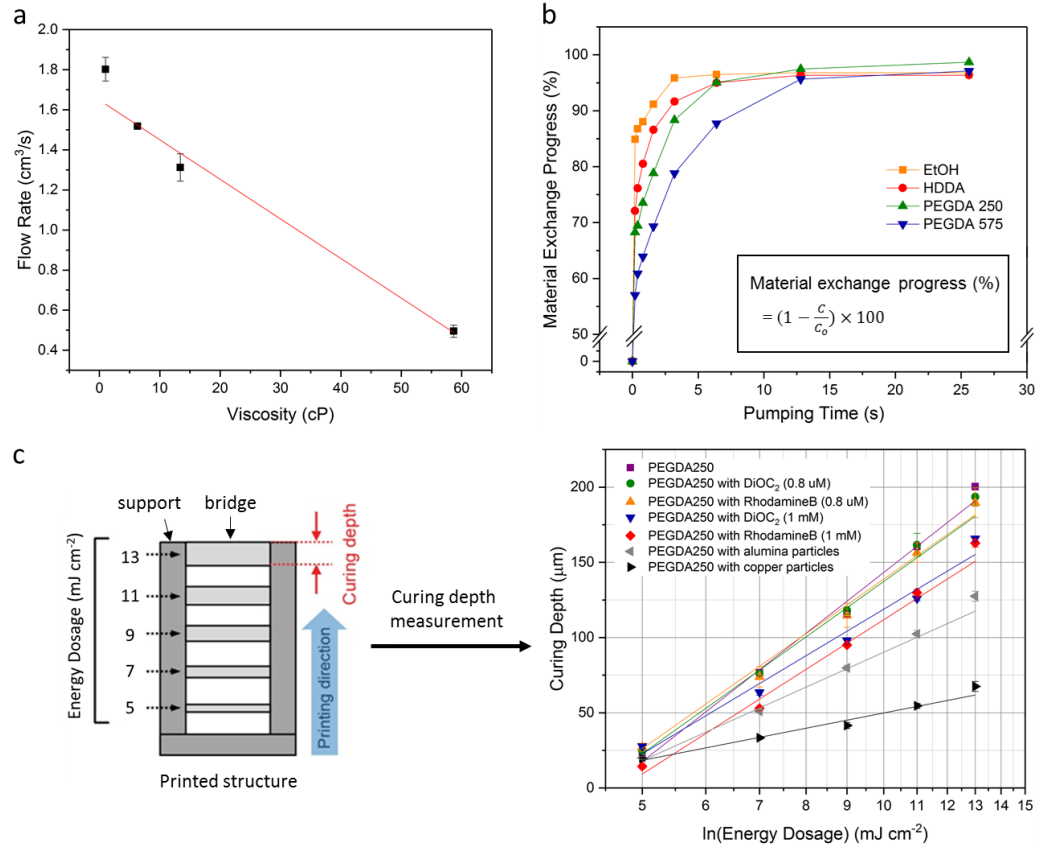
Figure 2.5. MM-PµSL system characteristics. (a) The relationship between viscosity and material flow rate in the fluidic cell. (b) Time evolution of material exchange progress for four different materials, namely ethanol (orange squares), HDDA (red circles), PEGDA 250 (green triangles), and PEGDA 575 (blue inverted triangles). (c) MM-PµSL curing depth working curves for different materials. The curing depth increases with energy dosage, but shows different growth rates depending on material.

2.3.3. Material change process

For a given flow rate, a longer pumping process introduces a higher volume of a new material into the fluidic cell, leading to more thorough material exchange. At the same time,

it increases overall printing time and material consumption. Therefore, it is important to determine an appropriate pumping time for given materials to maximize process throughput and material efficiency. To determine a pumping time, evolution of material composition in the fluidic cell during the material exchange process was measured. To this end, the fluidic cell was first filled with a liquid material sample (ethanol, HDDA, PEGDA 250, or PEGDA 575) containing 0.8 μM of green fluorescent dye ($DiOC_2$). The concentration of the fluorescent dye was constantly monitored while the same material without a dye was driven into the fluidic cell. As material exchange progresses, the material in the fluidic cell is diluted and concentration of the dye decreases. We sampled the solution from the fluidic cell at 0.2, 0.4, 0.8, 1.6, 3.2, 6.4, 12.8, and 25.6 s of pumping time, and measured the fluorescent intensity by a plate reader (Infinite M200 Pro, Tecan) (λ_{ex}: 482 nm, λ_{em}: 513 nm). Then, we calculated the fluorophore concentration with calibration curve (Figure 2.2) showing the relationship between fluorophore concentration and fluorescent intensity. Material exchange progress was quantitatively assessed with the fluorophore concentrations (Figure 2.5(b)). We define *material exchange progress index* (%) as $\left(1 - \frac{c}{c_0}\right) \times 100$, where c and c_0 are current and initial concentrations of the fluorescent dye in the fluidic cell. Figure 2.5(b) shows time evolution of material exchange progress indices for all tested materials. If we set the threshold material exchange progress to be 95%, material exchange times for ethanol, HDDA, PEGDA 250, and PEGDA 575 are 3.2, 6.4, 6.4, and 12.8 s, respectively. It is clearly seen that more viscous material requires more time to complete material exchange because of low volume flow rate. However, even with PEGDA 575 having a relatively high viscosity of 65 cP, near complete material exchange can occur within around 10 s. Compared to previously reported works (Wang et al. [92]

and Zhou et al. [104]), our multi-material process using dynamic flow control offers more than 30 times faster material switching, while maintaining exceptional printing resolution inherited from PµSL. The smallest feature size achieved with this system is 5 µm (Figure 2.6), which is more than an order of magnitude better than the reported multi-material stereography techniques (300 µm, Wang et al. and Zhou et al.).
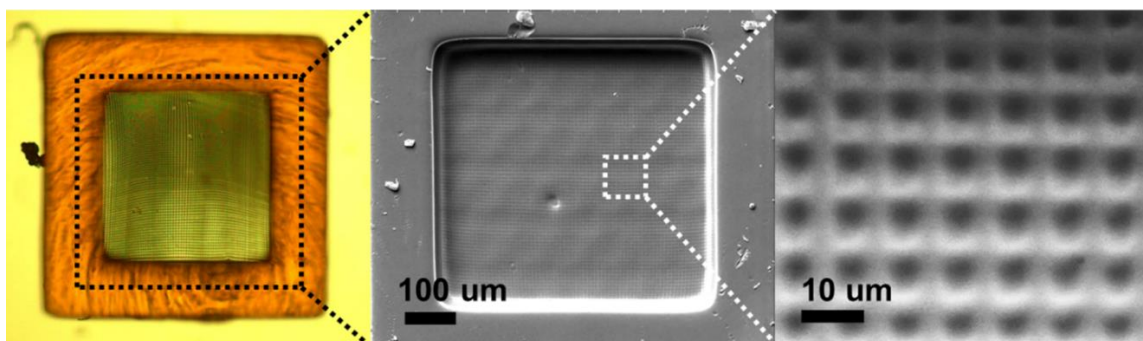
Figure 2.6. Optical microscope image and Scanning Electron Microscopy (SEM) images of printed structure with 5 µm grid lines.

2.3.4. Curing kinetics of different photopolymers

When a layer is formed upon light irradiation, photopolymerization starts from the top surface of the photopolymer and propagates into the polymer, resulting in continuous growth of the layer thickness over time. This thickness is called curing depth [119]. Since different photopolymers or the same photopolymer with different precursor or dye concentrations may have different reactivity, different light energy should be given to keep the layer thickness constant across multiple materials. To study the effect of light energy dosage on curing depth, we prepared a set of liquid photopolymers as listed in Table 2.1. A test structure comprised of two side supports and five suspended bridges between the

supports was printed for each photopolymer (Figure 2.5(c)). A sufficient vertical distance between the bridges (240 μm) was given such that the bridges were not touching with each other. Due to different levels of energy dosage given, each bridge grew to a different thickness. The intensity of UV light was 10.0 mW cm^{-2}, and exposure time for the bridges gradually increased from 0.5 to 1.3 s in increments of 0.2 s. Thickness of the bridges was measured using an optical microscope, and the curing depth as a function of light energy dosage was plotted for different photopolymer solutions in Figure 2.5(c). The curing depth increases with energy dosage, but at a different rate depending on material, following the stereolithography working curve equation, $C_d = D_p \ln(E/E_c)$, where C_d is a curing depth, and E is a light energy. Two key constants of a liquid photopolymer, D_p and E_c, are characteristic cure depth and critical energy, respectively [119]. Curing time per layer for a given material and for a desired layer thickness was determined based on this result. Table 2.3 lists all process parameters used to fabricate the multi-materials samples presented in the following sections.

Table 2.3. Printing parameters for the samples presented in this work

Section	Sample	Materials	Light intensity (mW cm^{-2})	Layer thickness (μm)	Curing time (s)	Pump time (s)
Cross-contamination (Sec.2.3.5)	Beams	PEGDA250 (0.8 μM DiOC$_2$) PEGDA250 (0.8 μM RhB)	10	100	1	3 - 11
Multi-material 3D micro-structures (Sec.2.3.6.1)	Taiji symbol	PEGDA250 (1 mM DiOC$_2$) PEGDA250 (1 mM RhB)	10	50	1.2	7
	Tense-grity	PEGDA250 (1 mM DiOC$_2$) PEGDA250 (1 mM RhB)	10	20	0.8	7
	Micro-capillary	PEGDA250 (1 mM DiOC$_2$) PEGDA250 (1 mM RhB)	10	20	0.8	7
Multi-particles-loaded structure (Sec.2.3.6.2)	Helix	PEGDA250 PEGDA250 (Cu) PEGDA250 (Al$_2$O$_3$)	10	50	1 1.2 1.2	11
	Taegeuk symbol	PEGDA250 (Cu) PEGDA250 (Al$_2$O$_3$)	10	25	700 300	90
Multi-responsive hydrogel structure (Sec.2.3.6.3)	Bilayer-beam	NIPAAm AA	30	30	10 0.5	7

2.3.5. Cross-contamination between materials

Since the material in the fluidic cell is gradually changed as a new material flows in, the material being replaced can be left behind in the fluidic cell if an influx of a new material is insufficient. In this case, a mixture of the two materials is present in the fluidic cell during crosslinking, which reduces a contrast between different materials, thereby degrading distinctive property and functionality of each material as well as the print quality of the multi-material structure. We call this cross-contamination. To achieve high-quality and high-fidelity multi-material 3D printing, we evaluated the effect of material exchange time

on cross-contamination. Three identical test structures shown in Figure 2.7(a) were printed with PEGDA 250-based photopolymer solutions (Table 2.1) using different material exchange times of 3, 7, and 11 s. The test structures have four thin strips (100 μm) made of two different fluorescent materials (Table 2.1). The 2nd and 4th strips were printed with the green material, followed by material switch to the red material for the 1st and 3rd strips, as illustrated in Figure 2.7(a).
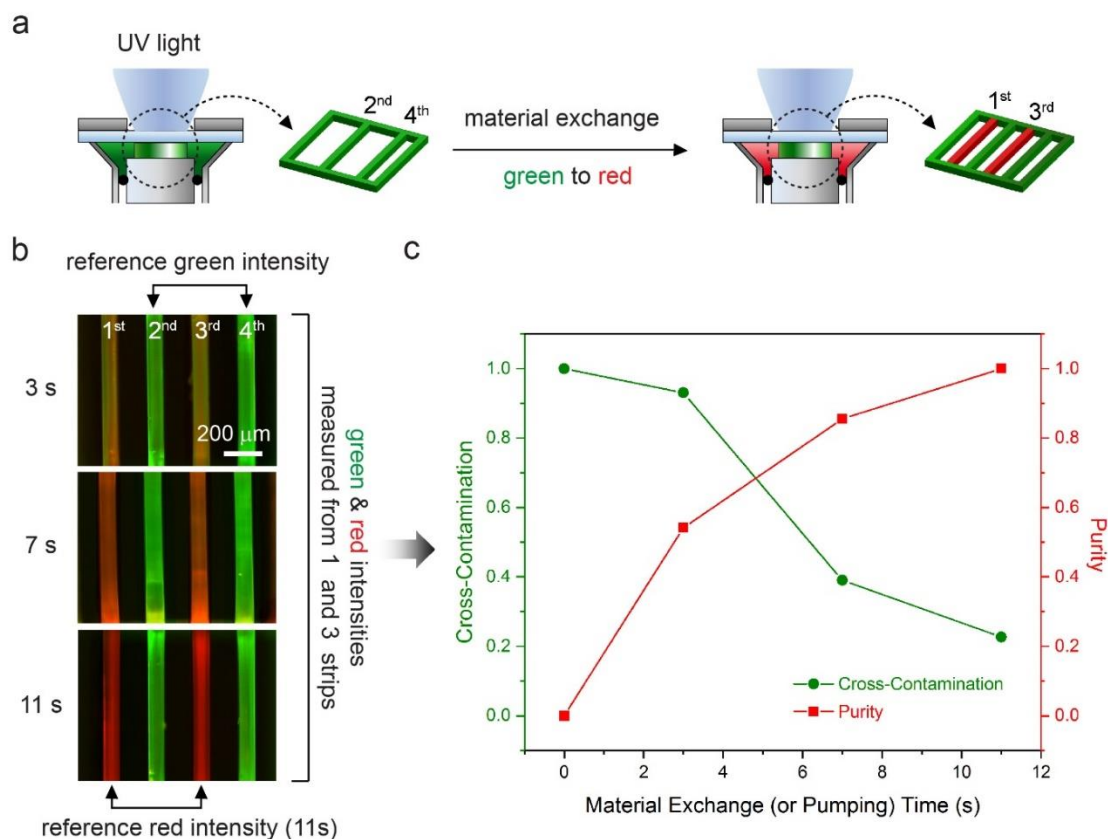
Figure 2.7. Multi-material cross-contamination assessment. (a) Schematic illustration of the 3D printed test sample having four thin strips made of two different fluorescent materials. (b) Fluorescent microscope image of the test samples printed with different material exchange time (3, 7, or 11 s). (c) Progression of the two indices, Cross-contamination index (green circles) and Purity index (red squares), with pumping time.

The green and red fluorescent images of the structure were taken using a fluorescent microscope (Figure 2.7(b) and Figure 2.3(a)) and intensity for each color was extracted from the image to quantify a degree of material cross-contamination in a printed sample. The obtained intensities were normalized to their respective reference intensity (Figure 2.3(b) for green and Figure 2.3(c) for red). Since the 2nd and 4th green strips were first printed without any foreign materials present, their green intensity is constant regardless of the pumping time, and it can be considered as the intensity of a pure green material (reference green intensity) (Figure 2.3(b)). Therefore, we defined *cross-contamination index* as a ratio of undesirable green intensity present in the red strips (1st and 3rd) to the reference green intensity from the green strips (2nd and 4th). On the other hand, *purity index* is defined as a ratio of red intensity measured from the red strips (1st and 3rd) normalized to the reference red intensity taken from the sample with the maximum red intensity (11-s sample) (Figure 2.3(c)). The mixed colors representing significant cross-contamination between the two materials were observed in the red strips (1st and 3rd). These mixed colors are most apparent in the 3-s sample. As material exchange progresses, cross-contamination index decreases from 1 to 0, while purity index increases from 0 to 1. Note that the sum of these two indices is not necessarily one because they are based on different reference values. Figure 2.7(c) plots progression of the two indices with pumping time, showing that increasing material influx during material change process will result in a high material contrast in a multi-material structure with low cross-contamination. However, it is worth noted that prolonged pumping time will eventually slow down overall printing process and increase material consumption. The material consumption during 11 s pumping (14 cm^3)

was about 1.6 times higher than 7 s pumping (9 cm^3). In all subsequent experiments using PEGDA 250-based photopolymer solutions, a material exchange time of 7 s was used.

2.3.6. Rapid, high-resolution multi-material 3D printing

2.3.6.1. Multi-material 3D micro-structures

Using the MM-PμSL system and multiple photocurable materials (Table 2.1), we printed 3D micro-structures as shown in Figure 2.8(a-c). First, a Taiji symbol patterned cylindrical structure was printed (Figure 2.8(a)). The diameters of the whole structure and the small dot inside are 1 mm and 100 μm, respectively. Two distinctive colors with clear boundaries were observed. We also fabricated a tensegrity structure consisting of high aspect ratio beams with different materials as shown in Figure 2.8(b). The diameter of the struts is 100 μm and the height of the overall structure is 2 mm. Fluorescent microscope images clearly show that the structure was created with two different materials (green and red). Third, we printed a bilayer micro-capillary structure with a hollow channel (inner diameter of 100 μm) as shown in Figure 2.8(c). Each layer has a thickness of 50 μm, which is clearly seen from the confocal fluorescent microscope images in different parts of the structure: top (Figure 2.8(c) (ii)), middle (Figure 2.8(c) (iii)), and bottom (Figure 2.8(c) (iv)). These results suggest that the present system provides the ability to create highly complex multi-material 3D micro-structures that would be difficult or impossible to fabricate with existing 3D printing techniques.
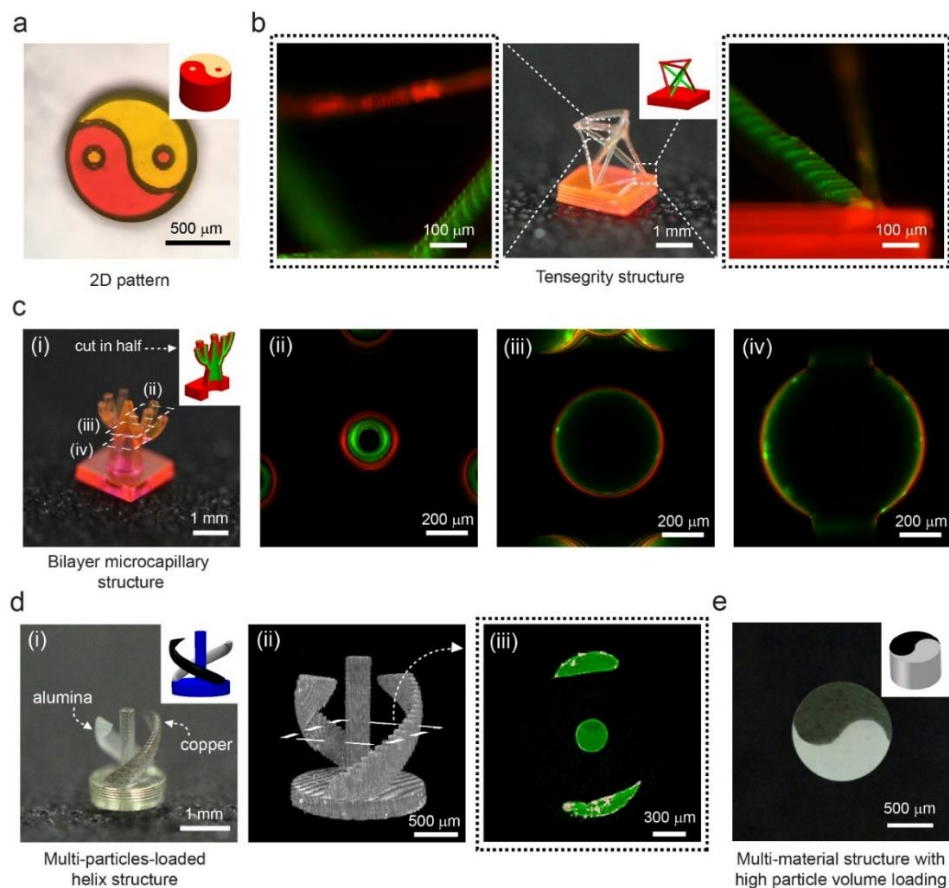
Figure 2.8. Multi-material micro 3D structures fabricated with MM-PµSL. (a) Optical microscope image of the Taiji symbol patterned cylinder made of two different materials. (b) Fluoresecnet microscope images of the tensegrity structure consisting of multi-material high aspect ratio beams. (c) Confocal fluorescent microscope images in different parts of the multi-material bilayer micro-caplillary structure: top (ii), middle (iii), and bottom (iv). (d) 3D helix composed of three different parts; particle-free center pillar, two helix arms loaded with copper and alumina nano-particles. 3D (ii) and cross-sectional (iii) micro CT images of the structure. The green areas and white dots indicate the polymer matrix and particles, respectively. (e) Taegeuk symbol patterned cylinder with high particle loading (16 vol. %) of two different materials (copper and alumina nano-particles in black and white areas, respectively).

2.3.6.2. Multi-particles-loaded 3D structure

Particle-loaded photocurable solutions have been employed in stereolithography to extend properties and functionalities of a 3D printed object beyond those of photocurable polymers. Examples include metallic and ceramic 3D parts obtained through pyrolysis of a 3D printed particle-loaded polymers [92, 112] and 3D tissue scaffolds printed from photopolymers with suspended living cells [31, 32]. With the pressure-tight fluidic cell that allows for facile control of multiple flow streams, our MM-PμSL provides a unique platform to integrate various particles in a single 3D structure. To demonstrate this capability, we printed a 3D helix having 3 arms shown in Figure 2.8(d) (i), with each arm made of different materials; particle-free center pillar (transparent), two helix arms loaded with copper (black) and alumina (white) nano-particles. Since the presence of particles increases the viscosity of a photopolymer (Figure 2.9 and Table 2.4) [120], a longer pumping time of 11 s was used to ensure enough material influx during material exchange (Table 2.3). The height of the overall structure and the diameter of the arms are 2 mm and 300 μm, respectively. 3D (Figure 2.8(d) (ii)) and cross-sectional images (Figure 2.8(d) (iii)) of the structure were obtained by micro computed-tomography (micro CT). The green areas and white dots in Figure 2.8(d) (iii) represent the polymer and nano-particles, respectively, confirming that the particles were selectively loaded in the desired parts. Also demonstrated is a multi-material 3D structure with high solid loading of nano-particles (Table 2.1), which could potentially be converted to a ceramic/metallic structure via thermal post-processing such as pyrolysis and sintering [112, 121]. We printed a cylinder patterned with a Taeguek symbol consisting of two parts loaded with 16 vol. % of copper (black) and alumina (white) nano-particles, respectively, as shown in Figure 2.8(e). The

diameter and height of the structure are 1 mm and 350 μm, respectively. A longer pumping

time of 90 s (Table 2.3) was used for material exchange because of higher viscosity (~ 270

cP) of the solutions (Figure 2.9 and Table 2.4). These result suggests MM-PμSL could

potentially enable selective assembly of various non-photocurable functional materials

including carbon nanotubes, graphene, quantum dots and even different cell lines.
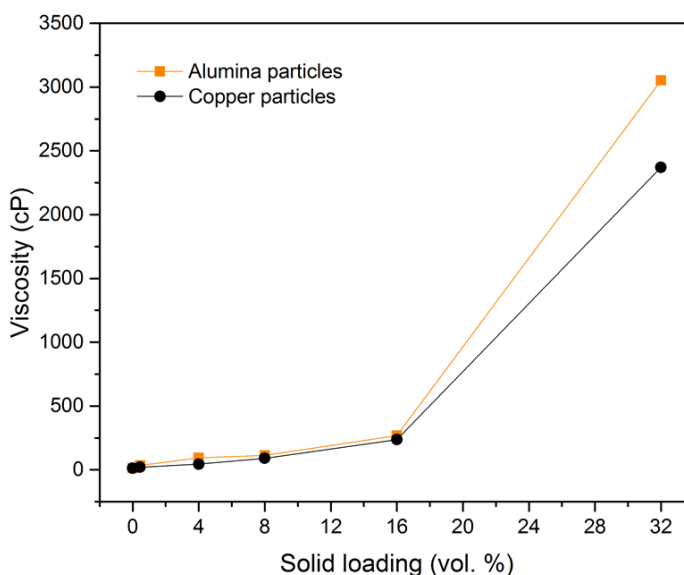
Figure 2.9. Relationship between solid loading of particles and viscosity. PEGDA 250 was

used as a solvent for all solutions. Viscosity of the solutions was measured at room

temperature by Kinexus Rotational Rheometer (Malvern Instruments) with PU 40 plate

geometry (diameter: 40 mm). A shear rate of 20 rpm (0.33 s^{-1}) was used for all solutions.

Table 2.4. Viscosity of particles-loaded solutions

Solid loading (vol. %)	0.45	4	8	16	32
Alumina (cP)	35	94	113	268	3052
Copper (cP)	20	45	91	237	2371

2.3.6.3. Multi-responsive hydrogel structure

3D printing of stimuli-responsive hydrogels is on the rise of gaining growing attention for smart materials and structures for many applications including soft robotics, targeted drug delivery, and tissue engineering [13]. Multi-responsive 3D hydrogel fabricated by MM-PµSL will significantly extend the potential of smart structures by enabling more diverse and complex deformation in response to various stimuli simultaneously. Using MM-PµSL, we fabricated a bilayer beam with two different stimuli-responsive hydrogels; thermo-responsive [110] and electroactive [111] hydrogels (Figure 2.10). Materials used to prepare the photocurable precursor solutions are listed in Table 2.1. The thermo-responsive hydrogel swells at a temperature below its low critical solution temperature (LCST) of 32 °C, and shrinks when the temperature is above its LCST [122] (relevant content will be discussed in Chapter 4). Also, the electroactive hydrogel exhibits different degrees of swelling in an electrolyte when an electric field is applied [123] (relevant content will be discussed in Chapter 3). The thickness of each hydrogel layer is 150 µm and the total length of the beam is 2.7 mm. The bilayer beam was straight at high temperature (55 °C) due to the same equilibrium swelling of the two hydrogels. However, when the temperature was lowered to 10 °C, only thermo-responsive hydrogel swelled further while electroactive hydrogel remained the same, causing the whole beam to bend, as illustrated in Figure 2.10(a). When this beam was subjected to an electric field, the electroactive hydrogel swelled or shrank depending on the direction of the electric field, again causing the whole beam to bend, as illustrated in Figure 2.10(b). In our experiments where we varied temperature (Figure 2.11) and electric field directions, the bilayer multi-responsive hydrogel beam showed various modes and degrees of bending deformation as expected,

depending on the combination of simultaneously applied stimuli, as shown in Figure 2.10(c).
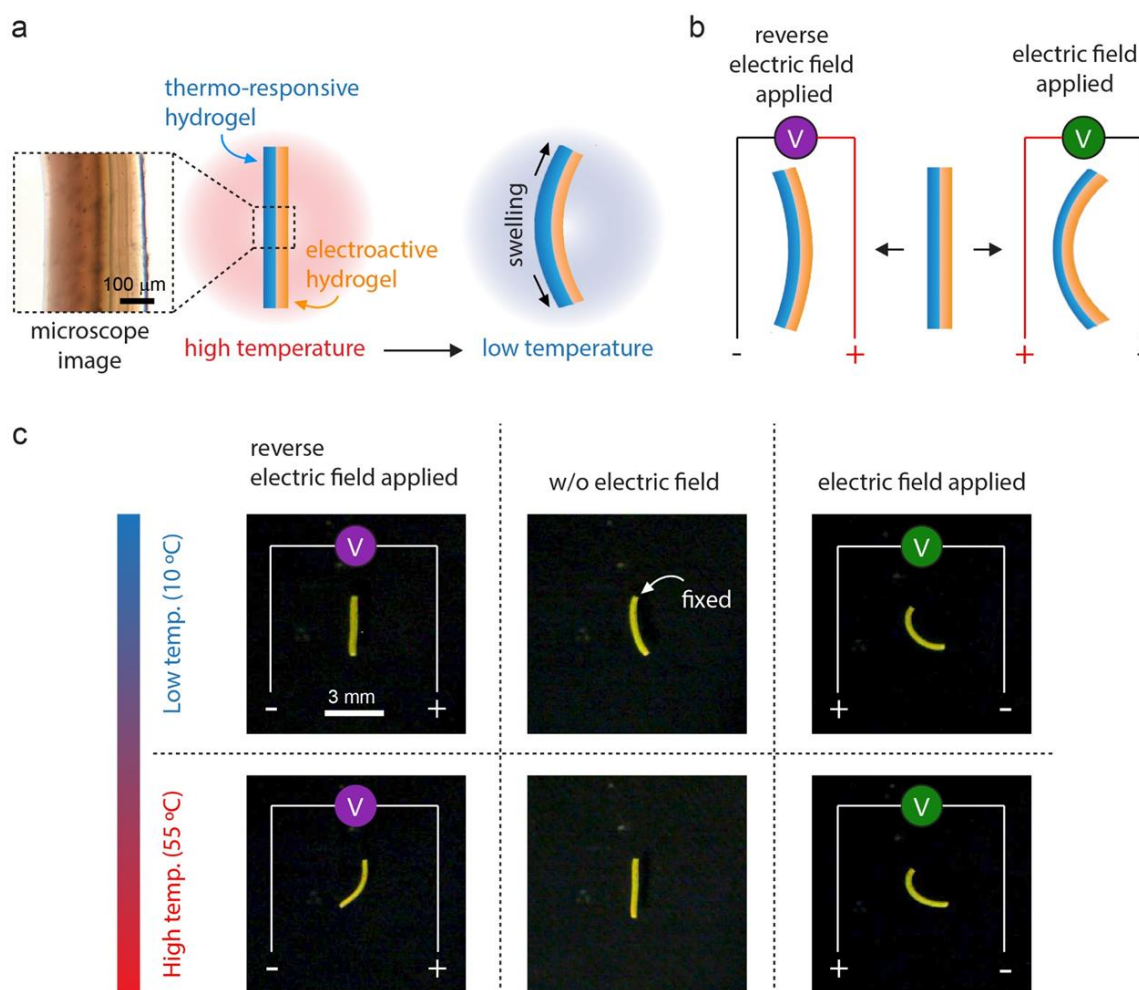
Figure 2.10. Multi-responsive bilayer hydrogel beam printed with two different stimuli-responsive hydrogels; thermo-responsive and electroactive hydrogels. Schematic illustration of bending deformation of the bilayer beam according to temperature change (a) and electric field direction control (b). (c) Various modes and degrees of bending deformation of the structure in response to the combination of simultaneously applied stimuli.
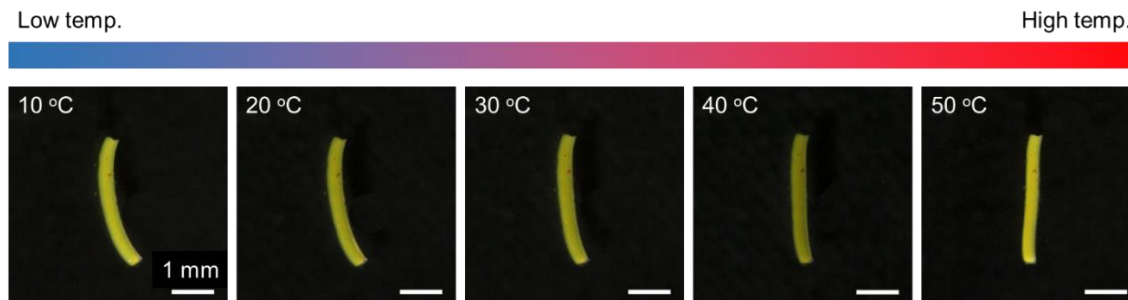
Figure 2.11. Thermo-responsive deformation of 3D printed bilayer hydrogel beam.

2.4. Conclusion

Stereolithography-based multi-material 3D printing methods reported thus far suffer from their long printing time due to interruptive and time-consuming material change processes for liquid-state materials in a vat. In this chapter, we presented a rapid multi-material micro 3D printing with a novel MM-PμSL system with an integrated fluidic cell in which multiple liquid photopolymers can be quickly exchanged through dynamic fluidic control. More than 95 % of the material inside the fluidic cell can be exchanged within a few seconds, showing an order of magnitude faster performance than previously reported multi-material stereolithography techniques. Based on the system characterization results we obtained, we successfully demonstrated high-resolution 3D printing of multi-material structures. We also presented 3D printing of a multi-particles-loaded structure with embedded metal (copper) and ceramic (alumina) nano-particles. Also demonstrated was 3D printing of a multi-responsive hydrogel bilayer beam with thermo-responsive and electroactive hydrogels. All the multi-materials micro 3D structures presented herein were printed within less than an hour, showing remarkable improvement in manufacturing throughput while maintaining excellent micro-scale printing precision. A few limitations of the current

system configurations to be addressed in future research include increasing material consumption with the number of materials used due to unavoidable material mixing during material change and compromised process throughput for highly viscous materials due to reduction in a material flow rate. Nevertheless, considering rapidly growing number of new printable materials with emerging properties, we believe our rapid multi-material micro 3D printing technique will become a new enabling manufacturing tool for facile production of multi-functional structures and devices across all fields.

Chapter 3

Micro 3D Printing of Electroactive Soft Devices

3. Micro 3D Printing of Electroactive Soft Devices

3.1. Introduction

Soft actuators achieve flexible motion using deformation of the material itself. Elastomers have been widely used in various soft robots and actuators [124-127]. However, they rely on either pneumatic or hydraulic pressure for actuation, often requiring bulky and complex auxiliary equipment such as compressors, pressure-regulators, and tubing. Untethered and autonomous soft actuators have been reported, using shape memory polymers and hydrogels that respond to external stimuli such as temperature, pH, and electric field [13, 128]. Particularly, electroactive hydrogel (EAH) actuators which exhibit large deformation in response to an electric field have gained much attention due to their favorable attributes including fast actuation, ease of control, and biomimetic materials properties [129]. Although many different types of EAH actuators have been developed [129-135], most of their actuations are simple. The shape and design of the EAH actuator have been significantly limited because of two-dimensional (2D) fabrication methods such as cutting, molding, and lithography. Recently, simple locomotion of an EAH structure has been demonstrated using two different types of EAHs that deform in opposite directions in the electric field [136]. Additive manufacturing (AM), a set of processes for three-dimensional (3D) fabrication, has been increasingly used for a wide range of materials including hydrogels [25, 30, 137, 138]. In particular, projection micro-stereolithography (PμSL) is a rapid, flexible, and high resolution 3D printing method using a digital light processing (DLP) technique [107, 108, 110]. In this chapter, we demonstrate soft robotic manipulation and locomotion of 3D printed EAH using PμSL. We study bending deformation of an EAH

for various electrolyte concentrations and electric field strengths to better understand and control actuation. Taking advantage of the precise dimensional control afforded by PμSL, we investigate the effects of characteristic thickness of an EAH structure on its actuation. Based on the findings, we demonstrate complex soft robotic 3D actuations including gripping and transporting an object and a bidirectional locomotion.

As shown in Figure 3.1(a), the photo-curable precursor solution for EAH consists of 13.3 M of acrylic acid (AA) as a monomer, 145 mM of poly (ethylene glycol) diacrylate (PEGDA 700) as a cross-linker, and 43 mM of phenylbis(2,4,6-trimethylbenzoyl) phosphine oxide as a photo-initiator (PI). As demonstrated in our previous study [139], an EAH beam placed in electrolyte (phosphate-buffered saline, PBS) exhibits bending deformation when an electric field is applied (Figure 3.1(b)). The bending mechanism of EAHs can be explained by Flory's theory and Donnan equilibrium [123, 136, 140, 141]. When carboxylic groups in the EAH network are ionized in electrolyte, a large number of mobile cations are generated, making the EAH network anionic [142]. Osmotic pressure (π) is developed when the concentrations of mobile cations in the EAH network and in the surrounding electrolyte are different. Consequently, water molecules migrate through the EAH network until equilibrium swelling is reached. When an external electric field is applied, mobile cations are attracted to the cathode, creating a concentration gradient of mobile cations in the solution. Therefore, the balance of the osmotic pressure between two interfaces of the EAH is broken ($\pi_1 > \pi_2$), results in non-uniform swelling between the interfaces which causes the EAH to bend toward the cathode.
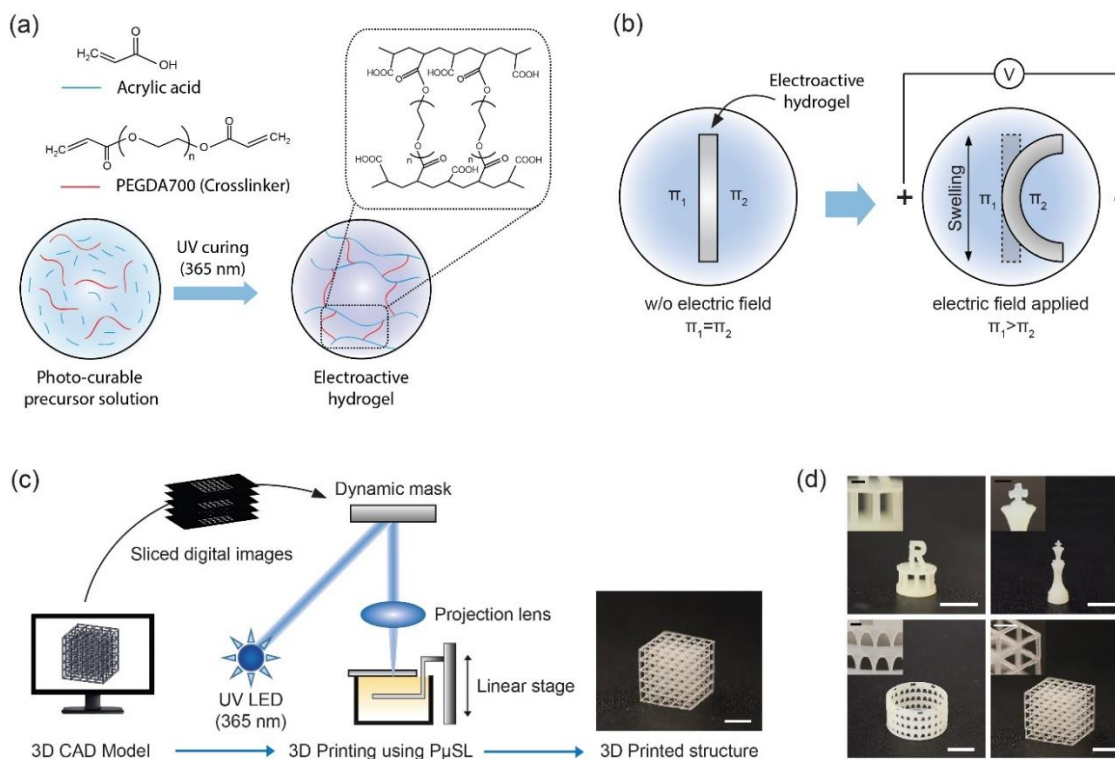
Figure 3.1. (a) EAH is cross-linked with AA and PEGDA 700. (b) The bending mechanism of EAH actuator can be explained by osmotic pressure (π) difference between the interfaces on the anode side (π_1) and the cathode side (π_2). The EAH bends toward the cathode by the swelling difference. (c) Schematic illustration of the PμSL process (scale bar: 5 mm). (d) 3D EAH structures printed using PμSL. The smallest feature size of the objects is 200 μm. (scale bars: 5 mm, scale bars for inset: 1 mm)

PμSL is employed to create 3D EAH structures, as shown in Figure 3.1(c). A 3D model is drawn using computer-aided-design (CAD) software and digitally sliced into a series of cross-sectional images of the model. Each digital image is sent to the dynamic mask to generate a patterned UV light, which is focused onto the surface of photo-curable precursor solution through a projection lens. Upon UV exposure, the liquid solution is

converted to a patterned solid layer. A 3D object is built layer upon layer by repeating this procedure for all the layers. (Figure 3.1(d)).

3.2. Materials and Methods

3.2.1. Materials

The photo-curable precursor solution used in this chapter consists of acrylic acid (AA, Sigma Aldrich), poly(ethylene glycol) diacrylate, Mn~700 (PEGDA 700, Sigma-Aldrich) as a cross-linker, and phenylbis (2,4,6-tri-methylbenzoyl) phosphine oxide (Sigma-Aldrich) as a photo-initiator (PI). 1 M phosphate-buffered saline (PBS, Sigma-Aldrich), DC regulated power supply (Tekpower), and 30 gauge platinum wires (uGems) as an electrode were used for electro-actuation. All materials and reagents were used as received.

3.2.2. Projection micro-stereolithography (PμSL)

A custom-made PμSL system was built using UV LED (365 nm) (Hamamatsu), digital micromirror device (DMD) (Texas Instruments), linear stage (Thorlabs), and convex lens (Convex lens, Thorlabs and extracted lens from commercial digital projector, Canon Realis SX50). System configuration is illustrated in Figure 3.1(c).

3.2.3. Curing depth study

To create a 3D structure using PµSL, we studied the energy dosage required to cure a certain depth of photo-curable precursor solution in the system. The test structure consisted of two side supports and five suspended bridges between the supports (Figure 3.2(a)). Enough vertical distance was given between bridges to prevent them from contacting with each other when they grow in vertical direction. Since each successive bridge was created with an increased energy dosage, each bridge grew to a different depth. The intensity of UV light was 23.4 mW cm^{-2}, and the exposure time for the bridges gradually increased from 0.5 s to 2.5 s in 0.5 s increments. The curing depth as a function of light energy dosage was measured using a microscope and plotted in Figure 3.2(b). As shown in the figure, the curing depth grows as the energy dosage increases, following the stereolithography working curve equation,

$$C_d = D_p \ln(E/E_c) \tag{3.1}$$

,where C_d is a depth of cure, and E is an exposure energy. Two key constants of the precursor solution, D_p and E_c, are characteristic cure depth and critical energy required to initiate curing, respectively [143]. A specific value of energy dosage required to create a layer with certain thickness can be determined based on the results of the curing depth study. On the basis of curing depth study, micro 3D printing using EAH was demonstrated as shown in Figure 3.1(d). All of the 3D EAH objects were printed with a layer thickness of 100 µm. About a 1 s curing time was applied to each layer.
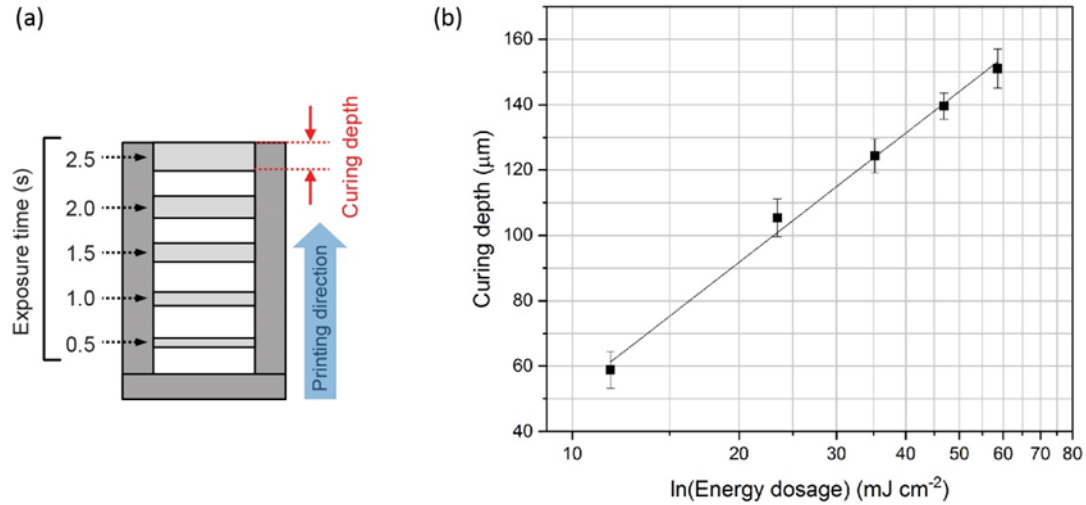
Figure 3.2. (a) 3D printed EAH structure for curing depth study. (b) PµSL curing depth working curve for EAH

3.2.4. Post-printing rinsing process

After printing, the samples were rinsed and stored in deionized water (DI water) at room temperature for 24 hours in order to rinse out the remaining un-cross-linked polymers in the network. Typical volume of the DI water used in rinsing is 60 ml for a sample having a volume of about 0.02 cm^3. Then the samples were put into a predetermined concentration of PBS solution (volume: 60 ml) and stored at room temperature for 24 hours to allow the samples to swell completely.

3.2.5. Swelling ratio measurement

The swelling ratio of disk samples with a diameter of 2 mm was obtained by optically measuring the diameter of the structure. After fabrication, all the samples were stored in

DI water for rinsing at room temperature for 24 hours. Then the samples were put into a

chamber filled with DI water and PBS solutions with different PBS concentrations. The

photo images of structures were taken after 24 hours using a digital camera coupled with a

microscope objective lens. Sample dimension was measured from the digital images using

Image J. In this chapter, we calculated the lengthwise swelling ratio as follows,

$$Lengthwise\ swelling\ ratio = \frac{D_s}{D_o} \tag{3.2}$$

,where D_s and D_o are the diameter of the swollen sample and original sample, respectively

(Figure 3.3). The original sample refers to the sample immediately after printing.
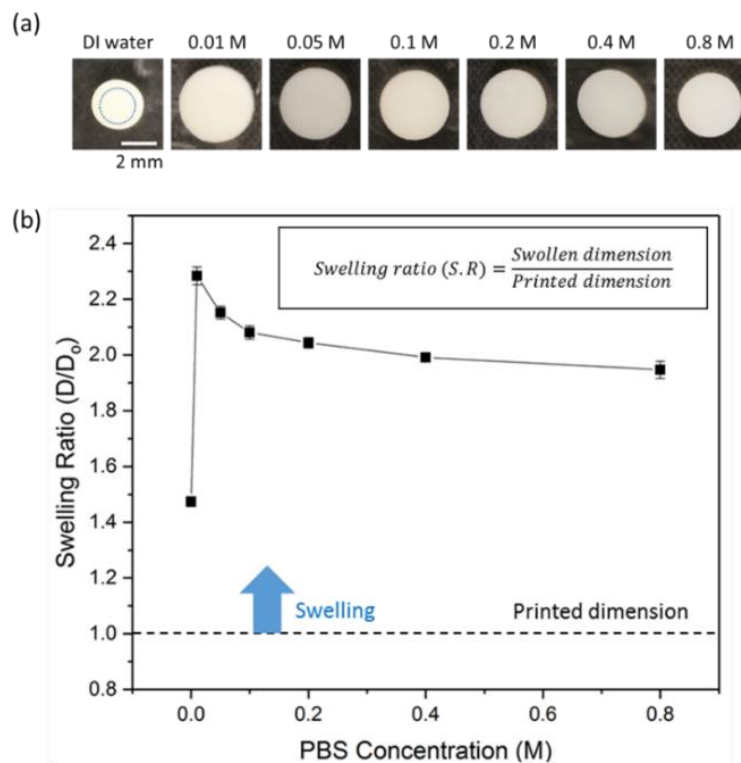
Figure 3.3. Swelling ratio study of printed EAH. The swelling ratio was defined as a ratio of swollen dimension to the printed dimension (diameter of 2 mm), or original dimension (dotted circle in Figure 3.3(a)). (a) The photo images of swollen samples at different PBS concentrations. (b) The swelling ratios of printed structure in DI water, 0.01 M, 0.05 M, 0.1 M, 0.2 M, 0.4 M, and 0.8 M PBS solution are 1.47, 2.28, 2.15, 2.08, 2.04, 1.99, and 1.95, respectively.

3.2.6. Water content measurement

Water content in the hydrogel can be obtained using the following equation:

$$Water\ Content\ (\%) = \frac{W_{swollen} - W_{dry}}{W_{swollen}} \times 100$$

(3.3)

where $W_{swollen}$ and W_{dry} are a weight of a gel sample in a fully swollen state and in a dry state, respectively. We prepared a set of samples and allowed them to swell in PBS solutions with different PBs concentrations for 12 hours. $W_{swollen}$ was obtained by measuring the weight of the swollen sample using a digital balance. Then, the sample was allowed to dry completely in an oven for 3 hours at 120 °C. Weight of the dry sample was measured using a digital balance. The water contents of printed structure in DI water, 0.01 M, 0.05 M, 0.1 M, 0.2 M, 0.4 M, and 0.8 M PBS solution are 70.8 %, 93.1 %, 90.0 %, 89.5 %, 89.2 %, 88.4 %, and 87.8 %, respectively (Figure 3.4).
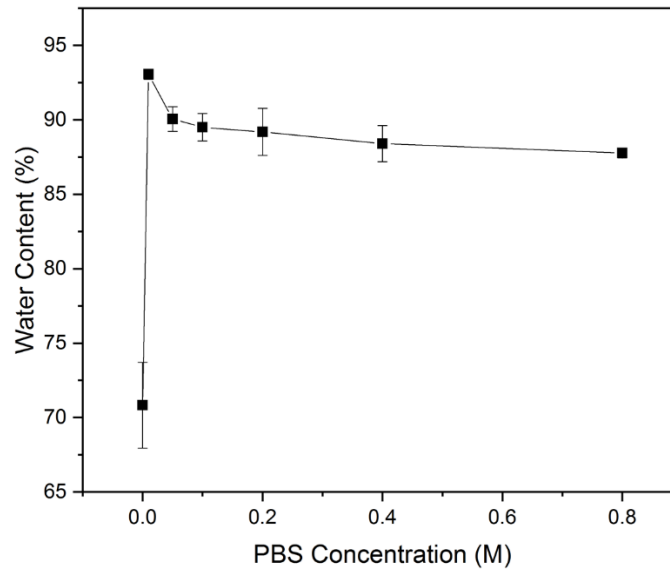
Figure 3.4. Water content of printed electroactive hydrogel

3.2.7. Electrical responsive actuation characterization

The beam structures with a width of 1 mm, height of 1 mm, and length of 20 mm were printed using PµSL to test the effects of PBS concentration and electric field strength on actuation. The width of the EAH beam was controlled to study the effect of characteristic thickness on actuation. After printing, all the samples were stored in DI water for post-printing rinsing. Then the samples were put into a predetermined concentration of PBS solution and stored at room temperature for 24 hours. To measure the actuation response to an electric field, two platinum electrodes spaced by 5.13 cm apart were submerged in the PBS, and a sample was placed in the middle of the two electrodes. An electric field was applied using a DC power supply. All actuation tests were recorded with a digital camera, and the bending curvature (1/R, inverse of a radius of curvature) was measured at 1 min or less intervals from the video using Image J (Figure 3.5).
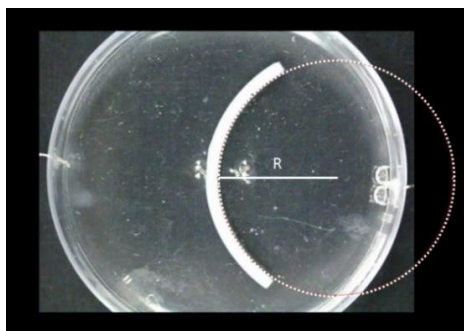
Figure 3.5. Bending curvature measurement using Image J

When testing the repetitive and reversible actuation, samples with a width of 1 mm, height of 1 mm, and length of 20 mm were prepared, and a voltage of 30 V was applied for 6 min to achieve the maximum bending curvature. After that, the following cycle was

performed repeatedly: a voltage of -30 V (applying the electric field in the opposite direction) was applied for 10 min, and then a voltage of 30 V was applied for 10 min.

3.2.8. Characteristic thickness and actuation time scale

To study the electro-actuation speed as a function of characteristic thickness (thickness of a EAH beam in the direction of an electric field), EAH beams with different thicknesses were printed using PµSL and tested in 0.05 M PBS solution with a voltage of 30 V (electric field: 0.58 V/mm). All actuation tests were recorded with a digital camera, and the bending curvature (1/R, inverse of a radius of curvature) was measured from the video using Image J. The data up to 98 % of the maximum bending curvature were used and fitted to the following equation [144]:

$$\kappa = \kappa_{\infty}(1 - e^{\frac{-t}{\tau}}) \tag{3.4}$$

where κ_{∞} is the equilibrium bending curvature, and t is the actuation time. The time constant τ is the step response time for the system to reach around 63.2% of its equilibrium bending curvature, representing the actuation time scale.

3.2.9. Bending strain calculation

The bending strain was calculated by a geometrical relationship based on Euler–Bernoulli beam theory.

$$e_{max} = \frac{tk}{2} \tag{3.5}$$

where ε_{max} is a maximum bending strain occurring at the bottom or top surface of the beam, t is the thickness of the swollen hydrogel beam, and κ is the inverse of a radius of curvature measured from the experiment κ is the inverse of a radius of curvature. Bending strain calculated from the results in Figure 3.8(c) is shown below (Figure 3.6). The maximum bending strains for all beams converge over time to a similar value of $\sim 4\%$, although their bending curvatures are significantly different (0.02 mm^{-1} for 2 mm thick beam vs. 0.17 mm^{-1} for 0.25 mm thick beam in Figure 3.8(c)). This is because bending strain is determined by an intrinsic material property and swelling pressure of the EAH, whereas bending curvature is highly dependent on the dimension of EAH structure.
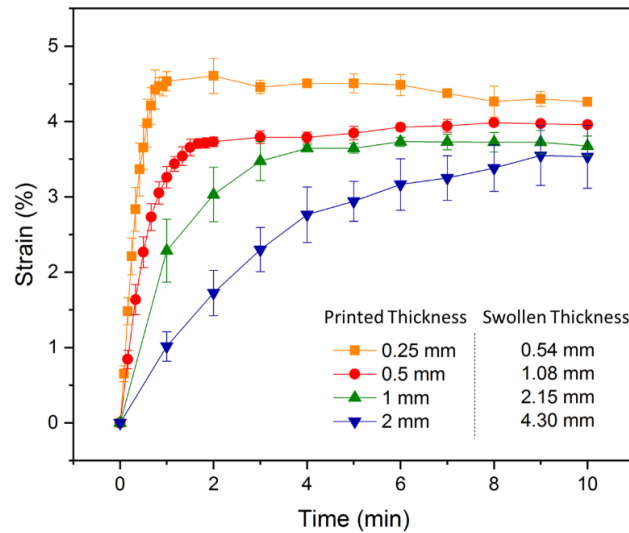
Figure 3.6. Bending strain on EAH beams calculated from bending curvature

3.2.10. Image analysis to determine the center of gravity of the locomotor

Original image shown in Figure 3.7(a) was first loaded into MATLAB and converted into grayscale. The loaded image was then passed through a customized binary filter that makes all pixels with intensity under a threshold black. The processed binary image is shown in Figure 3.7(b). Regions with high intensities became white and regions with low intensities became black. After obtaining size information of each white region in Figure 3.7(b), the region with biggest area was selected and all other regions were wiped as shown in Figure 3.7(c). Centroid of the region was extracted from the selected area using a MATLAB command 'regionprops' and marked in the original image shown in Figure 3.7(d).
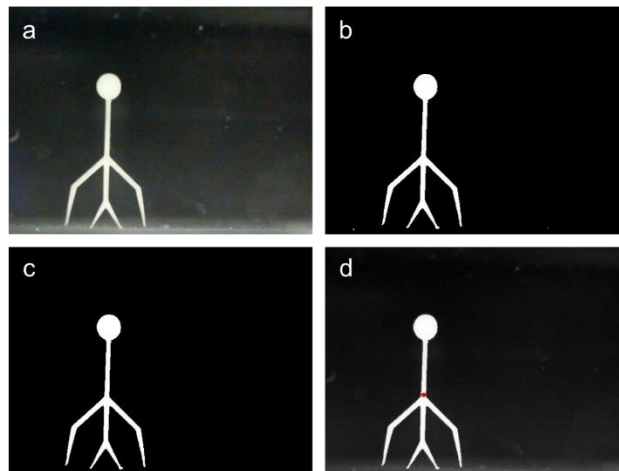
Figure 3.7. Image analysis for determining the center of gravity (a) original image, (b) black and white image after filter and conversion, (c) image with the region of largest area, (d) final overlaid image with an overlaid centroid mark

3.3. Results and Discussion

3.3.1. Bending deformation study using EAH beam

To better understand EAH actuation, we studied bending deformation of a 3D printed EAH beam for various PBS concentrations and electric field strengths. As illustrated in Figure 3.1(b), an EAH beam was placed between two electrodes in a PBS solution and waited until it reached equilibrium swelling (Figures 3.3 and 3.4). When the electric field was applied, the beam bent towards the cathode. Bending curvature (1/R, R is a radius of curvature) was measured during actuation.

3.3.1.1. Effect of PBS concentration on bending curvature

Since the concentration of mobile cation in the electrolyte induces osmotic pressure difference, we first studied the effect of PBS concentration on the bending deformation of the EAH. Using PµSL, EAH beams with 1 mm width, 1 mm thickness, and 20 mm length were 3D printed. Actuation tests were performed by applying an electric field of 0.58 V/mm for 6 different PBS concentrations and deionized (DI) water as a control. Figure 3.8(a) shows that the bending curvature increases with PBS concentration first and begins to decrease with the peak bending curvature occurring at 0.05 M. Smaller bending curvature at low PBS concentrations occurs because mobile ions are not sufficient enough to induce significant osmotic pressure. The decrease in bending curvature beyond 0.1 M is attributed to the fact that the mobile ion concentration gradient under the applied electric

field becomes less steep as PBS concentration increases. A 0.05 M PBS solution was used in all subsequent tests.

3.3.1.2. Effect of electric field strength on bending curvature

We also investigated the effect of electric field strength on EAH actuation. When an applied electric field strength increases, a steeper mobile ion concentration gradient is generated in the solution due to enhanced transfer rate of the mobile ions, resulting in larger bending deformation [145]. As shown in Figure 3.8(b), the bending curvature of 3D printed EAH increased linearly with electric field strength, suggesting that actuation control can be achieved through electric field control.
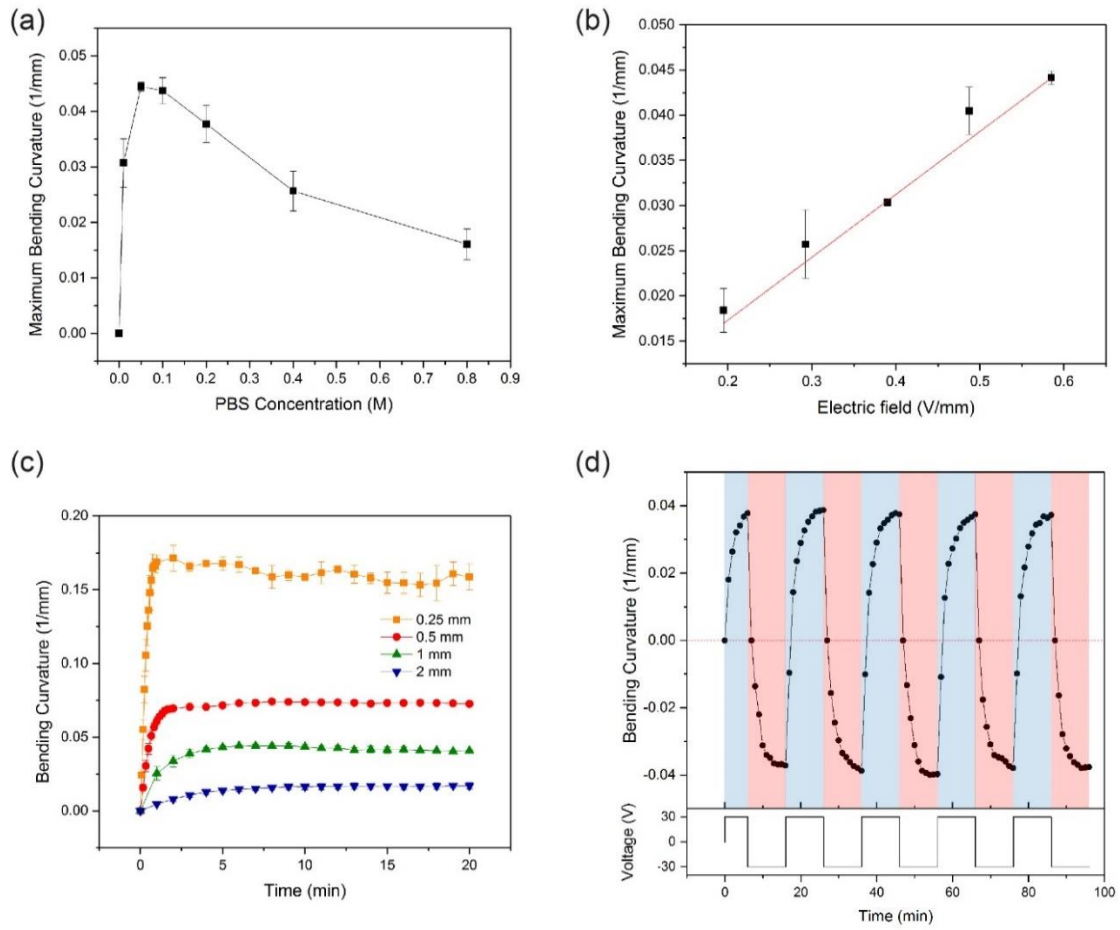
Figure 3.8. The bending deformation of 3D printed EAH beams. Effect of PBS concentration (a), electric field strength (b), and characteristic thickness of the EAH structure (c) on bending curvature. EAH beam shows the largest bending curvature in a 0.05 M PBS solution, and the bending curvature is proportional to the electric field strength. Also, a thinner EAH actuator exhibits larger and faster actuation than a thicker one. (d) The repeatability and reversibility of EAH actuator.

3.3.1.3. Effect of characteristic thickness of EAH structure on bending curvature

As gel swelling involves migration of water molecules within polymer network, actuation speed is closely related to the characteristic thickness of the gel [146, 147]. We printed four EAH beams with different thickness of 0.25 mm, 0.5 mm, 1 mm, and 2 mm, respectively, and performed the bending actuation tests for each beam. Figure 3.8(c) shows that thinner beams deformed into larger curvature. Furthermore, they reached their equilibrium bending curvature faster as beam thickness decreases. To quantify the actuation time scale, time evolution of the bending curvature was fitted to the response of the first-order system, $\kappa = \kappa_\infty (1 - e^{\frac{-t}{\tau}})$, where κ_∞ is an equilibrium bending curvature, t is time, and τ is a time constant characterizing actuation time scale (Figure 3.9). The result shows that the time constant increases linearly with the characteristic thickness of EAH beams, which is different from the quadratic relationship typically found in diffusive gel swelling. It is attributed to the fact that the molecular migration including ion transport and associated swelling occur in order to achieve electrical neutrality when it is disturbed by an electric field applied [123, 141]. This implies that actuation speed can be programmed by designing dimensions of an EAH structure. Therefore, 3D printing with precise dimensional control using PµSL can enable more diverse and complex actuations. In addition, when cyclic application of an electric field (0.58 V/mm) in alternating directions was given, the EAH beam changed the bending direction correspondingly without decay in bending curvature, demonstrating consistent, repeatable, and reversible actuation of the 3D printed EAH (Figure 3.8(d)).

Printed thickness (mm)	Swollen thickness (mm)	Time constant (τ)
0.25	0.54	19.1
0.5	1.08	48.5
1	2.15	89.4
2	4.30	184.3
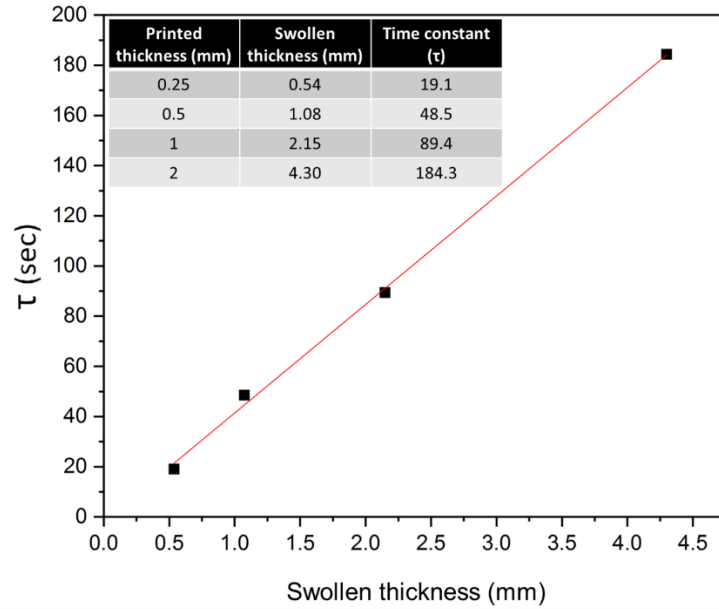
Figure 3.9. The actuation speed study with 3D printed beams fabricated with different thicknesses. Swollen thicknesses were calculated based on swelling ratio study, and a time constant as a function of swollen thickness was plotted. The inset table lists characteristic thickness of each EAH beam and corresponding time constant.

3.3.2. Soft robotic manipulation of 3D printed EAH actuators

Using the results from the above studies, we demonstrated soft robotic manipulation of 3D printed EAH actuators fabricated using PµSL. Figure 3.10(a) shows a gripper having two 'fingers'; two beams with different thicknesses, 0.25 mm (left) and 1 mm (right), respectively (Figure 3.11(a)). We chose these dimensions because the actuation time constants for these characteristic thicknesses are 19.1 s and 89.4 s, respectively, according to our analysis (Figure 3.9). Since the left finger should bend more and faster than the right one, gripping and releasing motions can be achieved when it is subjected to an electric field

(Figure 3.10(a)). Figure 3.10(b) shows time-lapse images of the 3D printed EAH gripper while it was picking up (positive field) and dropping down (negative field) a small ball. First, two straight fingers were brought to the ball without an electric field (Figure 3.10(b) (i)). When an electric field was applied, the left finger first bent inward fast and large enough while the slow right finger was still almost straight, allowing for gripping the ball (Figure 3.10(b) (ii)). The gripper was able to hold the ball even after 30 s because the right finger still barely bent (Figure 3.10(b) (iii-iv)), which is in good agreement with the previously obtained time constants. When an electric field in the opposite direction was applied, the left finger bent outward first to release the ball (Figure 3.10(b) (v-vi)).

An object transporter was also designed and fabricated. It consists of two sets of thin beam arrays ('hairs') and a thick beam ('bridge') connecting the two sets hairs (Figure 3.10(c)). The hairs have thickness of 0.25 mm, resulting in a fast actuation ($\tau = 19.1$ s). On the other hand, the bridge connecting the two sets of hairs is 2 mm in thickness, exhibiting a slow actuation ($\tau = 184.3$ s) (Figure 3.11(b)). Using these two different actuation time scales, we demonstrated transporting an object as shown in Figure 3.10(d). In the idle state, both the hairs and the bridge were straight (Figure 3.10(d) (i)). When an electric field was applied, the hairs were quickly bent toward the bridge, pushing the object (Figure 3.10(d) (ii)). While the electric field was kept constant, the bridge slowly started to bend. Consequently, the two sets of hair arrays were moved away from the object (Figure 3.10(d) (iii)). With the electric field applied in the reverse direction, the hairs first quickly changed their bending direction, yet without moving the object because it was already disengaged (Figure 3.10(d) (iv)). Later as the bridge slowly changed the bending direction, the two sets of hairs were brought back together (Figure 3.10(d) (v)). Since the hairs were bent outward

already when the object was engaged again, a large displacement of the object was achieved when electric field was applied again (Figure 3.10(d) (vi)) (Figure 3.12 for moving distance).
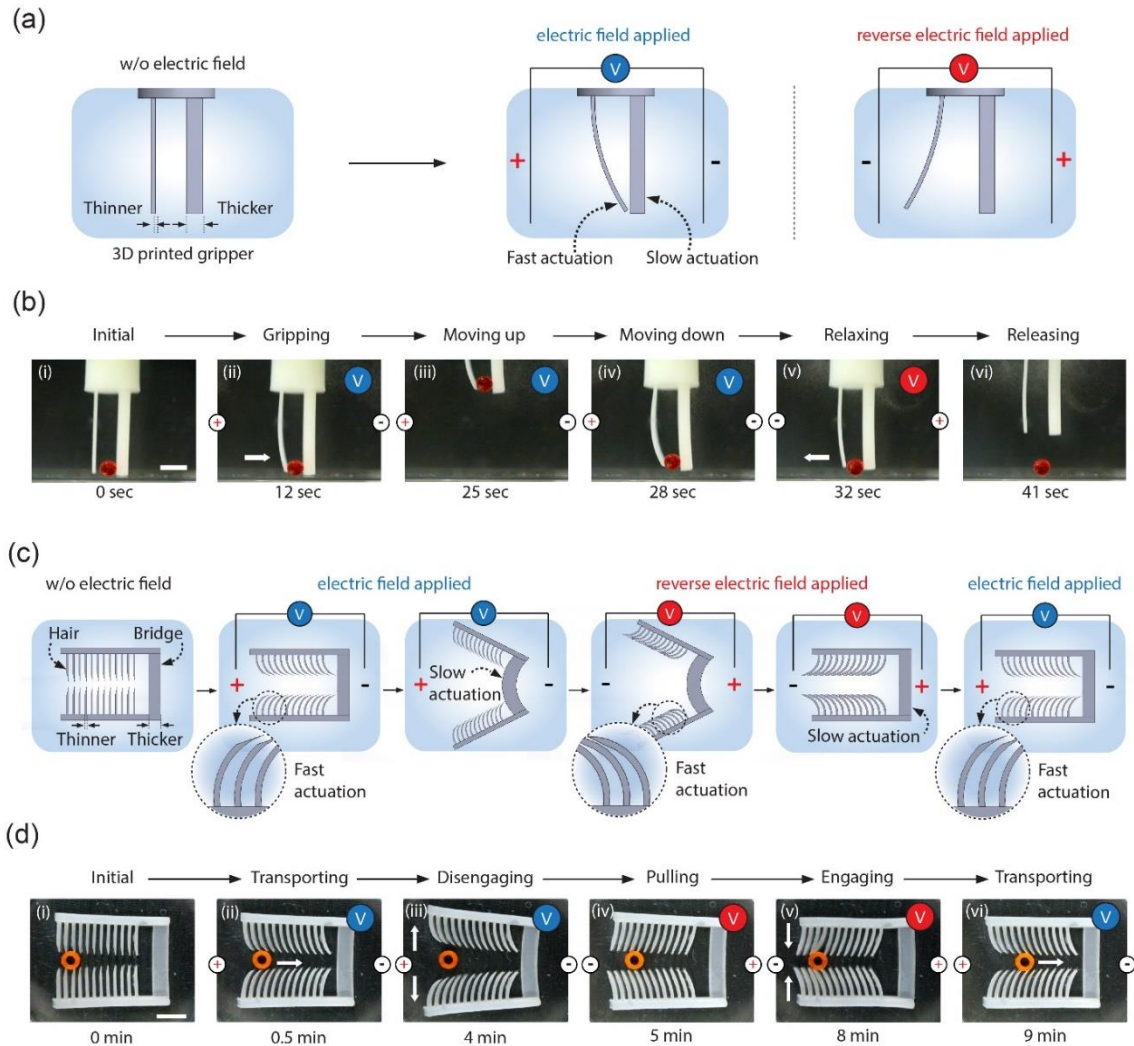
Figure 3.10. Soft Robotic Manipulation with 3D printed EAH. (a) Schematics of a gripper consisting of two beams with different thicknesses. (b) Gripping an object by applying the electric fields. (c) Schematics of a transporter consisting of hairs and a bridge with difference characteristic thicknesses. (d) Transporting an object by applying the electric fields in alternating directions. All scale bars indicate 5 mm.
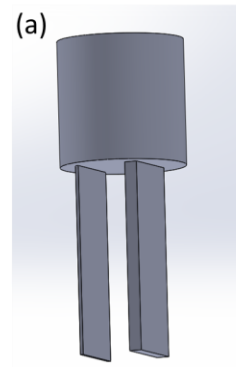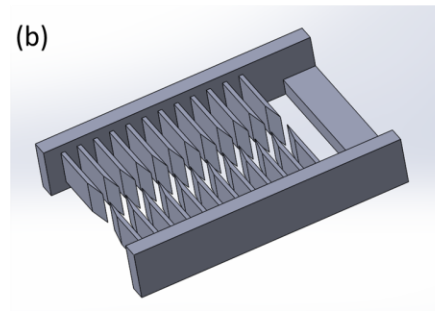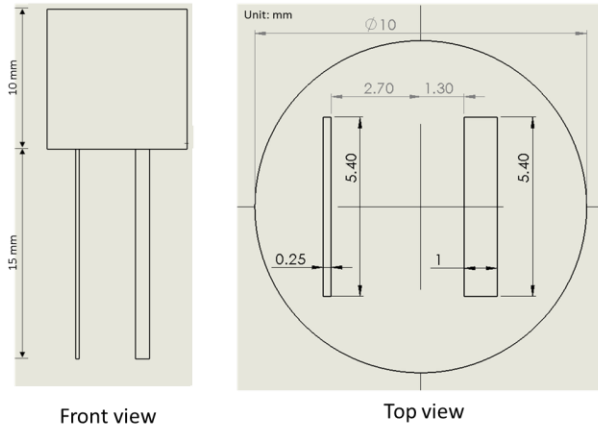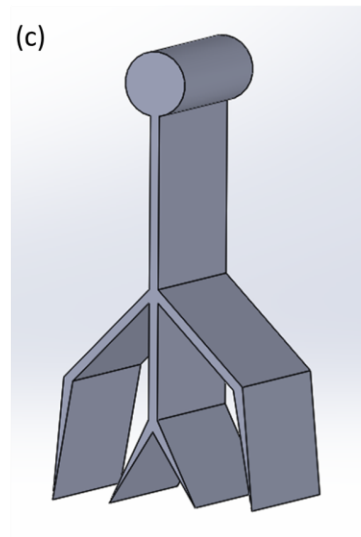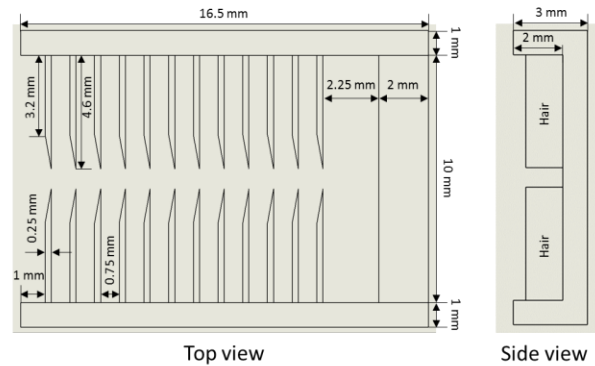
Figure 3.11. Printing dimensions of gripper (a), object transporter (b), and human-like locomotor (c)
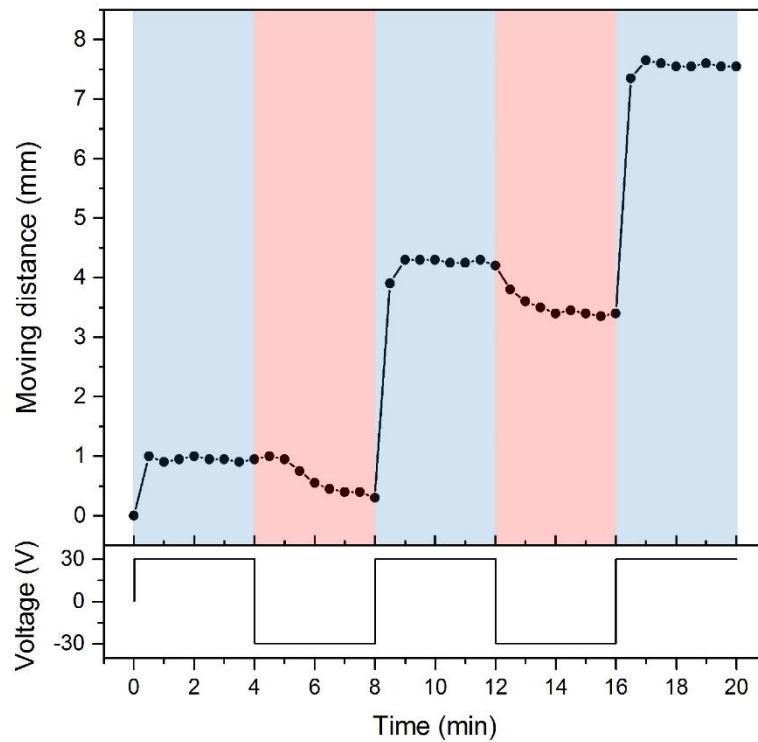
Figure 3.12. Moving distance of the object by applying electric fields, shown in Figure 3.10(c, d). The object moved about 8 mm for 20 min, with most of movements achieved when the electric field was applied (blue region). When a reverse electric field was applied, the object slightly moved in the opposite direction until it is fully disengaged from the transporter (red region).

3.3.3. Soft robotic locomotion of 3D printed EAH structure

Furthermore, untethered and bidirectional locomotion was achieved with a human-like 3D printed EAH structure, as shown in Figure 3.13(a). The height of the structure was 9.5 mm, and thickness of the 'body', 'legs', and 'arms' were 220 μm, 300 μm, and 220 μm, respectively (see Figure 3.11(c)). The walking motion of the structure was achieved by orchestrated bending actuation of the body, legs, and arms in response to an electric field. The center of gravity (CG) (symbol 'x' in Figure 3.13(a)) of the structure was initially at the center of the structure due to the symmetry, allowing the structure to stand upright on the two legs (Figure 3.13(a) (i)). When an electric field was applied, the CG quickly moved toward the rear (~10 s), shifting the anchoring point (Figure 3.13(a) (ii)) to the rear arm (red arm in Figure 3.13(a)). As the entire structure deformed while anchored with the rear arm, the front leg (blue leg in Figure 3.13(a)) slid forward (Figure 3.13(a) (iii)). When an electric field was removed, the structure began to return to its original shape, but the anchoring point was still placed on the rear arm (Figure 3.13(a) (iv)). Therefore, the front leg could further slide forward, moving the entire structure forward. Two minutes after the electric field was removed, the structure almost recovered its original shape and stood with its two legs again (Figure 3.13(a) (v)). Through digital image processing, we analyzed the relative position of CG and walking distance throughout the entire walking motion (Figure 3.7). Figure 3.13(b) shows the walking distance measured by tracking the position of the front leg (black line in Figure 3.13(b)) and the relative position of CG (green dashed line in Figure 3.13(b)) over time. The relative position of CG is defined as a ratio of the distance between the CG and the front leg to the distance between the CG and the rear arm. Therefore, the relative position of CG being greater than 1 means the CG located closer to

the rear arm and the relative position of CG being less than 1 means the CG being closer to the front leg. As shown in the Figure 3.13(b), while the structure walked forward about 12 mm for 21 min, majority of the walking stroke was achieved when the relative position of CG is greater than 1 (yellow box in Figure 3.13(c)), clearly showing the role of the CG position in walking. Furthermore, due to the symmetry, the structure changed the direction and walked to the same location (21 min to 42 min in Figure 3.13(b)) when the electric field direction was reversed. This bidirectional locomotion highlights the versatility and flexibility of electric field driven actuation of 3D printed EAHs. A 3D actuator with controlled mobility could potentially lead to a deployable multi-functional device for inspection, disease diagnostics, and drug detection/delivery, as well as unprecedented underwater soft robots mimicking bipedal locomotion of aquatic animals [148].
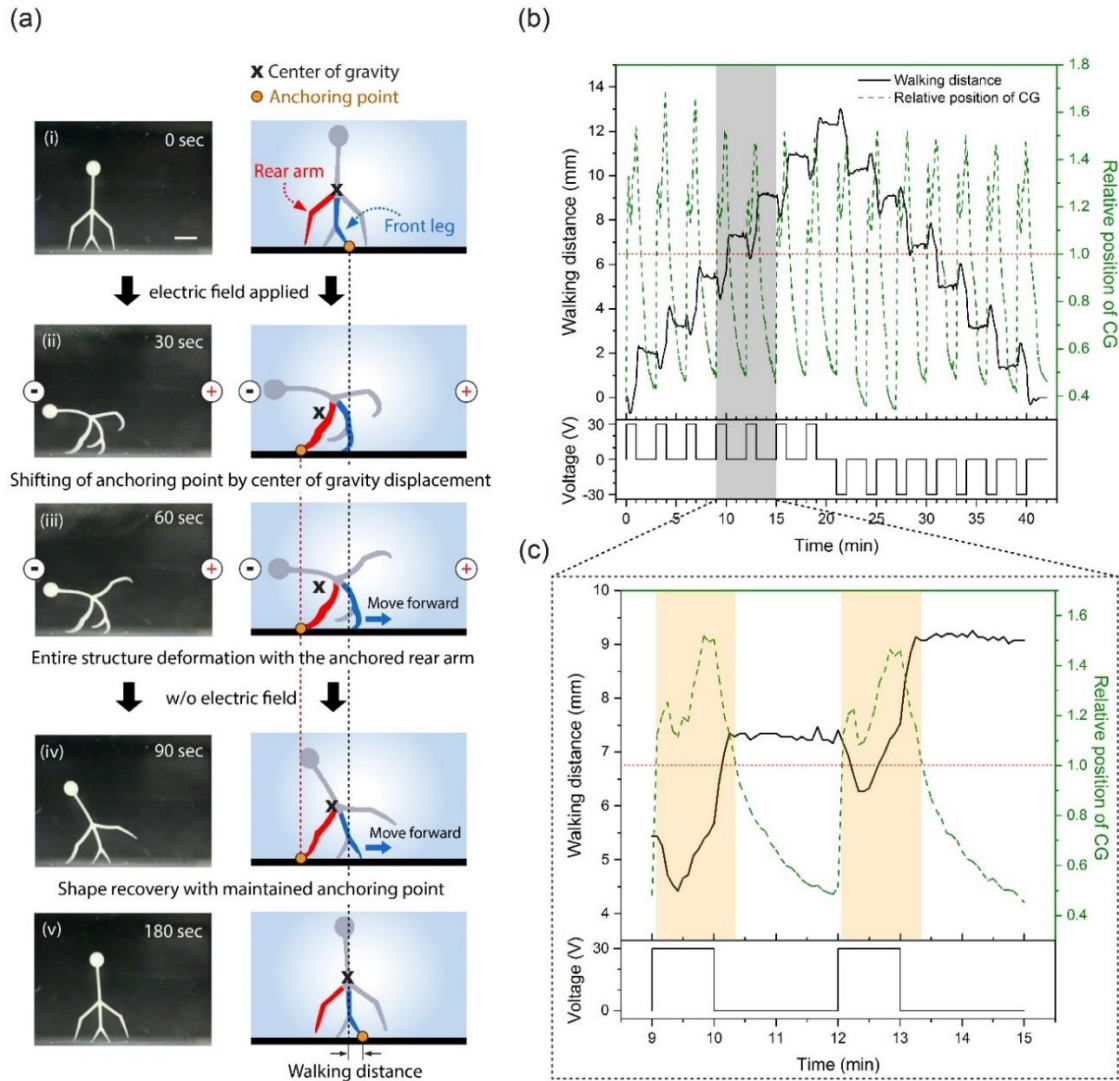
Figure 3.13. Bi-directional locomotion of a 3D printed human-like EAH structure. (a) Walking motion achieved by electric field driven actuation and corresponding shift of the CG. The CG and anchoring point are indicated by the symbol x and orange circle, respectively. (b) The walking distance (black solid line) and relative position of CG (green dashed line) according to electric fields. Red dashed line is a reference when the CG is located in the middle of the front leg and rear arm. (c) Enlarged graph for the range from 9 min to 15 min. Yellow box shows where the relative position of CG is greater than 1, indicating the CG is closer to the rear arm (Scale bar: 3 mm).

3.4. Conclusion

In conclusion, soft robotic manipulation and locomotion were achieved with 3D printed EAH structures fabricated using PµSL. We found that the 3D printed EAH exhibits the largest deformation in an electrolyte with a specific ionic strength (0.05 M PBS solution in this chapter) and the deformation is proportional to the applied electric field strength. We also found that actuation time scale is linearly proportional to the characteristic thickness. Utilizing the unique advantages enabled by high resolution 3D printing technique, PµSL, various complex actuations of EAH were achieved. We demonstrated soft robotic manipulation with two actuators, a gripper and an object transporter, printed with actuation elements having two different characteristic thicknesses and, therefore, actuation speeds. Also demonstrated was bi-directional locomotion of 3D printed EAH using deformation-induced shift of the center of gravity in an electric field. We believe that 3D printing of EAH with precise dimensional control could unlock otherwise untapped potential of electroactive hydrogels and may lead to various applications in soft robots, artificial muscles, and tissue engineering.

Chapter 4

Micro 3D Printing of Thermo-Responsive Soft Devices

4. Micro 3D Printing of Thermo-Responsive Soft Devices

4.1. Introduction

Stimuli-responsive hydrogels are polymeric networks that are capable of physical or chemical changes in response to environmental stimuli such as temperature, pH, and electric field [13, 149]. Various stimuli-responsive hydrogels and their applications have been explored over the past several decades. Poly(N-isopropylacrylamide) (PNIPAAm) hydrogels, one of the most widely used temperature-responsive hydrogels, have been extensively investigated and used in many applications such as microfluidic devices [150, 151], drug delivery vehicles [152, 153], cell culture substrates [154, 155], and soft actuators [156-159]. PNIPAAm exhibits a large and reversible volume change in water at its Lower Critical Solution Temperature (LCST, typically 32-35 °C) due to a coil-globule transition of the polymer network strands [122, 160]. At a temperature below its LCST, NIPAAm molecules in an aqueous environment show a hydrophilic behavior with an extended coil structure, which leads to water uptake and swelling. When the temperature increases above the LCST, however, hydrophobic groups become more active, causing the molecules to transform into a shape resembling a compact globule. Such a dramatic change induces the escape of entrapped water molecules from the hydrogel network, resulting in a significant reduction of volume.

Despite the growing attention to PNIPAAm and its wide range of applications, manufacturing techniques for PNIPAAm have been limited to simple two-dimensional (2D) fabrication methods such as molding and lithography, which impedes full utilization of its

unique material behavior. Recently, there have been some efforts on creating a 3D shape from a 2D PNIPAAm sheet using an origami approach [20, 21, 161]. However, achieving a high resolution and high aspect ratio PNIPAAm geometry still remains challenging. More recently, additive manufacturing of PNIPAAm has been reported using a commercial extrusion-based 3D printer, but it is still limited to simple 2D extrusion geometries and low resolution [137]. Other high resolution 3D micro-manufacturing techniques including three-dimensional laser chemical vapor deposition (3D-LCVD) [162], electrochemical fabrication (EFAB) [163], and micro-stereolithography (μSL) [164] also have drawbacks such as long fabrication time, high cost, and limited sets of available materials.

In this chapter, we present high resolution 3D printing of PNIPAAm using projection micro-stereolithography (PμSL). PμSL is a lithography-based additive manufacturing technique that is fast, inexpensive, and flexible in material selection [106, 107]. A 3D model is generated using computer-aided-design (CAD) software and digitally sliced into a series of cross-sectional images of the 3D model. Each digital image is transferred to a digital mask to optically pattern ultra-violet (UV) light, which is then projected through a reduction lens and focused on the surface of photo-curable resin. The patterned UV light converts liquid resin to a solid layer through photo-polymerization. Once a layer is formed, the linear stage drops the sample holder on which the object is built in order to introduce fresh liquid resin for the next layer. The subsequent layer is polymerized in the same manner on top of the preceding layer. This process is repeated until all the layers are complete to build the 3D object (Figures 4.1(a) and 4.2).

Since PμSL uses projection lithography, an entire layer is polymerized by a single UV illumination of a few seconds. Therefore, fabrication speed is much faster than serial

processing techniques where a nozzle or a laser beam has to be raster-scanned for each layer. Also, the use of a reconfigurable digital photo mask eliminates the need for multiple physical photo masks which would otherwise make the fabrication process very expensive and time-consuming. PμSL is also compatible with various photo-curable materials including poly (ethylene glycol) (PEG), poly lactic acid (PLA), poly(caprolactone) (PCL), and their copolymers [106-109, 165]. In this chapter, we demonstrate the 3D printing of PNIPAAm using PμSL and the reversible deformation of various 3D printed PNIPAAm micro-structures. We also investigate the effects of PμSL process parameters as well as polymer resin composition on the temperature dependent swelling behavior of 3D printed PNIPAAm hydrogel. Also demonstrated is the sequential deformation of a 3D printed PNIPAAm structure by selective incorporation of an ionic monomer that shifts the swelling transition temperature of PNIPAAm.
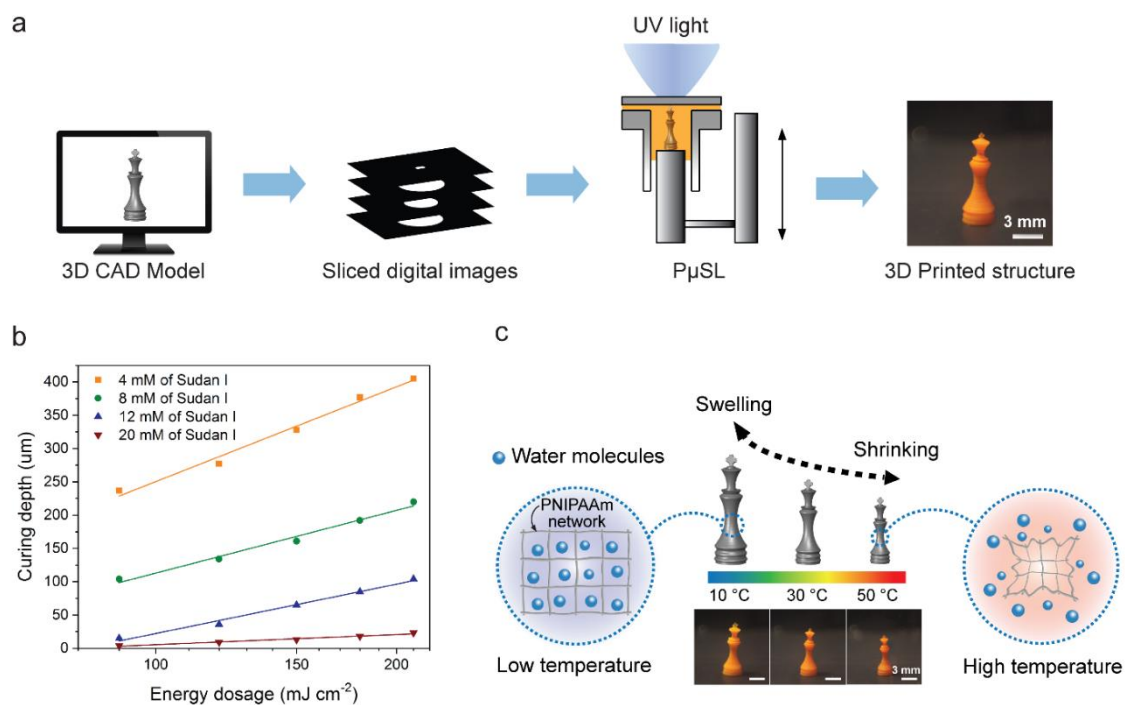
Figure 4.1. 3D printing of temperature responsive hydrogel using PµSL: (a) Schematic illustration of the PµSL process. (b) The result of curing depth study. Curing depth tends to decrease with increasing PA concentration. Also, higher PA concentration results in slower growth of a layer with increasing energy dosage (The slope of the plot decreases with increasing PA concentration.). (c) Temperature responsive swelling of 3D printed PNIPAAm hydrogel structure
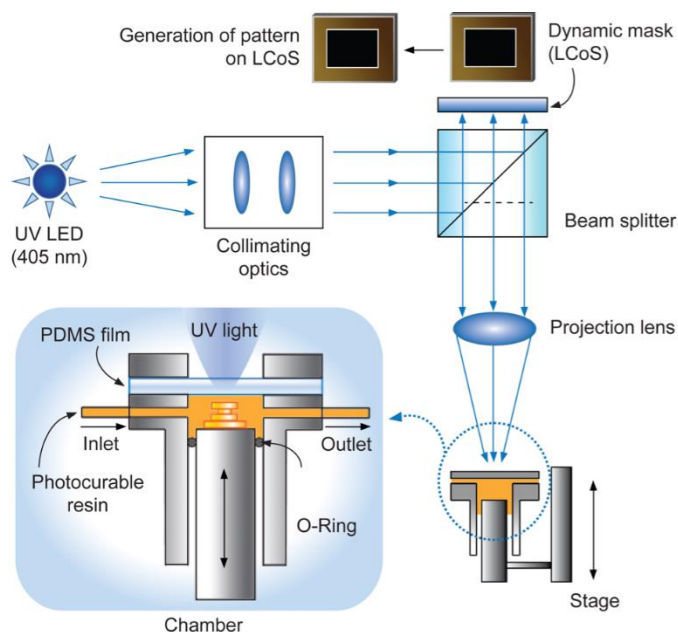
Figure 4.2. Schematic drawing of the high resolution PµSL system

4.2. Materials and Methods

4.2.1. Materials

The resin used in this chapter consists of N-isopropylacrylamide (NIPAAm) (Fisher Scientific), N,N'-Methylene-bis(acrylamide) (Sigma-Aldrich) as a cross-linker, Phenylbis (2,4,6-tri-methylbenzoyl) phosphine oxide (Sigma-Aldrich) as a PI, Sudan I (Sigma-Aldrich) as a PA, and a fluorescent dye Rhodamine B (Sigma-Aldrich). An ionic monomer Methacryl-amidopropyl-trimethyl-ammonium Chloride (MAPTAC) (Sigma-Aldrich) was used for the transition temperature study. Ethanol was used as a solvent in all resins. All materials were used as received.

4.2.2. Projection Micro-StereoLithography (PμSL)

A custom-made PμSL system was built using the following major components; Liquid crystal on silicon (LCoS) as a digital dynamic mask, a projection lens (Carl Zeiss), a UV LED (405 nm, Innovations in Optics), a linear stage (Newport Corporation), and collimation optics (Thorlabs). An LCoS digital dynamic mask was extracted from a commercial digital projector (Cannon) [166].

4.2.3. Curing depth study

To prepare the photo-curable resins for curing depth study, 6.2 M of NIPAAm was dissolved in ethanol with 324 mM of cross-linker, 47.8 mM of PI, and 2.1 mM of Rhodamine B. Then, 4, 8, 12, or 20 mM of Sudan I was added to the resin as a PA to confirm the effect of PA concentration on curing depth. The prepared resin was filled into a glass mold which has 1 mm thickness, and the rectangular images were projected with 30.0 mW cm^{-2} of light intensity through a transparent glass mold into PNIPAAm resin for different curing times (Figure 4.3). Due to the curing time difference, rectangular structures of different heights were grown from the glass surface. To measure the height of the structures on glass slide precisely, an AFM (NX-10, Park systems Corp.) was used in contact mode.
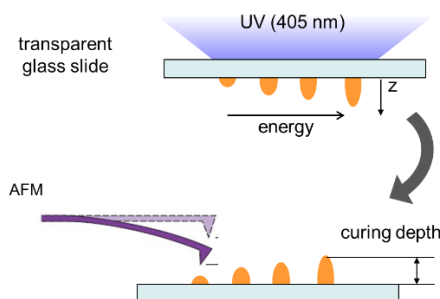
Figure 4.3. Schematic drawing of the process used for the curing depth study using an AFM

4.2.4. Sample fabrication using a UV oven

The photo-curable resins were prepared without PA and Rhodamine B to fabricate a fully cross-linked structure. The resins were cured with more than enough light energy (6000 mJ cm^{-2}) using a UV oven (CL-1000L, UVP, 365 nm). First, thin films of PNIAAm were cured with a transparent glass mold having a 360 μm thickness. PNIPAAm disks were made from these films using a punch tool with a diameter of 4.8 mm. The disks were rinsed in deionized water (DI water) at 15 °C overnight.

4.2.5. Temperature responsive swelling characterization

Based on the curing depth study, the photo-curable resin which has 6.2 M of NIPAAm, 324 mM of cross-linker, 47.8 mM of PI, 12 mM of PA, and 2.1 mM of Rhodamine B was chosen as a base resin. In addition, a light intensity of 30.0 mW cm^{-2}, curing time of 10 sec, and layer thickness of 30 μm, were chosen as standard process parameters. To study the

effect of polymer resin composition, two or three chemical concentrations were modified for each study. In addition, 0.2 and 0.4 M of MAPTAC were added to the base resin to study the effect of ionic monomer on transition temperature (Tables 4.1 and 4.2). The light intensity and layer thickness were controlled to study the effect of PµSL process parameters on swelling of 3D printed PNIPAAm (Table 4.3). The cylindrical samples with a diameter of 1.6 mm and a height of 3.6 mm were printed for the layer thickness study, and disk samples of a diameter of 1.6 mm and a thickness of 300 µm were printed for the rest of the swelling characterization.

Table 4.1. Chemical composition of different polymer resins. Ethanol was used as a solvent for all solutions.

Study	Chemical composition						
	NIPAAm (M)	Cross-linker (mM)	Molar ratio of cross-linker to monomer	PI (mM)	PA (mM)	Rhodamine B (mM)	MAPTAC (M)
Curing depth (Sec. 4.3.1)	6.2	324	0.05	47.8	4 8 12 20	2.1	-
Cross-linker (Molar ratio) (Sec. 4.3.2.1)	6.2	65 130 195 259 324	0.01 0.02 0.03 0.04 0.05	47.8	12	2.1	-
NIPAAm concentration (Sec. 4.3.2.1)	2.6 4.4 6.2 8.0 9.7	139 232 324 417 510	0.05	20.5 34.1 47.8 61.4 75.1	12	2.1	-
Light intensity (Sec. 4.3.2.2)	6.2	324	0.05	47.8	12	2.1	-
Layer thickness (Sec. 4.3.2.3)	6.2	324	0.05	47.8	12	2.1	-
Ionic monomer, MAPTAC (Sec. 4.3.2.4)	6.2	324	0.05	47.8	12	2.1	- 0.2 0.4
Gripper (Sec. 4.3.3)	6.2	324	0.05	47.8	12	2.1	-
Dumbbell (Sec. 4.3.3)	6.2	259 324	0.04 0.05	47.8	12	2.1	- 0.4

Table 4.2. Chemical composition of different polymer resins and the quantities of each component

Study	Chemical composition						
	Ethanol (mL)	NIPAAm (g)	Cross-linker (g)	PI (g)	PA (g)	Rhodamine B (g)	MAPTAC (mL)
Curing depth (Sec. 4.3.1)	100	70	5	2	0.1 0.2 0.3 0.4	0.1	-
Cross-linker (Molar ratio) (Sec. 4.3.2.1)	100	70	1 2 3 4 5	2	0.3	0.1	-
NIPAAm concentration (Sec. 4.3.2.1)	100	30 50 70 90 110	2.1 3.6 5.0 6.4 7.9	0.9 1.4 2.0 2.6 3.1	0.3	0.1	-
Light intensity (Sec. 4.3.2.2)	100	70	5	2	0.3	0.1	-
Layer thickness (Sec. 4.3.2.3)	100	70	5	2	0.3	0.1	-
Ionic monomer, MAPTAC (Sec. 4.3.2.4)	100	70	5	2	0.3	0.1	- 4.2 8.4
Gripper (Sec. 4.3.3)	100	70	5	2	0.3	0.1	-
Dumbbell (Sec. 4.3.3)	100	70	4 5	2	0.3	0.1	- 8.4

Table 4.3. PµSL process parameters

Study	PµSL process parameters			
	Light intensity (mW cm^{-2})	Curing time (sec)	Layer thickness (µm)	Number of layers
Molar ratio (Sec. 4.3.2.1)	30	10	30	10
NIPAAm concentration (Sec. 4.3.2.1)	30	20 (for 2.6 M NIPAAm) 15 (for 4.4 M NIPAAm) 10 (for 6.2 M NIPAAm) 8 (for 8.0 M NIPAAm) 5.5 (for 9.7 M NIPAAm)	30	10
Light intensity (Sec. 4.3.2.2)	4.3 (Grayscale 100) 7.3 (Grayscale 150) 14.3 (Grayscale 200) 30 (Grayscale 255)	4	30	10
Layer thickness (Sec. 4.3.2.3)	30	10	30 60 90 120	120 60 40 30
Ionic monomer (MAPTAC) (Sec. 4.3.2.4)	30	10	30	10
Gripper (Sec. 4.3.3)	4.3 (Grayscale 100) 30 (Grayscale 255)	4	30	95
Dumbbell (Sec. 4.3.3)	30	10	30	154

4.2.6. Post-printing rinsing process

After fabrication, the samples were rinsed and stored in DI water at 15 $^{\circ}$C overnight in order to exchange the ethanol and remaining uncross-linked polymers in the network with DI water. Typical volume of the DI water used in rinsing is 60 ml for a sample having a volume of about 6 x 10^{-4} cm^3. At this low temperature of 15 $^{\circ}$C, PNIPAAm becomes hydrophilic and thus allows water molecules to diffuse into the cross-linked network to replace ethanol. With an abundant amount of rinsing water, ethanol in the printed PNIPAAm is effectively diluted and replaced with water, which results in large swelling of PNIPAAm.

4.2.7. Swelling ratio measurement

The swelling ratio of PNIPAAm samples was obtained by optically measuring the diameter or length of the structure. After fabrication, all the samples were stored in DI water at 15 $^{\circ}$C overnight for post-printing rinsing. Then the samples were put into a temperature-controlled chamber filled with DI water. The chamber has a transparent glass window through which temperature dependent deformation of samples were observed and measured. The temperature of water in the chamber were controlled within a range from 10 $^{\circ}$C to 90 $^{\circ}$C. The rate of temperature change was 0.4 $^{\circ}$C/min. The photo images of structures were taken at every 5 $^{\circ}$C using a digital camera coupled with a microscope objective lens. Sample dimension was measured from the digital images using image analysis software, Image J.

4.3. Results and Discussion

4.3.1. 3D Printing of PNIPAAm

All photo-curable PNIPAAm resins used in this work were prepared by dissolving NIPAAm as a monomer, N,N'-Methylene-bis(acrylamide) as a cross-linker, and Phenylbis (2,4,6-tri-methylbenzoyl) phosphine oxide as a photo-initiator (PI) that initiates a photo-polymerization upon light absorption, all of which were dissolved in ethanol as a base solvent. In addition, Sudan I was added in the resins as a photo-absorber (PA) that controls the penetration depth of light. Rhodamine B was also added as a dye for visualization of 3D printed PNIPAAm structures. Table 4.1 provides the chemical components of the photo-curable resins used in each study and their concentrations. In addition, the exact quantities of the components in the resins are provided in Table 4.2.

Lateral resolution of the PµSL system is determined by the optics of the PµSL system and the polymerization kinetics of PNIPAAm. With the current PµSL system and the PNIPAAm resin, a lateral resolution of around 160 µm was achieved for PNIPAAm hydrogel (Figure 4.4). In order to build a 3D object in a layer-by-layer fashion, we also studied how a layer of PNIPAAm hydrogel is polymerized and grows in the vertical direction. The depth of photo-polymerization, or curing depth, was measured as a function of light energy dosage. To study the curing depth, rectangular images were projected through a transparent glass slide into PNIPAAm resin for different curing times (Figure 4.3). Since polymerization begins from the surface of the glass slide and grows with exposure time, the curing depth can be obtained by measuring the height of resulting

rectangular pattern using atomic force microscope (AFM). The same experiment was repeated with PNIPAAm resins having different concentration of PA. As shown in Figure 4.1(b), the curing depth of PNIPAAm hydrogel can be prescribed by controlling the light energy dosage and PA concentration in the resin.
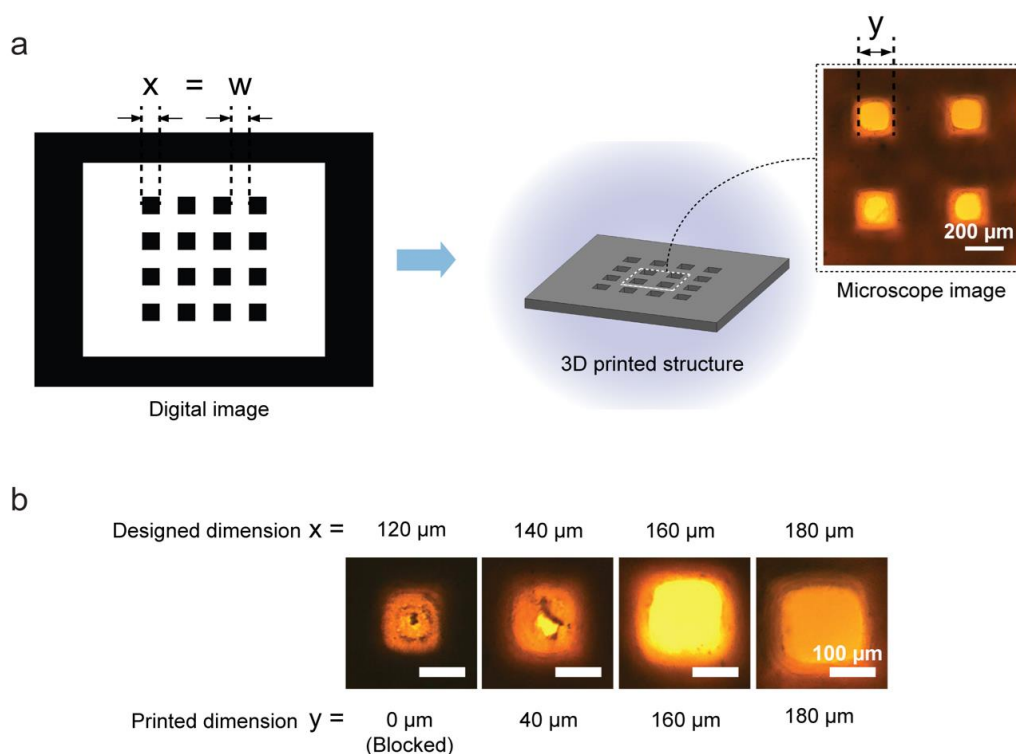
Figure 4.4. Lateral resolution test for PNIPAAm 3D printing. (a) A digital image with multiple grid lines was projected to test the minimum possible feature size. The width of the grid lines (*w*) and that of holes (*x*) were identical in the digital image. The width of the holes in the printed structure (*y*) was measured using a microscope. (b) To determine the lateral resolution, four digital images with different width of holes and lines, 120, 140, 160, and 180 μm, were prepared and projected to create the structures. The printed hole sizes were 0, 40, 160, and 180 μm, respectively. The results show that the lateral resolution of PµSL with PNIPAAm hydrogel is around 160 μm.

Based on the process characteristics determined by the above experiments, 3D printing of PNIPAAm was demonstrated as shown in Figure 4.1(c). The height of the object is 7.83 mm, consisting of 261 layers having a thickness of 30 μm. A nine second curing time was used for each layer, making the total fabrication time of 65 min. The smallest lateral feature size of the object is 163 μm. After printing, the PNIPAAm micro-structure was stored in DI water at 15 °C overnight for post-printing rinsing. During that time, the ethanol inside the structure is replaced with DI water, and uncross-linked polymers and other chemical components in the resin are removed from the printed structure. Therefore, no further cross-linking occurs with time after rinsing. To confirm the temperature dependent deformation of the printed structure, it was put into a temperature-controlled water chamber while the deformation of structure was recorded. As shown in Figure 4.1(c), the 3D PNIPAAm hydrogel structure was swollen to a height of 9.63 mm at 10 °C, which then shrank to a height of 7.41 mm when the temperature was raised to 50 °C. The rate of temperature increase and that of temperature decrease were 1.33 °C/min and 0.67 °C/min, respectively. Reversible swelling deformation was observed when the temperature was dropped to 10 °C again, demonstrating that swelling deformation of a 3D PNIPAAm hydrogel printed by PμSL can be controlled by environmental temperature.

4.3.2. Controlling temperature responsive swelling of PNIPAAm hydrogel

The key attribute of PNIPAAm hydrogel is its ability to change its degree of swelling in response to temperature change. To quantify this, we use the swelling ratio (SR) in this study defined as a ratio of swollen length to the original length (as fabricated). It is important to note that the reference dimension is not the dimension of the hydrogel in the dry state, but the original dimension at the moment of polymerization (or printing). For example, the SR is greater than 1 when a PNIPAAm hydrogel swells and gets bigger than the printed dimension at low temperature, and the SR is less than 1 when it shrinks and becomes smaller than the printed dimension at high temperature.

To observe the overall swelling behavior of PNIPAAm in response to temperature, disk-shaped samples with a diameter of 1.6 mm and a thickness of 300 μm were printed using PμSL. The NIPAAm and cross-linker concentrations of the polymer resin used in this study were 2.6 M and 139 mM in ethanol, respectively. As shown in Figure 4.5(a), swelling ratio at a low temperature of 10 °C is 1.42.
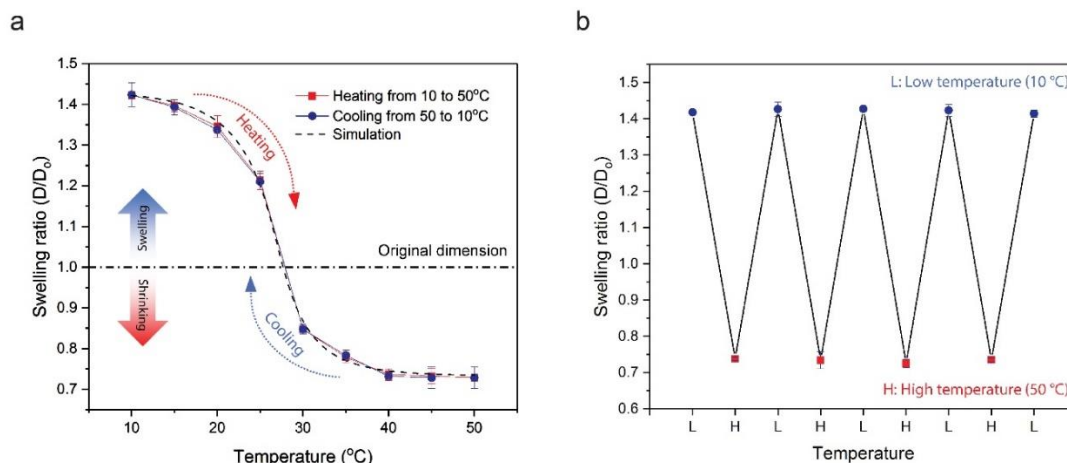
Figure 4.5. Reversible temperature dependent swelling/shrinkage of PNIPAAm hydrogel. (a) Equilibrium swelling of PNIPAAm depends on temperature. Swelling ratios of PNIPAAm during a heating cycle match well with those from a cooling cycles. Also, experimental results are in a good agreement with the equilibrium swelling simulation result. (b) Low temperature swelling and high temperature shrinkage of PNIPAAm occurred repeatedly when heated and cooled alternately between 10 °C and 50 °C.

It shows a 42 % increase in length (or 186 % in volume) compared to the original dimensions of the printed disk sample. On the other hand, the swelling ratio is 0.73 at a high temperature of 50 °C, which indicates a 27 % decrease in length (or 61 % in volume) from the printed dimension of the sample. Furthermore, the swelling ratio was measured at every 5 °C while increasing temperature from 10 °C to 50 °C and subsequently decreasing temperature back to 10 °C. The temperature was changed by 5 °C every 3 hours to ensure swelling reaches an equilibrium state. The result shows that swelling ratios in the heating and cooling cycles are well-overlapped. Also, the maximum and minimum swelling ratios remain constant after multiple cycles of heating and cooling (Figure 4.5(b)),

showing that temperature dependent swelling of PNIPAAm is reversible and repeatable. Thermally responsive gel behavior is analyzed in the context of the theoretical model in the recent study [167], showing good agreement with experimental data (Figure 4.5(a)).

Thermally responsive gel behavior is analyzed in the context of the theoretical model in the recent study [167], and for brevity, only the main points are repeated here. Since the experiment was performed over a very long time, equilibrium is assumed both mechanically and chemically, therefore inertia and diffusion are not considered. Further, since the body is not constrained, we consider stress free swelling, so that the deformation will be isotropic. Under these conditions, the model reduces to a nonlinear scalar equation for the swelling ratio

$$f(\varphi) = R\theta(\ln(1 - \varphi) + \varphi + \chi\varphi^2) + \Omega G(\varphi^{1/3} - \varphi) = 0 \tag{4.1}$$

Here, φ is the polymer volume fraction (a measure of swelling ratio), R is the gas constant, θ the absolute temperature, Ω the molar volume, G the shear modulus, and lastly the interaction parameter χ characterizes the interaction between the polymer and solvent. In the model, the key to the thermally responsive swelling is χ, which is based on the mixing contribution to the behavior of the material. The specific form chosen for this work comes from a recent study [167], and has the form

$$\chi(\theta) = \frac{1}{2}(\chi_L + \chi_H) - \frac{1}{2}(\chi_L - \chi_H)\tanh\left(\frac{\theta - \theta_T}{\Delta}\right) \tag{4.2}$$

Here, χ_L is the value at a "low" temperature, χ_H the value at a "high" temperature, θ_T the transition temperature, and Δ the width of the transition. For calibration, we need to assume the shear modulus, and since we do not currently have reliable data, we have

assumed the shear modulus is 0.5 MPa. Further, since the data shows a swelling ratio less than one at high temperatures, the structure was fabricated with some initial amount of fluid inside. We have estimated that initial swelling at $\varphi_0 = 0.3772$ such that the polymer is 95% dry in the high temperature condition. Therefore, knowing φ from analysis of the experimental data, we are able to solve the nonlinear equation for $\chi(\theta)$, which is then calibrated as shown in the figure below, which fits very well.
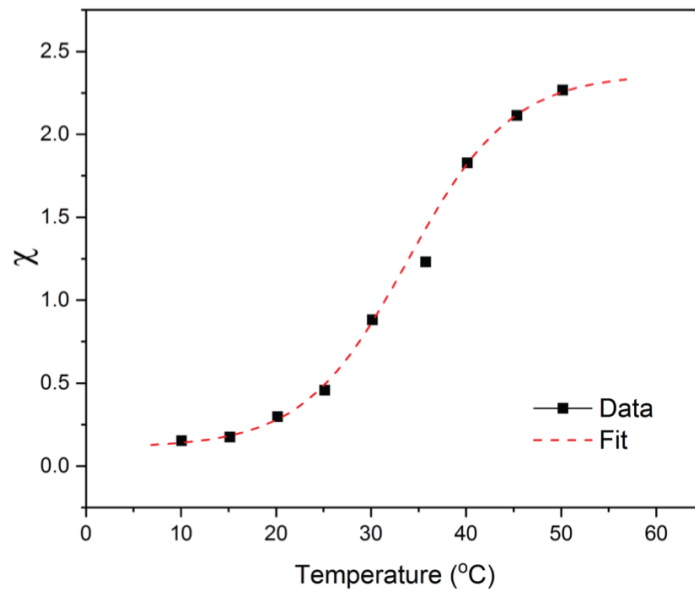
Figure 4.6. Analysis of the experimental data with χ

Next, with $\chi(\theta)$ calibrated to the data for PNIPAAm, we are able to use a finite element procedure to simulate the behavior of various geometries and thermo-mechanical loading conditions. The full set of material parameters is given in below table.

Table 4.4. Material parameters for simulation

Parameter	Value
Gas constant	$R = 8.31457$ J/(mol K)
Shear modulus	$G = 0.5$MPa
Molar volume	$\Omega = 18.0695$ cm^3/mol
Interaction parameter at low temperature	$\chi_L = 0.112$
Interaction parameter at high temperature	$\chi_H = 2.365$
Transition temperature	$\theta_T = 307$K
Width of the transition	$\Delta = 10.94$K

Thermodynamically, the equilibrium swelling ratio of a gel in a solvent is governed by the cross-linking density of the polymer network and its interaction with that solvent. Since we use photo-polymerization to cure PNIPAAm hydrogels using PμSL, the temperature responsive swelling behavior of 3D printed PNIPAAm hydrogel may be tailored by controlling polymerization kinetics in the PμSL process. In this chapter, some key parameters including polymer resin composition, curing light intensity, and layer thickness of 3D printed PNIPAAm are studied.

4.3.2.1. Effect of polymer resin composition on temperature responsive swelling

The swelling behavior of hydrogels is closely associated with the polymer chain length; for instance, a hydrogel comprised of long polymer chains exhibits a large degree of swelling [140]. Since the polymer network of a PNIPAAm hydrogel is formed by the cross-linkers that connect NIPAAm monomers, the polymer chain length is determined by molar ratio of cross-linker to NIPAAm monomer. In other words, a high ratio of cross-linker to monomer results in more cross-linking sites and therefore a shorter polymer chain

length, leading to a low degree of swelling. The overall concentration of monomer also affects the swelling behavior because it determines the volume of a shrunken PNIPAAm hydrogel at high temperature. To confirm the effect of the molar ratio of cross-linker to monomer on swelling behavior, five different disk shaped samples were printed by PμSL. All of the samples were created with the same monomer concentration, but different molar ratios, ranging from 0.01 to 0.05 (Table 4.1). Since the concentration of NIPAAm is significantly higher than that of cross-linker throughout the five samples, the sum of monomer and cross-linker molecules in all samples were approximately the same.

As shown in Figure 4.7(a), samples with different molar ratios exhibit different swelling behavior at low temperature. It proves that a low molar ratio creates long polymer chains that can stretch further, leading to a high swelling ratio at low temperature (10 °C, blue solid squares in Figure 4.7(a)) as described in the earlier sections. By lowering the molar ratio from 0.05 to 0.01, approximately a 60 % increase in swelling ratio was achieved at 10 °C. On the contrary, the swelling ratio at high temperature (50 °C, red solid circles in Figure 4.7(a)) remained the same around 0.9 across all samples regardless of molar ratio. This is because the concentration of monomer molecules in the resin determines the polymer volume fraction of the cross-linked hydrogel. The swelling of the fully cross-linked samples prepared by a UV oven with a significantly higher exposure dosage (6000 mJ cm^{-2}) showed the similar trend (open squares and circles in Figure 4.7(a)). Swelling differences between printed samples and UV cured fully cross-linked samples at low temperature is attributed to low reactivity of resins with low cross-linker concentration. When a sample was cured in a UV oven, we applied a high energy dose of 6000 mJ cm^{-2} such that all cross-linker molecules in the resin can form cross-links regardless of the

reactivity of the resin. However, for 3D printed samples, an energy dose of 300 mJ cm^{-2} was given to all five printed samples to ensure printing quality and to avoid over-curing (Table 4.3). Therefore, the crosslinking density of printed samples with low cross-linker concentrations is lower than that of UV cured fully cross-linked samples, leading to higher swelling in low temperature. This trend becomes more apparent for the samples with lower cross-linker concentrations. On the other hand, when the cross-linker concentration reaches a ratio of 0.05 to NIPAAm monomer, the reactivity of the resin is high enough that the cross-linking density of the printed sample reaches that of the UV oven cured counterpart. Therefore, we can conclude that swelling of 3D printed PNIPAAm at low temperature can be prescribed by controlling the ratio of cross-linker with respect to NIPAAm in the resin.

To study the effect of the monomer concentration on the swelling behavior, we prepared five samples with different NIPAAm concentrations, 2.6, 4.4, 6.2, 8.0, and 9.7 M, respectively, while keeping the cross-linker to monomer ratio fixed at 0.05. Figure 4.7(b) shows that NIPAAm concentration causes significant change in shrinkage at high temperature, while its influence on low temperature swelling is negligible. By decreasing the NIPAAm concentration from 9.7 to 2.6 M, approximately a 20 % difference in the swelling ratio was achieved at 50 °C. It also showed very good agreement with the results obtained from similar fully cross-linked samples prepared using the UV oven (the open squares and circles). Since the rate of polymerization is strongly dependent on monomer concentration, a different curing time was used for a different NIPAAm concentration (Figure 4.8 and Table 4.3).
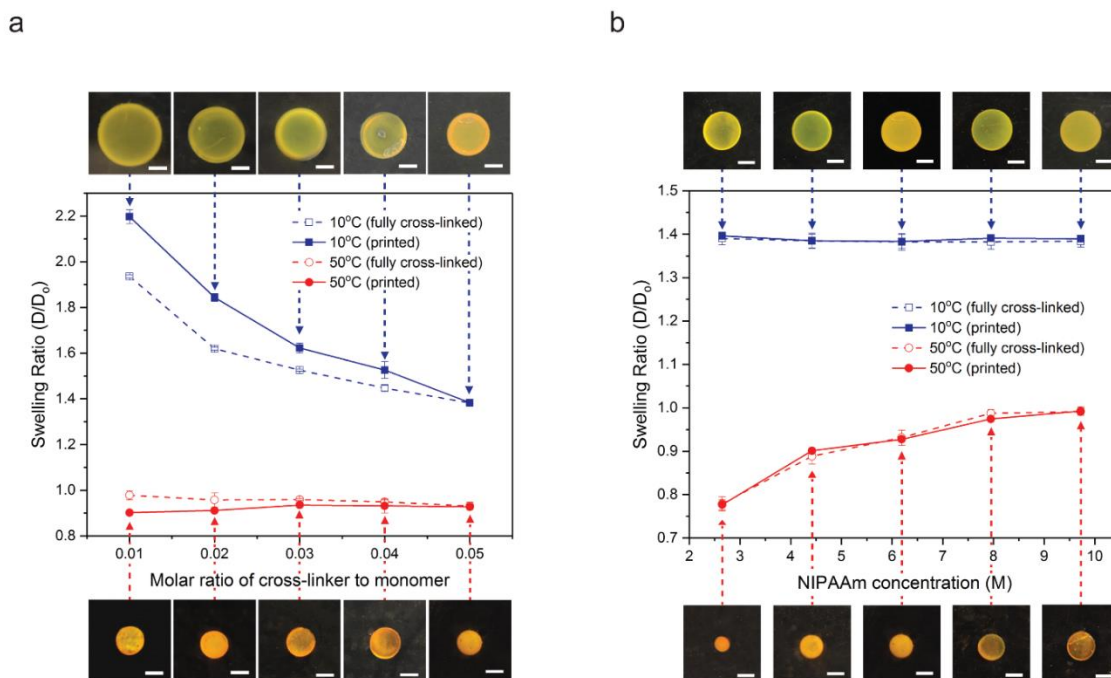
Figure 4.7. Effects of the chemical composition of photo-curable resin on temperature responsive swelling of PNIPAAm. (a) Low temperature swelling of PNIPAAm is determined by the molar ratio of cross-linker to NIPAAm monomer. (b) High temperature shrinkage of PNIPAAm is determined by the NIPAAm concentration. Solid and dashed lines are for the samples fabricated using PµSL and a UV oven, respectively. Blue and red lines are for the swelling ratio at 10 °C and 50 °C, respectively. The photo images show the size of corresponding PNIPAAm disk samples at 10 °C and 50 °C. All scale bars indicate 1 mm.
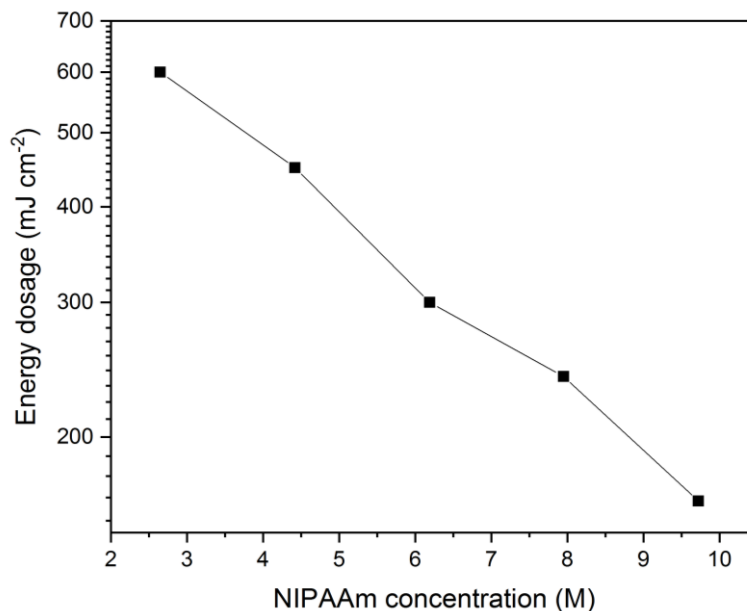
Figure 4.8. Energy dose required to cure a 30 μm thick layer for different NIPAAm concentrations. An excessive energy dose results in unwanted polymerization.

4.3.2.2. Effect of curing light intensity of PμSL on temperature responsive swelling

A light exposure intensity determines the rate of photo-polymerization, which in turn determines the cross-linking density of the hydrogel [106-109, 165]. The cross-linking density is the most important factor that determines the physical properties of the polymer network, including the equilibrium swelling ratio [140]. Since the PμSL system employs a digital image to generate a pattern, the projection light intensity can be easily tuned by controlling the grayscale value of the digital image [168, 169] (Figure 4.9). The grayscale value of a typical 8-bit digital image ranges from 0 to 255, with 0 being black and 255 being white.
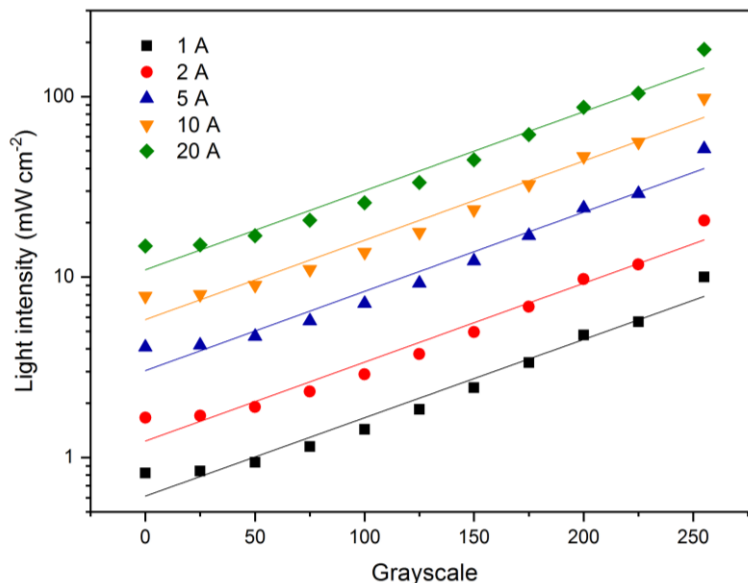
Figure 4.9. The light intensity of the PµSL system for grayscales of a digital image and for different applied currents.

To study the effect of curing light intensity on the degree of swelling, four different disk-shaped samples were fabricated by PµSL using digital images with grayscale values of 100 (4.3 mW cm^{-2}), 150 (7.3 mW cm^{-2}), 200 (14.3 mW cm^{-2}), and 255 (30.0 mW cm^{-2}) (Table 4.3). Figure 4.10(a) shows that the swelling ratio of the 3D printed structures at low temperature (10 °C, blue solid square in Figure 4.10(a)) remains constant at 1.43, whereas the swelling ratio at high temperature (50 °C, red solid circle in Figure 4.10(a)) depends on the grayscale value. PNIPAAm samples printed using a grayscale value of 100 shrank to a swelling ratio of 0.66 at 50 °C while those printed using a white image resulted in a swelling ratio of 0.86 at the same temperature, showing an approximately 23 % difference in the swelling ratio.
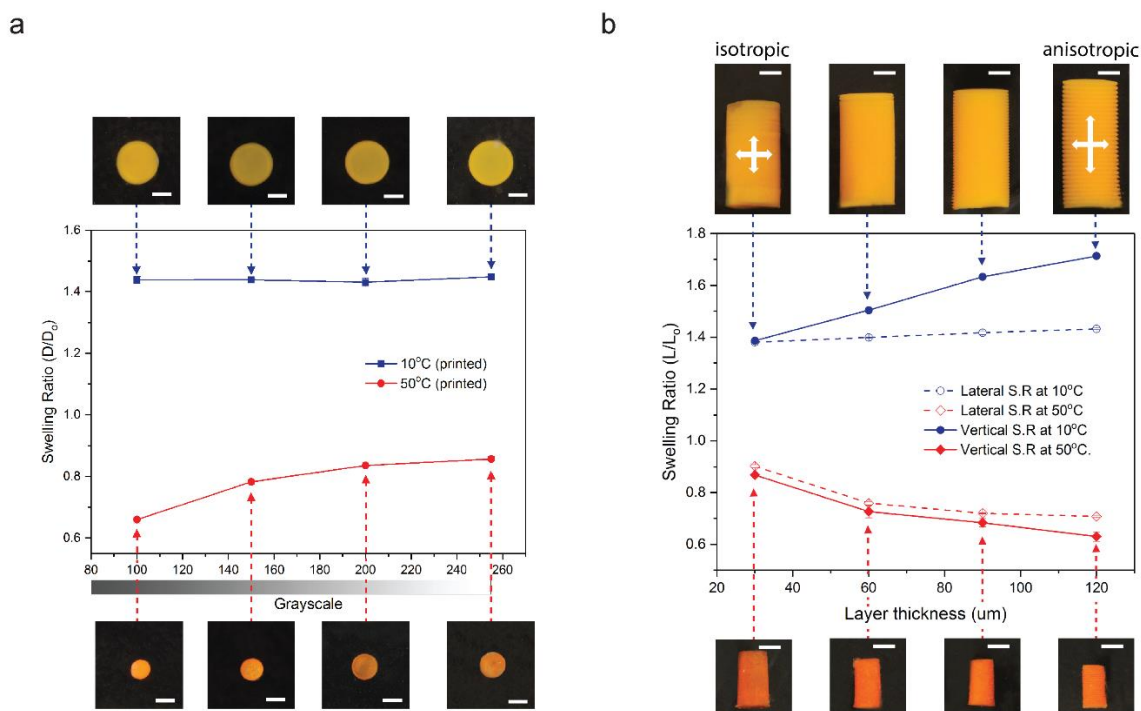
Figure 4.10. Control of temperature dependent swelling of PNIPAAm using PµSL process parameters. (a) As the grayscale level of a projected digital image decreases from white (gray scale of 255) to black (gray scale of 0), the swelling ratio at high temperature of PNIPAAm hydrogel is significantly reduced. Blue and red lines are for the swelling ratio at 10 °C and 50 °C, respectively. (b) Vertical swelling at low temperature increases with layer thickness, while lateral swelling is independent of layer thickness. Shrinkage at high temperature is relatively insensitive to layer thickness. Solid and dashed blue lines are for the swelling ratio at 10 °C in vertical and lateral directions, respectively. Solid and dashed red lines are for the swelling ratio at 50 °C in vertical and lateral directions, respectively. The photo images show the size of corresponding PNIPAAm disks (top view) and cylinders (side view) at 10 °C and 50 °C. All scale bars indicate 1 mm.

This trend is similar to the results from the study of monomer concentration presented in the previous section (Figure 4.7(b)), which implies that the amount of molecules cross-linked into a polymer network decreases with a decreasing light intensity modulated by a grayscale level of the digital image. This is because lower irradiation energy leaves more NIPAAm monomers in the resin uncross-linked, which are later rinsed out from the polymer network by the post-printing rinsing process. Similarly, the low temperature swelling ratio is the same throughout all samples because they were all printed using the same resin (Table 4.1). This result demonstrates that temperature dependent swelling can also be controlled using PµSL even without changing the resin. Furthermore, non-uniform swelling may also be programmed within a layer simply by designing an appropriate distribution of grayscale in the projected digital image.

4.3.2.3. Effect of layer thickness of PNIPAAm on temperature responsive swelling

PµSL, like other 3D printing techniques, builds a 3D object in a layer-by-layer fashion. When each layer is solidified, a UV light is focused on the surface of the resin from which photo-polymerization is initiated and gradually propagates into the resin. Hence, within a layer, a gradient of cross-linking density is created with the upper part being highly cross-linked. Consequently, the swelling behavior throughout the thickness is not uniform because it strongly depends on the cross-linking density as studied on the previous sections (Figure 4.11(a)). As the difference in cross-linking density across the thickness of a layer increases with layer thickness, the bottom portion of a relatively thick layer tends to have a relatively lower cross-linking density and swell further as a consequence (Figure 4.11(b)).
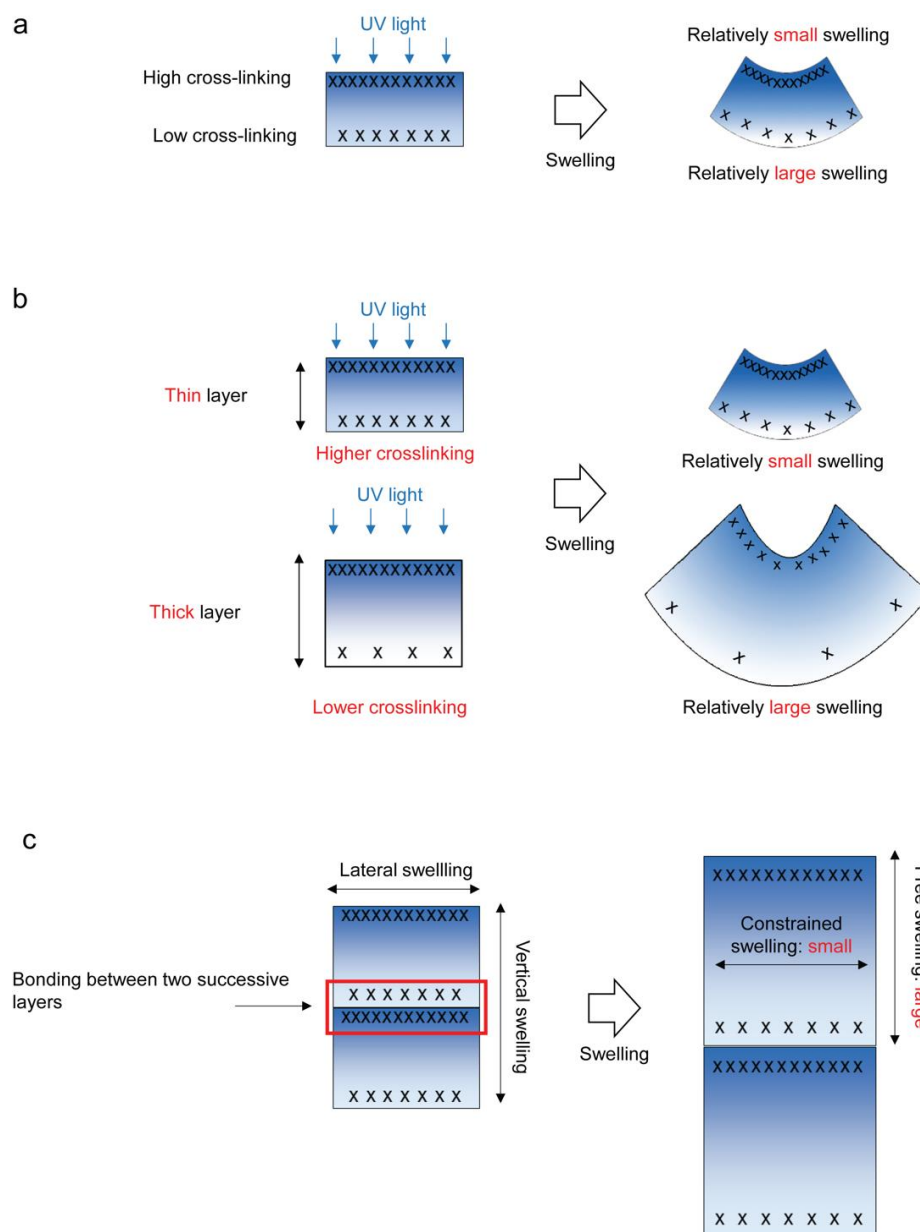
Figure 4.11. The lateral and vertical swelling of 3D printed PNIPAAm layers. (a) A gradient of cross-linking density within a layer and corresponding swelling. (b) Since cross-linking density decreases with layer thickness, larger swelling is expected to occur at the bottom of the layer. (c) Bonding of successive layers constrains lateral swelling while swelling in a vertical direction occurs freely, resulting in overall swelling anisotropy.

When these layers are stacked to create a 3D PNIPAAm structure, the relatively lower cross-linked bottom portion of a layer is bonded to the highly cross-linked top portion of the layer underneath. Due to this physical constraint at the interface, the amount of lateral swelling is therefore dominated by the highly cross-linked upper portion of each layer. On the other hand, the layers can swell freely in the vertical direction without any constraint. (Figure 4.11(c)). As a result, it is possible to create anisotropy in temperature responsive swelling of 3D printed PNIPAAm hydrogel by controlling a layer thickness in the PµSL process.

To study the effect of layer thickness on the lateral and vertical swelling of PNIPAAm, cylindrical samples were printed with the same resin (Table 4.1) but different layer thicknesses (Table 4.3). As shown in Figure 4.10(b), the sample fabricated with a 30 µm layer thickness showed the same swelling ratios in both lateral and vertical directions at high and low temperatures. This implies that cross-linking density within these thin layers is relatively uniform. However, as the layer thickness increases, the amount of vertical swelling at low temperature increases significantly (blue solid circle in Figure 4.10(b)) while lateral swelling remains almost identical regardless of layer thickness (blue open circle in Figure 4.10(b)). When the PNIPAAm hydrogel shrinks at high temperature, the deformation in both lateral (red open diamond in Figure 4.10(b)) and vertical (red solid diamond in Figure 4.10(b)) directions were similar regardless of layer thickness. This result demonstrates that PµSL provides a unique capability to create anisotropy in thermo-responsive swelling of PNIPAAm hydrogel.

4.3.2.4. Effect of ionic co-monomer on temperature responsive swelling

The transition temperature of 3D printed PNIPAAm structures is the LCST of NIPAAm, 32-35 °C. However, it can be shifted by adding positively charged ionic co-monomer, Methacrylamidopropyltrimethyl-ammonium Chloride (MAPTAC), to the polymer resin. The positively charged MAPTAC integrated in the cross-linked network increases hydrophilicity of a polymer chain because of the growing ratio of cationic site [170, 171]. As a result, the transition temperature shifts up from around 32 °C to a higher temperature. To confirm the effect of MAPTAC, three different PNIPAAm disks were printed with different concentrations of MAPTAC (Tables 4.1 and 4.3). As shown in Figure 4.12, the disk without MAPTAC dramatically changes in size between 20 and 30 °C (orange box and line in Figure 4.12), whereas adding 0.2 and 0.4 M of MAPTAC resulted in shift in transition temperature to 30 – 40 °C (green box and line in Figure 4.12) and 40 – 50 °C (blue box and line in Figure 4.12), respectively.

The temperature at which more than 80 % of the entire swelling deformation was achieved shifts from 35 °C for original PNIPAAm to 50 °C and 65 °C for 0.2 M and 0.4 M of MAPTAC, respectively (Figure 4.13). Furthermore, adding MAPTAC to PNIPAAm allows for broadening and linearizing the swelling transition, which could potentially be utilized in various sensing applications.
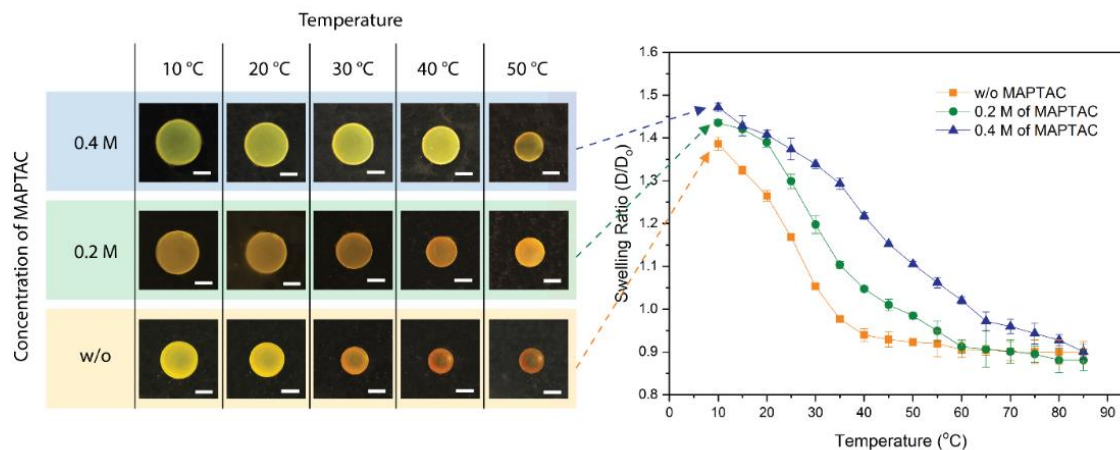
Figure 4.12. The swelling transition temperature of PNIPAAm increases by adding ionic co-monomer. Green and blue lines show temperature responsive swelling of PNIPAAm with 0.2 M and 0.4 M of MAPTAC, respectively. The swelling ratio of the standard PNIPAAm without MAPTAC (orange line) was measured as a control. The photo images show the size of corresponding disk samples at different temperatures. All scale bars indicate 1 mm.
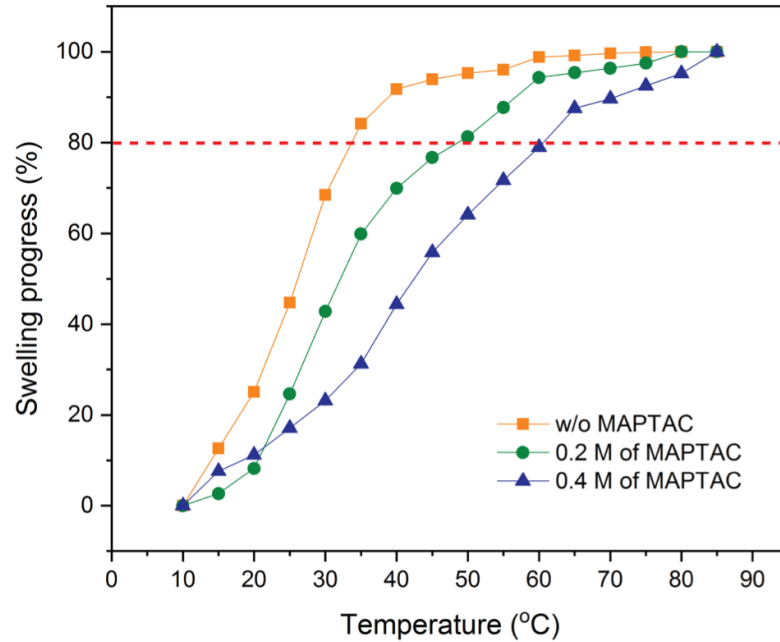
Figure 4.13. Swelling progress as a function of temperature for various concentrations of MAPTAC. More than 80 % of the entire swelling ratio change was achieved at 35 °C without MAPTAC, at 50 °C with 0.2 M of MAPTAC, and at 65 °C with 0.4 M of MAPTAC.

4.3.3. 3D printed PNIPAAm micro-structures

Based on the findings presented above, we 3D printed PNIPAAm structures using a variety of different process parameters. Figure 4.14 shows a gripper consisting of four beams fabricated using two different levels of grayscale. Due to the different levels of light intensity (4.3 mW cm^{-2} for gray (100) and 30 mW cm^{-2} for white (255)), a virtual bilayer beam having two different swelling characteristics was created. Different swelling ratios in different regions of the cross-section generated a strain mismatch between the two regions, causing a bending deformation of the beam as the temperature is cycled. At temperatures below the transition temperature, all beams are straight since both white and

gray regions have a similar swelling ratio. As temperature increases, the gray regions facing the center start to shrink more than white regions, causing the beams to bend inward to generate a gripping motion. When the temperature lowers, the beams become straight again.

Also, a dumbbell-shaped structure in Figure 4.14(b) was fabricated using two different resins having different transition temperatures. The left half was made of pure PNIPAAm and the right half was made using a PNIPAAm resin with 0.4 M of MAPTAC. At low temperature (10 °C), both sides are fully swollen, so the dumbbell is symmetric. As the temperature increases, the left half begins to shrink while the right half remains in its fully swollen state, posing an asymmetric shape at a temperature near 35 °C. When temperature further increases beyond the transition temperature of the right half, shrinking starts to occur in the right half as well, and the dumbbell eventually becomes symmetric again, but in a smaller shrunken dimension. As demonstrated here, PμSL provides a unique fabrication capability to easily program complex temperature responsive deformation in 3D PNIPAAm micro-structures.
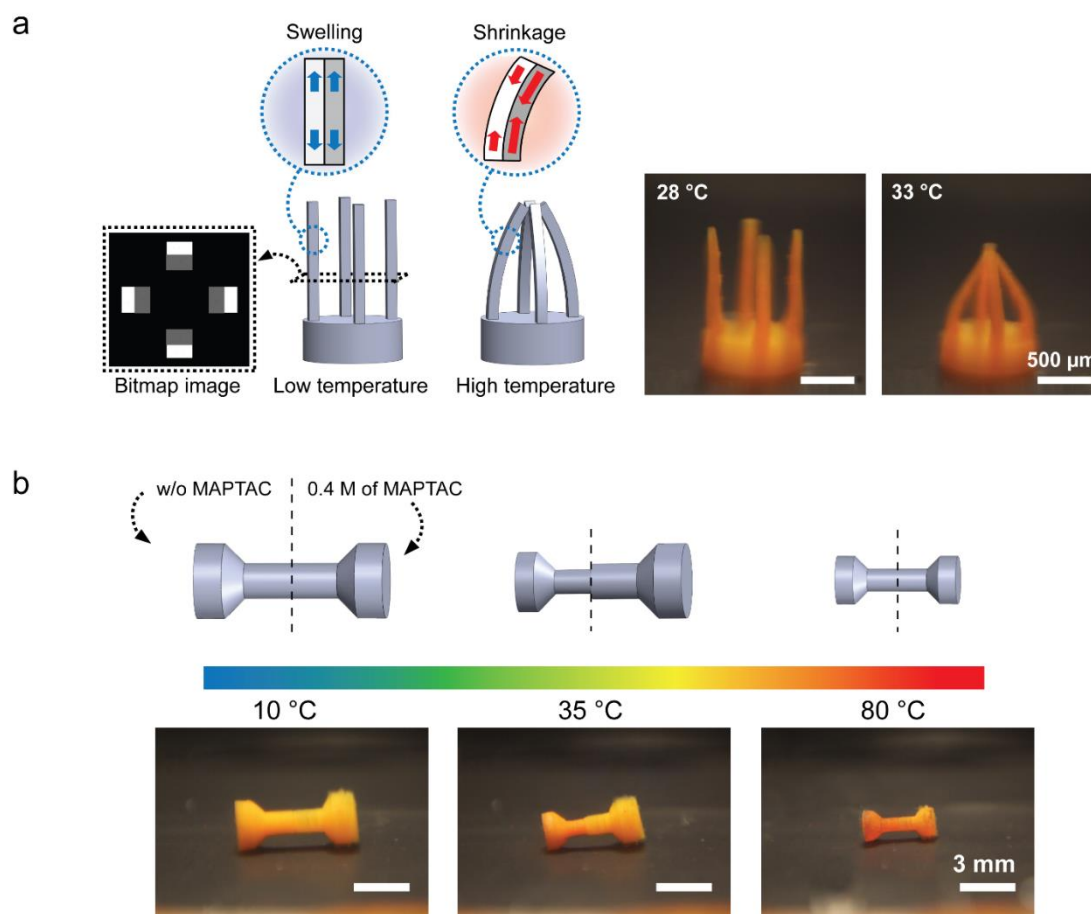
Figure 4.14. 3D printed PNIPAAm micro-structures and their programmed temperature dependent deformation. (a) A gripper consisting of four beams was fabricated using two different grayscale levels. The difference in the swelling ratio between the two regions caused the beams to bend towards the center at high temperature (scale bar: 500 μm). (b) A dumbbell-shaped structure was printed with ionic monomer, MAPTAC. The left half is pure PNIPAAm while the right half contains 0.4 M of MAPTAC. When temperature increases, the left half with lower transition temperature begins to shrink first, and the right half shrinks later at higher temperature (scale bar: 3 mm).

4.4. Conclusion

We presented the 3D fabrication of PNIPAAm micro-structures using high resolution PµSL. The effects of various material and process parameters involved in the PµSL process on the thermally responsive swelling of 3D printed PNIPAAm were investigated. We found that PNIPAAm swelling at low temperature and shrinking at high temperature can be independently controlled. The molar ratio of cross-linker to monomer determines the low temperature swelling of PNIPAAm, while high temperature shrinking of PNIPAAm is primarily determined by the monomer concentration. Furthermore, we demonstrated that grayscale of digital images can be utilized to control curing light intensity, which mainly affects the high temperature shrinkage of 3D printed PNIPAAm. This indicates that temperature dependent swelling behavior of PNIPAAm can be spatially encoded and distributed within a layer without the need for time- and material-consuming resin exchange. We have also shown that 3D printed PNIPAAm swelling in the lateral and vertical directions is dependent on the layer thickness, through which anisotropic thermo-responsive swelling can be achieved by design. In addition, control of the swelling transition temperature of PNIPAAm was demonstrated by incorporating a hydrophilic ionic monomer. The transition temperature was increased with increasing ionic monomer concentration. Overall, we believe that the presented method of using PµSL to three-dimensionally fabricate PNIPAAm micro-structures, along with the understanding of the temperature responsive swelling characteristics of PNIPAAm, will significantly extend the potential of smart materials for various applications, such as soft robots, microfluidic devices, and drug delivery vehicles.

Chapter 5

Multi-Material 4D Printing of

Bio-Inspired Adaptive Camouflage Skin

5. Multi-Material 4D Printing of Bio-Inspired Adaptive Camouflage Skin

5.1. Introduction

Soft materials, including polymers, colloids, granular materials, liquid crystals, and a number of biological materials, are materials that can be easily deformed or structurally altered by thermal or mechanical stresses and fluctuations. The main physical behaviors of these materials occur at an energy scale comparable to room temperature thermal energy, which can be obtained relatively easily. Soft materials have been receiving a great deal of attention in a wide range of engineering fields, such as tissue engineering [2, 172], drug delivery [4], biomedical devices [173, 174], microfluidics [175, 176], optics [177-179], stretchable electronics [180-183], and soft robotics [108, 110, 111, 184, 185], because of their unique characteristics, such as, multi-functionality, adaptability, flexibility, lightweight, and biocompatibility.

In nature, living creatures mostly made of soft materials are perpetual sources of inspiration for engineering functional materials. It is fascinating to observe how certain living creatures perform seemingly impossible tasks; for instance, binding of gecko's feet to various surfaces, manipulating of octopus's arm with almost unlimited degree of freedom, color generating of butterfly's wing without pigments, etc. Camouflage animals, which reversibly change their structural colors or textures in response to their surrounding environment, have been studied to understand their camouflage mechanisms. Camouflage animals can be classified into two groups according to their mechanisms: non-changeable skin coloration and changeable skin coloration. The former group of animals, such as owls

and leaf bugs, has non-changeable colors and textures that resemble to their surrounding environments. It makes it possible for them to successfully hide their bodies from their enemies. The latter group of animals exhibits more interesting and complex camouflage mechanisms, showing active color changes. The examples include seasonal molting of snowshoe hares, and color changes of chameleons and octopuses.

Within the second group, we are particularly interested in octopuses, since these marine molluscs possess soft material bodies, diverse behaviors, elaborate skin patterning capabilities and a sophisticated visual system that controls body patterning for communication and camouflage. It is well-known that the camouflage mechanism of cephalopods, including octopuses, cuttlefishes, and squids, consists of contraction and expansion of pigments-containing chromatophores in the skin [186-188] (Figure 5.1).
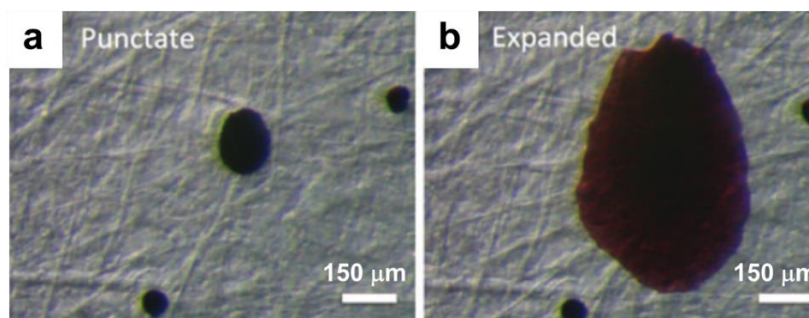
Figure 5.1. A single retracted (a) and expanded (b) chromatophore. Images are from [187].

The chromatophores consist of a central cytoelastic sac which contains pigment granules. This sac is surrounded by a series of radial muscles (Figure 5.2(a)). A typical size of the central sac is approximately 150 μm in diameter when it is retracted, and is approximately 450 μm (about three times) when it is expanded. Contraction of the radial

muscles results in planar expansion of the central sac. It is the expansion of the network of pigmented sac, relative to the unpigmented surrounding tissue, which generates the optical effect. The skin of cephalopods is composed of three different sacs with different pigment colors. These sacs contribute to their rapid and various color-changing ability (Figure 5.2(b)). By contracting and releasing the radial muscles, the corresponding sacs can expand and shrink their areas, reversibly generating a variety of patterns with multiple colors within a few seconds [189, 190]. Therefore, implementing these outstanding features of the cephalopods on soft devices will enable the development of various applications, such as flexible display and electronics, bio-photonic devices, and dynamic camouflage interfaces.
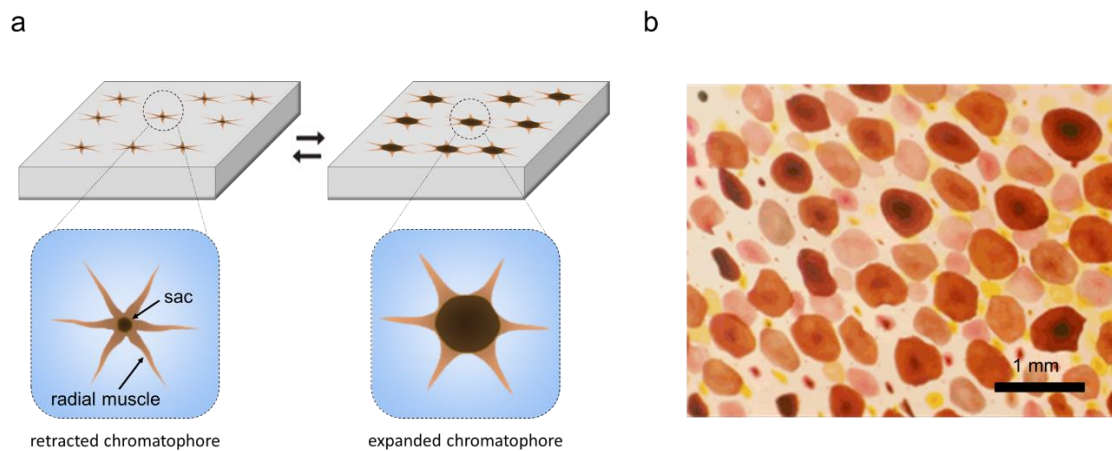
Figure 5.2. (a) Schematic illustration of chromatophore and its composition. (b) Skin of cephalopods with three different color chromatophores (black, brown, and yellow).

Recently, color-changing devices inspired by cephalopods have been demonstrated using electrokinetic technology [191], on-demand fluorescent patterning with electro-mechano-chemically responsive elastomers [192], and actuating of dielectric elastomers

[188]. However, these devices required a high voltage to activate the system and produced the color change using a method different from the actual color change mechanism (muscle contraction) of cephalopods. In order to realize the actual mechanism, development of new materials and manufacturing technology that can fabricate a complex device composed of multiple materials are essential.

In this chapter, we report a cephalopod-inspired adaptive camouflage skin that shows the dynamic color modulation using the actual color change mechanism with light irradiation. The skin employs rectangular artificial chromatophores comprised of three components; photo-active muscles, a stretchable sac, and a rigid frame (Figure 5.3). Each component plays an important role in implementing the color change mechanism. First, photo-active muscle made of a photo-active hydrogel exhibits large volume shrinkage under light irradiation, which pulls out the stretchable sac. The photo-active hydrogel was made by adding poly-dopamine nanoparticles (PDA-NPs) to thermo-responsive hydrogel (PNIPAAm) that exhibits swelling at low temperatures and shrinkage at high temperatures (see details in Chapter 4). PDA-NP, one of the well-known photo-thermal agent, generates heat energy via photo-thermal effect associated with electromagnetic radiation [193]. The generated thermal energy from PDA-NPs is transferred to a thermo-responsive hydrogel. The temperature of the hydrogel is then raised to trigger shrinkage of a thermo-responsive hydrogel. Second, the stretchable sac creates an optical effect using its large area changes generated by photo-active muscles. Lastly, a rigid rectangular frame anchors one end of the photo-active hydrogels, allowing the sac to stretch effectively.

To successfully demonstrate the artificial chromatophore, there are some requirements for each component. Photo-active hydrogel for photo-active muscles should

generate enough heat energy to shrink the hydrogel under a given light energy, and the shrinkage force generated during the contraction of the hydrogel should be able to stretch the sac up to three times. The stretchable material for the sac should be able to stretch up to three times without fracture. Finally, the material for the rigid frame should exhibit strong bonding with the photo-active hydrogel and less deformation when the hydrogel shrinks. According to these requirements, we characterized the material for each component and successfully fabricated artificial chromatophores using these materials. As a manufacturing tool for the artificial chromatophore, we used a digital light processing (DLP)-based multi-material additive manufacturing technique, multi-material projection micro-stereolithography (MM-PμSL).
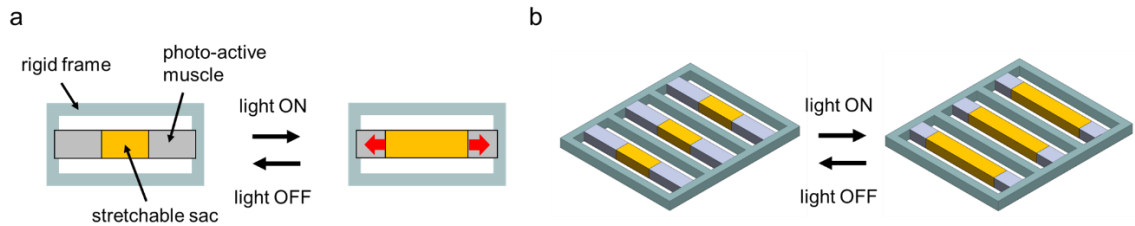
Figure 5.3. Schematic illustrations of rectangular artificial chromatophore unit cell (a) and cephalopod-inspired adaptive camouflage skin having multiple chromatophore cells (b)

5.2. Materials and Methods

5.2.1. Materials

Poly(ethylene glycol) diacrylate, Mn~250 (PEGDA 250), Poly(ethylene glycol) diacrylate, Mn~700 (PEGDA 700), Acrylic acid (AA), Phenylbis(2,4,6-trimethylbenzoyl) phosphine oxide (photo-initiator, PI), Iron(III) nitrate nonahydrate, Dopamine hydrochloride, and Ammonium hydroxide solution were purchased from Sigma-Aldrich. N-Isopropylacrylamide (NIPAAm) was purchased from Fisher Scientific. All materials were used as received. Table 5.1 provides the chemical components of the solutions used in each study and their concentrations.

5.2.2. Synthesis of PDA-NPs

PDA-NPs were synthesized according to the procedure reported in the literature (oxidation and self-polymerization dispersion polymerization procedure) [193]. 2 mL of ammonium hydroxide solution (NH_4OH) was mixed with 80 mL of ethanol and 180 mL of deionized water (DI water) and stirred at room temperature for 10 minutes. 1 g of dopamine hydrochloride was dissolved in 20 mL of deionized water and then added into the above mixture solution. The mixture was stirred in the dark at room temperature for 30 hours to allow dopamine polymerization. The PDA-NPs were then dried at 60 °C.

Table 5.1. Material composition of photo-curable precursor solutions

Study	Material composition					
	Monomer (M)	Cross-linker (PEGDA700) (M)	PI (mM)	PDA (g/L)	Fe^{3+} (mM)	Solvent
Photo-active hydrogel (Sec.5.3.2)	NIPAAm (2.6)	0.36	47.8	- 10 20 30	- - - -	Ethanol
Cross-linker concentration study for AA hydrogel (Sec.5.3.3.1)	AA (3.0)	0.02 0.05 0.10 0.20 0.40 0.80	47.8	- - - - - -	15	Ethanol
Fe^{3+} concentration study for AA hydrogel (Sec.5.3.3.2)	AA (3.0)	0.02	47.8	- - - - - - -	0 5 10 15 20 25 30	Ethanol
Mechanical properties for 3 materials (Sec.5.3.4)	PEGDA250 NIPAAm (2.6) AA (3.0)	- 0.36 0.02	47.8	- 30 -	- - 15	- Ethanol Ethanol

5.2.3. Absorbance measurement of PDA-NPs solution

Five solutions were prepared with predetermined PDA-NPs concentrations (0.0125, 0.025, 0.05, 0.1, and 0.2 g/L). The PDA-NPs were dispersed in DI water and stirred in the dark at room temperature overnight. Then, absorption spectra (400 to 900 nm) of the PDA-NPs solutions were measured at room temperature with a UV-Vis spectrometer (FLAME-S, Ocean Optics) and a halogen lamp (HL-2000-HP-FHSA, Ocean Optics) as a light source (Figure 5.4). The cuvette (CVD-UV1S-SAM, Ocean Optics) used in this chapter has a 1

cm path length. Average of absorbance was calculated to study the light penetration depth and photo-thermal efficiency (Figure 5.5).
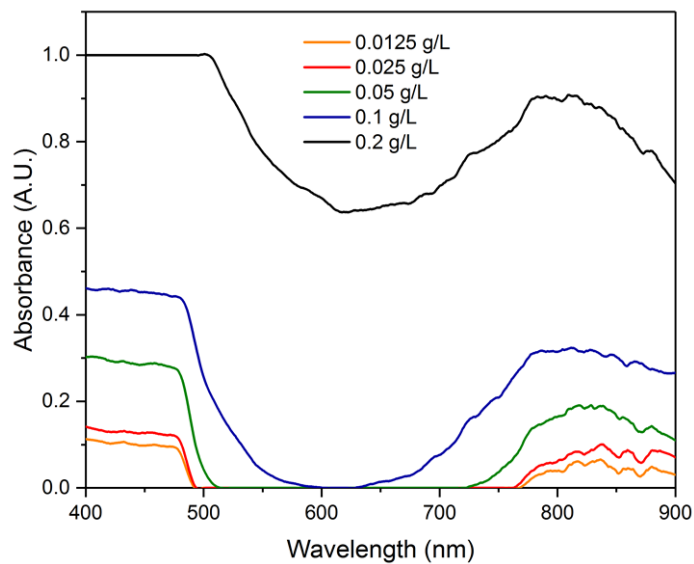
Figure 5.4. Absorbance spectrum of PDA-NPs solutions
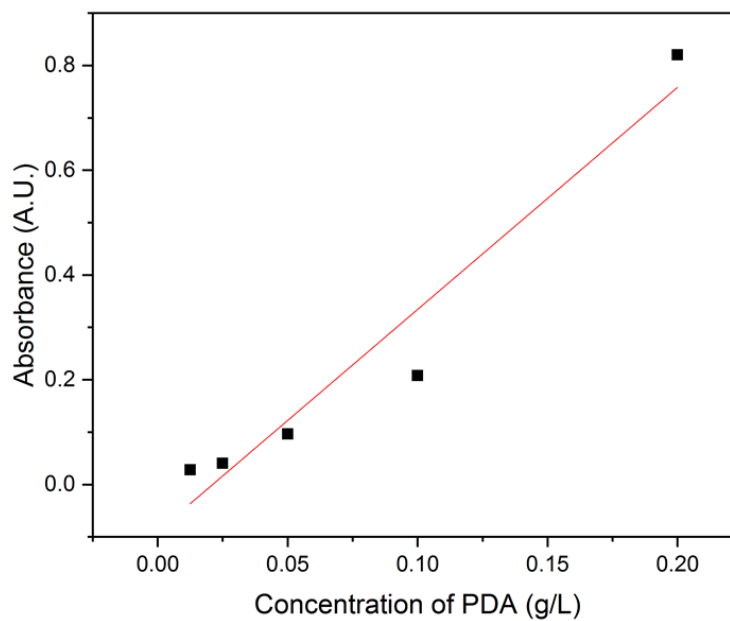
Figure 5.5. Average absorbance of PDA-NPs solutions

5.2.4. Light penetration depth of PDA solutions

PDA-NPs generate thermal energy via photo-thermal effect associated with electromagnetic radiation. Therefore, the light penetration depth of PDA solution is closely related to the amount of heat energy generated from PDA solution. The light penetration depth can be calculated based on Beer-Lambert law.

$$A = log_{10}\left(\frac{I_0}{I}\right) = \varepsilon c l \qquad (5.1)$$

where A is the absorbance of the solution, I_0 is the incident intensity of the light, I is the transmitted intensity of the light, ε is the molar absorptivity of PDA, c is the concentration of PDA, and l is the length of the light path. Based on the absorbance results (Figure 5.5), the molar absorptivity (ε = 4.24 L/g cm) of PDA can be calculated. With the molar absorptivity of PDA, the light penetration depth according to the PDA concentration can be predicted based on Beer-Lambert law (Eq. 5.1). If we set the threshold light absorbance to be 90% (A=1), the light penetration depth for 10, 20, and 30 g/L are 236, 118, and 79 μm, respectively (Figure 5.6).
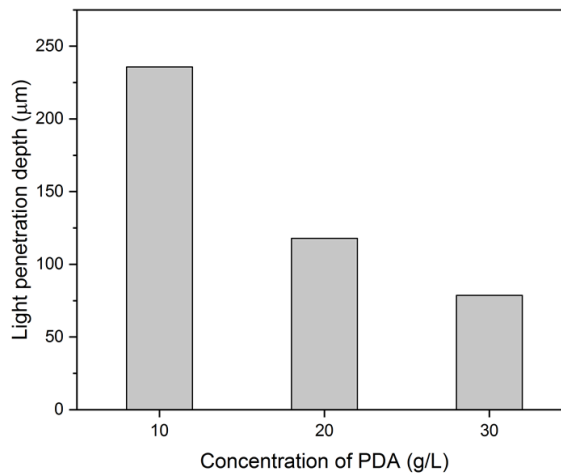
Figure 5.6. Calculated light penetration depth of PDA-NPs solutions

5.2.5. Photo-thermal effect of PDA-NPs solution

Seven solutions were prepared with predetermined PDA-NPs concentrations (0, 0.31, 0.62, 1.25, 10, 20, and 30 g/L). The PDA-NPs were dispersed in DI water and stirred in the dark at room temperature overnight. 34 μL of each solution was added into the 96-well microplate (D: 0.654 cm), resulting in the height of the solution being 1 mm. A commercial beam projector (PJD6531w/DLP, ViewSonic) was used as a light source. The light intensity of the projector is 0.77 W/cm^2 when a white image was projected. Temperature of the solutions was monitored using a thermocouple, and recorded with LabVIEW.

5.2.6. Calculation of the photo-thermal conversion efficiency

The photo-thermal conversion efficiency of PDA-NPs was determined according to the method described in the literature [193]. Briefly, the photo-thermal conversion efficiency was calculated based on the total energy balance of the system.

$$\sum_i m_i C_{p,i} \frac{dT}{dt} = Q_{NPs} + Q_s - Q_{loss} \qquad (5.2)$$

Here, m is the mass of solvent (water), C_p is the heat capacity of solvent (4.184 J/gK, water), T is the solution temperature. Q_{NPs}, Q_s, and Q_{loss} are the photo-thermal energy generated by PDA-NPs, the heat associated with the light absorbance of the solvent, and the heat energy lost to the surroundings.

$$Q_{NPs} = I(1 - 10^{-A_\lambda})\eta \qquad (5.3)$$

Here, I is the projection light energy, A_λ is the absorbance of PDA, and η is the photo-thermal conversion efficiency from the absorbed light energy to heat energy.

$$Q_s = m_{water} C_{p,water} \Delta T \qquad (5.4)$$

In this chapter, Q_s measured with deionized water without PDA-NPs is 5.38 J.

$$Q_{loss} = hA\Delta T \qquad (5.5)$$

Here, h is the heat transfer coefficient, A is the surface area of the container, and ΔT is the temperature change, which is defined as $T_{solution}$ - $T_{surroundings}$.

At the maximum steady-state temperature, the heat generated is equal to the heat lost to the surroundings.

$$Q_{NPs} + Q_s = Q_{loss} = hA\Delta T_{max} \qquad (5.6)$$

According to the Eq. 5.3 and Eq. 5.6, the photo-thermal conversion efficiency (η) can be determined:

$$\eta = \frac{hA\Delta T_{max} - Q_s}{I(1 - 10^{-A_\lambda})} \qquad (5.7)$$

In Eq. 5.7, ΔT_{max}, Q_s, I, and A_λ can be obtained experimentally, but hA is unknown values for solving the equation. To get the hA values, we introduced θ, which is defined as the ratio between ΔT and ΔT_{max}.

$$\theta = \frac{\Delta T}{\Delta T_{max}} \qquad (5.8)$$

According to the Eq. 5.2 and Eq. 5.8, the total energy balance of the system can be rearranged:

$$\frac{d\theta}{dt} = \frac{hA}{\sum_i m_i C_{p,i}} \left[\frac{Q_{NPs} + Q_s}{hA\Delta T_{max}} - \theta \right] \qquad (5.9)$$

When the projection light is off, Q_{NPs} and Q_s are zero.

$$dt = -\frac{\sum_i m_i C_{p,i}}{hA} \frac{d\theta}{\theta}$$

(5.10)

By integrating Eq. 5.10, we can obtain the relationship between t and $ln\theta$.

$$t = -\frac{\sum_i m_i C_{p,i}}{hA} ln\theta$$

(5.11)

The *hA* value can be determined by plotting the cooling time (after shutting off the light) as a function of $-ln\theta$ (Figure 5.7(b)). The photo-thermal conversion efficiency of PDA-NPs can be calculated by substituting *hA* value into Eq. 5.7.

Based on the above analysis, the photo-thermal efficiency of the PDA-NP solution of 30 g/L was 25%.
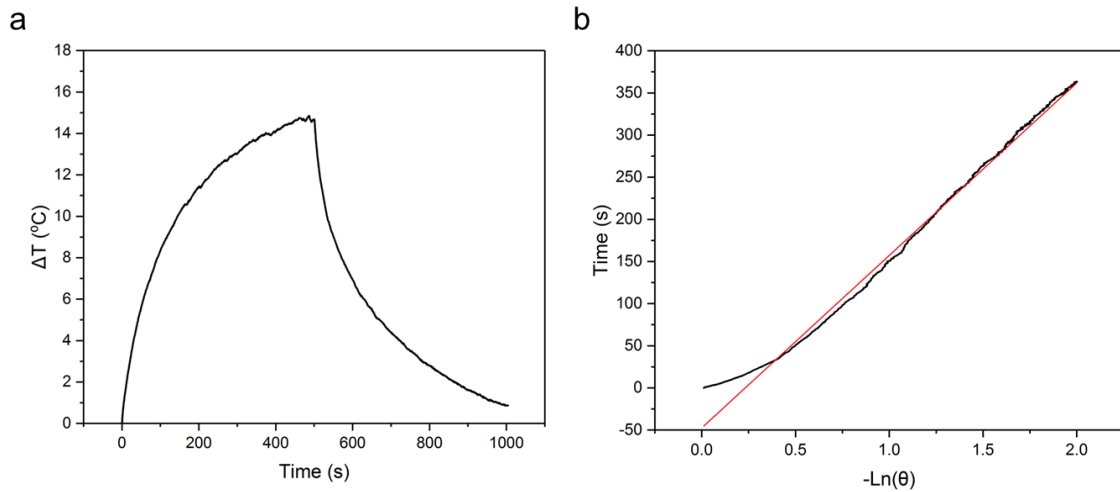
Figure 5.7. Photo-thermal efficiency calculation of PDA-NP solution (30 g/L). (a) The photo-thermal response of the PDA-NP solution (30 g/L) for 500 s with a projection light (0.77 W/cm^2) and then the projection was shut off. (b) Linear time data versus $-ln(\theta)$ obtained from the cooling period of Figure 5.7(a).

5.2.7. Fabrication of photo-active hydrogel with PDA-NPs

To prepare the photo-curable precursor solution for photo-active hydrogel, 2.6 M of NIPAAm was dissolved in ethanol with 0.36 M of cross-linker (PEGDA 700), and 47.8 mM of PI. Then, PDA-NPs was added to the precursor solution as a photo-thermal material. The solution was mixed in the dark at room temperature overnight. The prepared solution was filled into a film-shaped glass mold which has 300 μm thickness, and cured with light energy (1320 mJ cm^{-2}) using a UV oven (CL-1000L, UVP, 365 nm), yielding a fully cross-linked hydrogel film. Disk samples were made from the film sample using a punch tool with a diameter of 4.8 mm. The rectangular samples for mechanical tests were created with a glass mold which has 150 μm thickness. All samples were rinsed in DI water at room temperature overnight.

5.2.8. Swelling ratio study for hydrogels

The swelling ratio of hydrogel samples was obtained by optically measuring the diameter of the disk sample. The samples were put into a temperature-controlled chamber filled with DI water. The chamber has a transparent glass window through which temperature dependent deformation of samples were observed and measured. The temperature of water in the chamber was controlled within a range from 10 °C to 60 °C (temperature change rate: 0.4 °C/min). The swelling ratio of the sample was measured every 5 °C. When the water reached the target temperature, the temperature increase was temporarily stopped for one hour, allowing the sample to reach equilibrium swelling. Then, a photo image of the

sample was taken using a digital camera, and sample dimension was measured from the image using image analysis software, Image J.

5.2.9. Photo-thermal effect of photo-active hydrogel

A commercial beam projector (PJD6531w/DLP, ViewSonic) was used as a light source. The light intensity of the projector is 0.77 W/cm^2 when a white image was projected. Temperature of the hydrogels was monitored using a thermal camera (TIM 640, Microepsilon), and the swelling ratio of hydrogels was calculated by optically measuring the diameter of the disk sample.

5.2.10. Shrinkage force measurement for photo-active hydrogel

To measure the shrinkage force of photo-active hydrogel at increasing temperatures, rectangular specimens (30 mm x 5 mm x 150 μm) of PNIPAAm including PDA-NPs (concentration: 30 g/L) was prepared using UV oven with a glass mold. Then, dynamic mechanical analysis (DMA) was conducted on a dynamic mechanical analyzer (DMA 850, TA Instruments) using a submersion tension clamp. All samples were tested with isostrain mode and the temperature increased from room temperature to 50 ^{o}C at a ramp rate of 1 ^{o}C min^{-1}.

5.2.11. Fabrication of stretchable acrylic acid (AA) hydrogel with Fe^{3+} ions

To prepare the photo-curable precursor solution for stretchable AA hydrogel, 3 M of AA was mixed with 47.8 mM of PI. Then, cross-linker (PEGDA 700) and iron (III) nitrate nonahydrate were added to above solution. The solution was mixed in the dark at room temperature overnight. The prepared solution was filled into a film-shaped glass mold which has 1 mm thickness, and cured with light energy (1320 mJ cm^{-2}) using a UV oven (CL-1000L, UVP, 365 nm), yielding a fully cross-linked hydrogel film. Disk samples for swelling ratio study were made from the film sample using a punch tool with a diameter of 4.8 mm. All samples were rinsed in DI water at room temperature overnight.

5.2.12. Mechanical properties of three materials

To measure the mechanical properties of three materials (PNIPAAm with PDA, AA with Fe^{3+} ions, and PEGDA 250) rectangular specimens (25 mm x 4 mm x 1 mm (or 300 μm)) were prepared using UV oven (light energy: 1320 mJ cm^{-2}) with glass mold. Then, the samples were rinsed in DI water at room temperature overnight. Mechanical properties of the materials were measured on a dynamic mechanical analyzer (DMA 850, TA Instruments) using two clamps, film tension clamp for AA samples and submersion tension clamp for PNIPAAm and PEGDA samples. All samples were tested at room temperature with strain rate of 0.33 %/s and preload force of 0.001 N.

5.2.13. Bonding strength between materials

To measure the bonding strength between two different materials, multi-material rectangular specimens (30 mm x 4 mm x 300 μm) were prepared using UV oven with glass mold. For PNIPAAm/PEGDA samples, PNIPAAm hydrogel was fabricated first in the glass mold (15 mm x 4 mm x 300 μm) using UV oven (light energy: 1320 mJ cm^{-2}). Then, PEGDA solution was injected into the space next to the fabricated PNIPAAm hydrogel. The PEGDA solution was then cured using UV oven (light energy: 1320 mJ cm^{-2}). The samples were rinsed in DI water at room temperature overnight. For AA/PNIPAAm samples, AA hydrogel was cured first in the glass mold, followed by the PNIPAAm hydrogel. Bonding strength between materials was measured on a dynamic mechanical analyzer (DMA 850, TA Instruments) using a film tension clamp. All samples were tested at room temperature with strain rate of 0.33 %/s and preload force of 0.001 N.

5.2.14. Multi-material projection micro-stereolithograpy (MM-PμSL)

A MM-PμSL system was built with the following major components: a UV LED (405 nm, Innovations in Optics), a digital micro-mirror device (DMD) (extracted from P1 projector, ASUS, Taipei, Taiwan), a projection lens (magnification of 0.2X, GCA Tropel, Fairport, NY), linear stages (Newport Corporation, Irvine, CA), a vacuum pump (Parker, Cleveland, OH), and 2-way pinch valves (Reet Corporation, Berlin, CT). All components of the system are controlled by a custom-written LabVIEW (National Instruments) script.

5.2.15. Curing depth study for photo-curable precursor solutions

To create a 3D structure using MM-PµSL, we studied the light energy dosage required to cure a certain depth of photo-curable precursor solutions in MM-PµSL. The test structure consisted of two side supports and five suspended bridges between the supports (Figure 5.8). Sufficient vertical distance was given between the bridges to prevent them from overlapping with each other when they grow in vertical direction. Since each successive bridge was created with an increased energy dosage, each bridge grew to an increasingly thicker depth. The photo images of the bridges were obtained using a microscope, and the curing depth of the bridges was measured using Image J. On the basis of curing depth study, a specific value of energy dosage required to create a layer with certain thickness (100 µm in this study) can be determined. MM-PµSL process parameters used in this study are shown in Table 5.2.
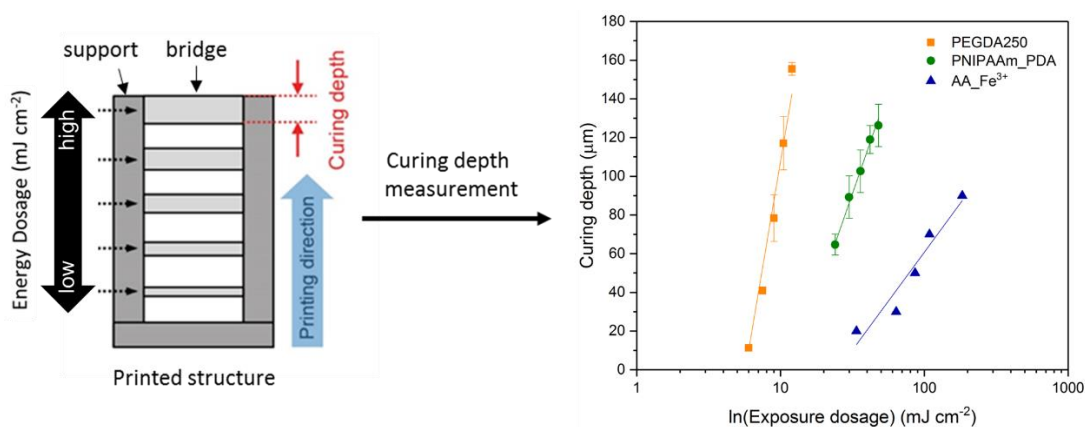
Figure 5.8. Curing depth study for three different materials. Schematic illustration of test structure with five bridges. The curing depth as a function of light energy dosage was measured using a microscope.

Table 5.2. MM-PµSL process parameters for 3D printing of artificial chromatophore

Component (Material)	Light intensity (mW cm^{-2})	Curing time (sec)	Layer thickness (µm)
Rigid frame (PEGDA 250)	29.5	2	100
Photo-active muscle (PNIPAAm/PDA 3%)	29.5	11	100
Stretchable sac (AA/Fe^{3+})	29.5	20	100

5.2.16. Post-printing rinsing process

After 3D printing, the samples were rinsed and stored in DI water at room temperature overnight in order to exchange the remaining uncross-linked polymers in the network with DI water. Typical volume of the DI water used in rinsing is 50 ml for the sample. With an abundant amount of rinsing water, remaining uncross-linked polymers in the printed structure is effectively diluted and replaced with water.

5.3. Results and Discussion

5.3.1. Photo-thermal effect of PDA-NPs

PDA-NPs have been receiving a great deal of attention as a photo-thermal agent with high photo-thermal conversion efficiency and good biological functions [193]. In addition, PDA, containing both catechol and amine groups, has a molecular structure similar to that of mussel-adhesive proteins, and exhibits high adhesion to a wide range of substrates through covalent bonds and noncovalent interactions with substrates [194]. Thus, incorporating PDA-NPs into hydrogel systems can lead to the development of numerous biomedical devices and bio-nanotechnologies that have not been explored and realized with existing technologies to date.

We synthesized PDA-NPs via oxidation and self-polymerization dispersion polymerization procedure (see details in sec. 5.2.2) [193]. To study whether PDA-NPs can effectively convert light energy into thermal energy, various concentrations of PDA-NP solutions were prepared with deionized water (DI water), and their temperature changes were observed when light was illuminated. Commercial projector was used as a light source (light intensity: 0.77 W/cm^2).

As shown in Figure 5.9, when the concentration of PDA-NPs falls within the range of 0-10 g/L, the temperature of solutions increases with increasing concentration. However, highly concentrated solutions (20 and 30 g/L) show decrease in temperature. We attribute this to the fact that the light penetration is reduced due to the high concentration of PDA-NPs, which prevents some of PDA-NPs from receiving light energy in the solution of 1

mm height (see details in sec. 5.2.4). Light penetration depths of 10, 20, and 30 g/L PDA-NP solutions calculated by Beer-Lambert Law were 235, 117, and 78 μm, respectively (Figure 5.6). We also calculated the photo-thermal efficiency of PDA-NP solution (30 g/L). With the commercial projector as a light source, the photo-thermal efficiency of the solution is ~25% (see details in sec. 5.2.6) that is comparable and even higher than those of previously reported photo-thermal agents, such as gold nanoparticles (η = 3.4 - 9.9%), gold nanorods (η = 17 - 22%) , and semiconductor nanoparticles (η = 27 – 30%) [195].
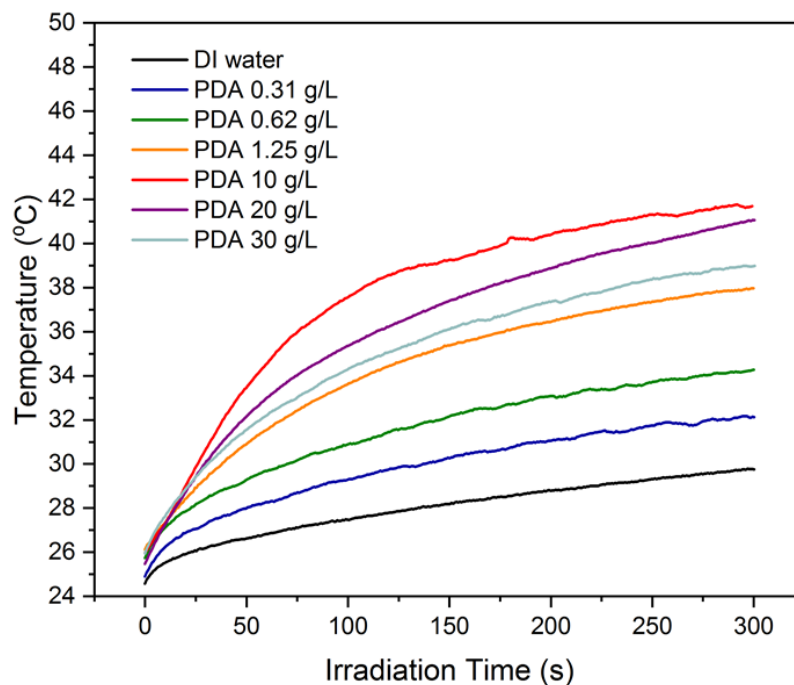
Figure 5.9. Photo-thermal effect of PDA-NPs

5.3.2. Characterization of photo-active hydrogel

The chromatophore cell of cephalopods uses radial muscles to control the size of the sac according to light. To implement this principle, it is necessary to create muscles using materials that react to light. In this study, the photo-active hydrogel was selected as a muscle in the artificial chromatophore cell, and it was fabricated by simply adding PDA-NPs into photo-curable precursor solution of thermo-responsive hydrogel, Poly(N-isopropylacrylamide) (PNIPAAm) hydrogel. PNIPAAm hydrogel is one of the most widely used thermo-responsive hydrogels, which exhibit a large and reversible volume change in water at its Lower Critical Solution Temperature (LCST, typically 32–35 °C) due to a coil-globule transition of the polymer networks [122, 160]. At a temperature below its LCST, NIPAAm molecules in an aqueous environment show a hydrophilic behavior, resulting in water uptake and swelling. When the temperature increases above the LCST, however, hydrophobic groups become more active, causing the significant volume shrinkage. The key attribute of photo-active hydrogel is its ability to change its degree of swelling in response to light irradiation due to embedded PDA-NPs generating heat. To quantify the swelling change, we use the swelling ratio (SR) in this study defined as a ratio of swollen length to the original length (as fabricated). For example, the SR is greater than 1 when the hydrogel swells and gets bigger than the fabrication dimension at low temperature, and the SR is less than 1 when it shrinks and becomes smaller than the fabrication dimension at high temperature.

First, we observed the overall swelling behavior of photo-active hydrogels, which were located in a temperature-controlled water chamber, in response to temperature (Figure 5.10). Disk-shaped samples with a diameter of 4.8 mm and a thickness of 300 μm were

fabricated using UV oven (see details in sec. 5.2.7). The NIPAAm and cross-linker (PEGDA 700) concentrations of the photo-curable precursor solution used in this study were 2.6 M and 0.36 M in ethanol, respectively. Four samples were prepared with different PDA-NP concentrations, 0, 10, 20, and 30 g/L. As shown in Figure 5.10, all the samples swell at low temperature and shrink at high temperature. Also, as the content of PDA in the hydrogel sample increases, the swelling ratio of the hydrogel decreases over the entire temperature range (10 - 60 $^{\circ}$C). This is attributed to the fact that the PDA-NPs having abundant catechol functional groups on their surfaces confers multiple cross-linking to the hydrogels, including non-covalent and covalent cross-linking [196, 197].
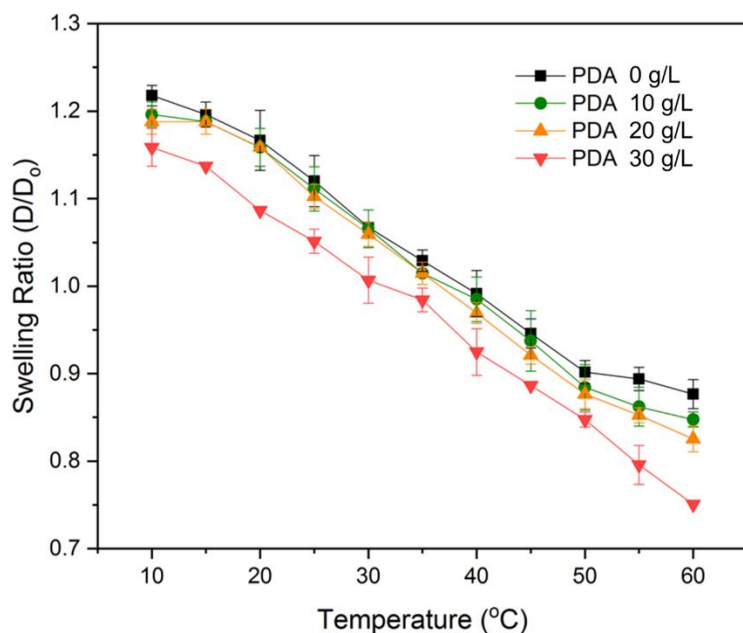
Figure 5.10. Temperature dependent swelling/shrinkage of photo-active hydrogel

We also investigated the temperature change of photo-active hydrogels in response to light irradiation (Figure 5.11). Based on the findings in sec. 5.3.1, higher concentrations of PDA-NPs generate more heat energy, resulting in a higher temperature of the sample. To study the effects of PDA concentration on temperature change of photo-active hydrogel, four disk-shaped samples were prepared with different PDA-NP concentrations, 0, 10, 20, and 30 g/L. The samples were placed under the projection light in air after removing water from the sample surface with a Kimwipe. Then, sample temperature was monitored with a thermal camera. Overall, PDA-NPs generate enough heat to increase the temperature of the hydrogel sample, and the maximum temperature can be achieved within 500 seconds (Figure 5.11). Samples made with 30 g/L of PDA-NPs showed a high temperature rise above 100 °C. These high temperatures of the samples indicate that our photo-active hydrogels can respond well even in water, which has a high heat capacity (4.184 J/g K).
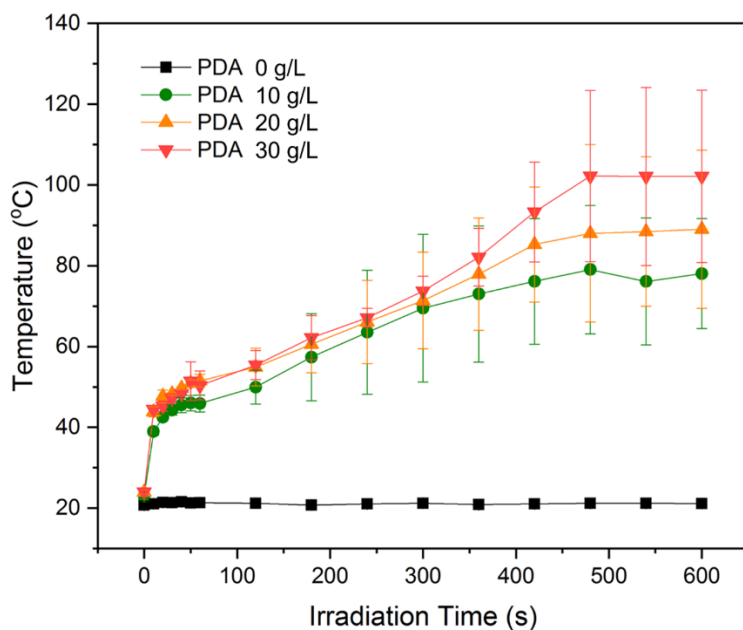
Figure 5.11. Light-induced temperature changes of photo-active hydrogels

The overall swelling behavior of photo-active hydrogels in response to light irradiation was investigated (Figure 5.12). Four disk-shaped samples were prepared with different PDA-NP concentrations, 0, 10, 20, and 30 g/L. The samples were placed under the projection light in air after removing water from the sample surface with a Kimwipe. Then, diameters of the samples were measured at every 1 minutes while light illuminating to calculate the swelling ratios. As shown in Figure 5.12, swelling ratio becomes smaller as light irradiates. This is because the thermal energy generated from PDA-NPs is transferred to PNIPAAm hydrogel, causing volume reduces of photo-active hydrogel. The degree of changes in swelling ratio of photo-active hydrogels is in good agreement with the results of swelling ratio study with a temperature-controlled water chamber (Figure 5.10). Pure PNIPAAm, which does not contain a PDA, also reduces the swelling ratio when illuminated. This is due to the heat associated with the light absorbance of the PNIPAAm hydrogel itself. In this study, the photo-active hydrogel made with 30 g/L of PDA-NPs was chosen as the material for the artificial muscle since it showed the greatest volume shrinkage (~30%) for the same amount of light energy.
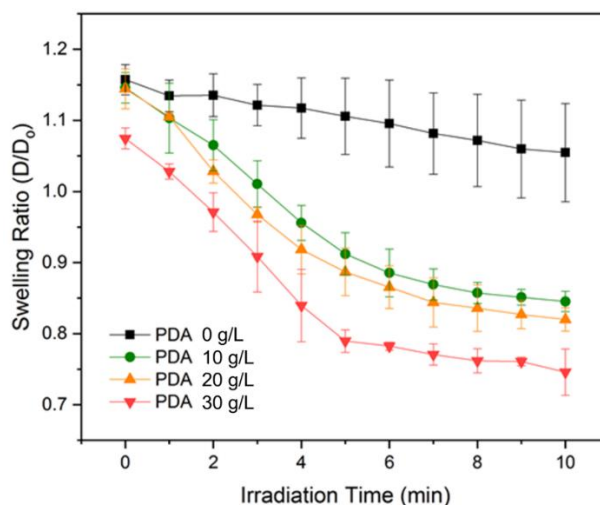
Figure 5.12. Light-induced shrinkage of photo-active hydrogels

Since the stretching of the sac is driven by the shrinkage of photo-active muscles, it is essential to measure the shrinkage stress of the photo-active hydrogel in order to design the artificial chromatophore. A rectangular PNIPAAm sample (30 mm x 5 mm x 150 μm) was prepared with 30 g/L of PDA-NPs. Then, the shrinkage stress generated as the temperature increased was obtained using a DMA with isostrain mode. Figure 5.13 shows that the hydrogel creates the maximum shrinkage stress of 176.1 kPa at 47 $^{\circ}$C. It indicates that the dynamic color modulation of the artificial chromatophore can be effectively implemented when the stress required to stretch our artificial sac by three times, which is the size difference of the sac shown by the actual chromatophore, is less than 176.1 kPa.
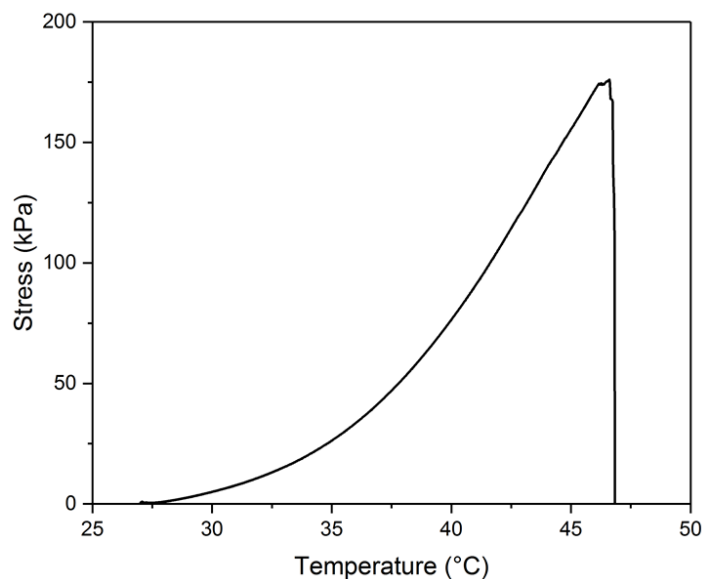
Figure 5.13. Shrinkage stress of photo-active hydrogel with increasing temperature

5.3.3. Characterization of stretchable AA hydrogel

In the chromatophore cell of actual cephalopods, sac can be stretched up to about three times by radial muscles. To achieve this capability, it is necessary to create an artificial sac with stretchable material that will not fracture when the sac is pulled more than three times. Hydrogels are usually composed of hydrophilic polymer chains, which can therefore hold a large amount of water molecules in the polymer networks. Swelling of polymer networks in water usually decreases their mechanical strengths, resulting in relatively brittle hydrogels. Therefore, intensive research has been going on to improve mechanical strengths and stretchability of hydrogels due to tremendous demands for tough hydrogels in various applications.

Double-network (DN) system, having two different polymer chain networks (long- and short-chain networks), exhibits a significant increase in the toughness of the hydrogels [198]. DN hydrogels usually rely on the fracture of a short-chain network for energy dissipation and the interpenetration of a long-chain network for maintaining high elasticity. However, the fracture of polymer chains usually induces irreversible permanent damage of polymer networks in hydrogels, resulting that the stress-strain hysteresis loops reduce over repeated deformation. Physical cross-linkers commonly used for the reversible cross-linking mechanism include hydrogen bonding [199-201], lamellar bi-layer [202], or ionic interaction [203]. Since these physical cross-linkers can be recovered in repeated loadings, it is possible to maintain the stress–strain hysteresis the same over cyclic loadings. For example, Xie group demonstrated a large and recoverable deformation of acrylic acid (AA) hydrogel fabricated with Fe^{3+} ions [204]. A reversible ionic crosslinking among the PAA polymer chains is enabled by Fe^{3+} ion, and a covalent cross-linking is achieved by covalent

cross-linker. Under deformation, the covalently cross-linked AA polymer chains remain intact to maintain their original configuration, while the ionic cross-linking enabled by Fe^{3+} ions is broken to dissipate energy. It is well-known that the mechanical properties of the AA hydrogels are significantly influenced by the contents of covalent cross-linkers and ions. In this study, the effects of cross-linker concentration and Fe^{3+} ion concentration on the mechanical properties of AA hydrogel were studied.

5.3.3.1. Effect of cross-linker concentration on mechanical properties of AA hydrogel

First, the AA hydrogels prepared with different cross-linker (PEGDA 700) contents were tested to study the effect of cross-linker concentration on mechanical properties of AA hydrogel. Six rectangular samples (25 mm x 4 mm x 1 mm) were prepared with different cross-linker concentrations, 0.02, 0.05, 0.10, 0.20, 0.40, and 0.80 M, in which the Fe^{3+} contents was fixed at 15 mM. Figure 5.14 shows the stress-strain curves, measured on a DMA, for 6 samples. By increasing the concentration of the covalent cross-linker (PEGDA 700), the elastic modulus of the hydrogel increased while the stretchability was reduced. The lower the cross-linker concentration, the lower the cross-linking density of the hydrogel, which results in a less brittle but relatively low elastic modulus. Specifically, the AA hydrogels fabricated with 0.02 M of cross-linker can be stretched up to three times (200 % strain) or more of its original length.
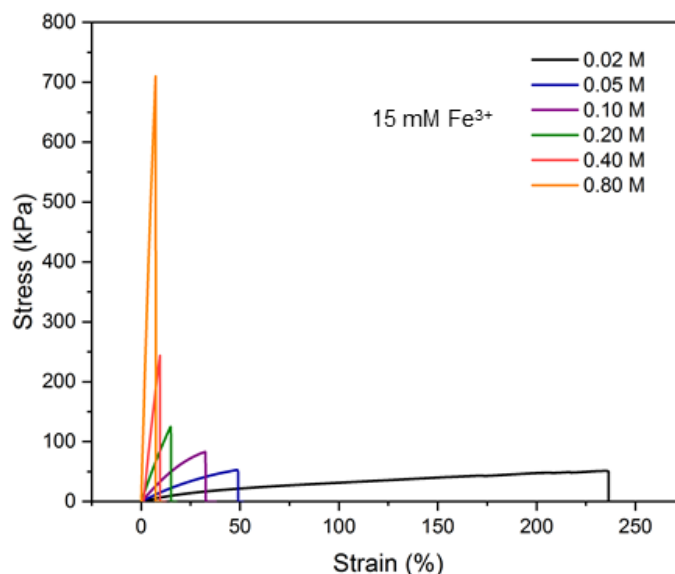
Figure 5.14. Effects of cross-linker concentration on mechanical properties of AA hydrogel

5.3.3.2. Effect of Fe^{3+} ion concentration on mechanical properties of AA hydrogel

We also studied the effect of Fe^{3+} ion concentration on mechanical properties of AA hydrogel. Seven rectangular AA hydrogel samples (25 mm x 4 mm x 1 mm) were fabricated with different Fe^{3+} ion contents, 0, 5, 10, 15, 20, 25, and 30 mM. The covalent cross-linker concentration was fixed at 0.02 M. As shown in Figure 5.15(a), introducing Fe^{3+} ions to the AA hydrogels can improve the mechanical properties significantly. The pure AA hydrogel fabricated without Fe^{3+} ion exhibits much weaker mechanical properties, with a strength of 4.42 kPa and a strain of 45.4%. When Fe^{3+} ion content is less than 10 mM, the increase in mechanical properties is not significant. However, when Fe^{3+} ions are introduced over 15 mM, the mechanical properties of AA hydrogel is dramatically enhanced. This indicates that a certain level of ion concentration is required to form double-

networks. Particularly, the strength was enhanced by more than 30 times (136.4 kPa), and strain was improved by more than 6 times (293.5%) from the pure AA hydrogel when the Fe^{3+} ion concentration was 20 mM. With higher concentration of Fe^{3+} ions, AA hydrogels, fabricated with 25 and 30 mM of Fe^{3+} ions, exhibit degraded strength and strain. It should be point out that Fe^{3+} ions have a negative influence on the free radical polymerization as well as initiate the polymerization [204]. Thus, high concentration of Fe^{3+} ions leads inhomogeneous cross-linking points in the networks, and less cross-linking density. In this study, an AA hydrogel made of 15 mM of Fe^{3+} ions, which can be stretched up to three times with lower stress (47.1 kPa), was chosen as the material for the artificial sac (Figure 5.15(b)). It is important to note that the stress required to stretch the hydrogel by three times is lower than the maximum shrinkage stress (176.1 kPa) of our photo-active hydrogel. It indicates that the area of sac can be effectively expanded through the stretching of the sac with our photo-active hydrogel muscles.
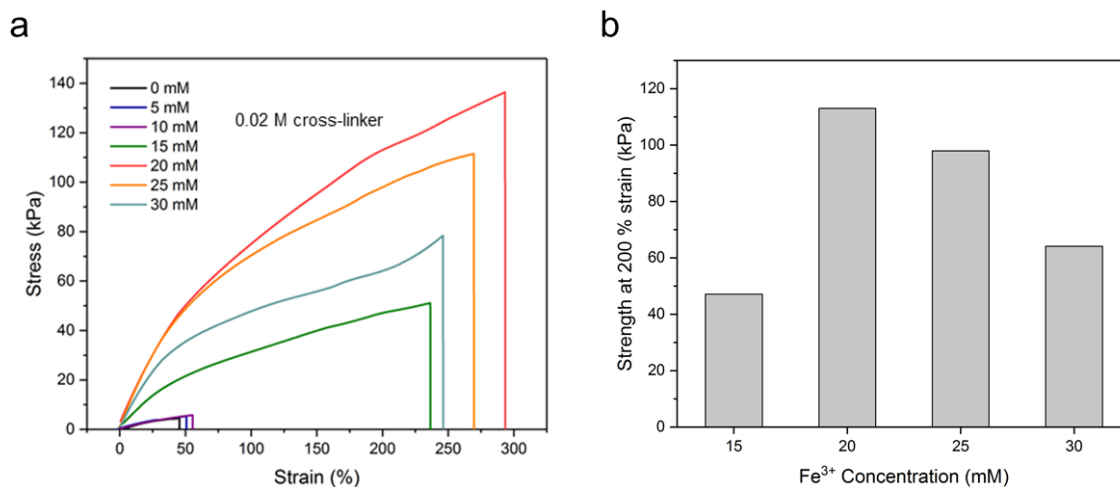
Figure 5.15. Mechanical properties of AA hydrogels according to Fe^{3+} ion concentration. (a) Stress-strain curves for seven AA hydrogel samples. (b) Strengths when AA hydrogels are stretched up to 200%.

5.3.4. Three components for artificial chromatophore and their materials

Artificial chromatophore consists of three parts: photo-active artificial muscles, a stretchable artificial sac, and a rigid frame (Figure 5.3). As discussed earlier, PNIPAAm hydrogel with 30 g/L of PDA-NPs and AA hydrogel with 15 mM of Fe^{3+} ions were selected as materials for the artificial muscles and the artificial sac, respectively. In order to effectively implement the function of the chromatophore using the hydrogels, a rigid frame is essential as a fixed boundary. PEGDA 250 was chosen as a material for rigid frame since it shows low swelling in water (less than 0.1%) and low thermal expansion at high temperature (less than 3% at 60 ^{o}C) (Figure 5.16(a)), and high mechanical strength (~8 MPa) (Figure 5.16(b)).
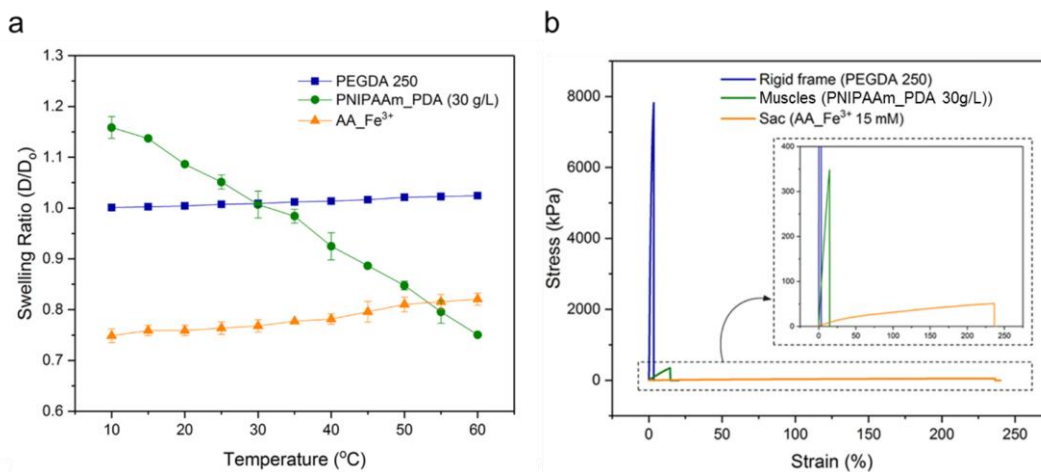
Figure 5.16. (a) Swelling behaviors of three materials according to temperature change: PEGDA 250 (blue squares), PNIPAAm with PDA (30 g/L) (green circles), and AA with Fe3^{+} ions (15 mM) (orange triangles) samples. (b) Mechanical properties of three materials: PEGDA 250 for rigid frame (blue line), PNIPAAm with PDA (30 g/L) (photo-active hydrogel) for artificial muscle (green line), and AA with Fe^{3+} ions (15 mM) for artificial sac (orange line).

Although a large number of multi-material 3D structures have been demonstrated with various multi-material 3D printing techniques, the weak bonding strength between different materials in the structure remains a critical problem. In particular, large forces could be applied to devices when large deformation is involved. Therefore, the bonding between materials could be broken when the bonding strength is too low, causing dissociation of the structure. As discussed earlier, PDA contains both catechol and amine groups in the structure, leading to the high adhesion to a wide range of substrates by forming covalent and noncovalent interactions with substrates. Therefore, PDA-NPs in our artificial muscle enhance the bonding strength with both materials, PEGDA 250 and AA hydrogel. The bonding stress and fracture strength were measured on a DMA. As shown in left half of graph in Figure 5.17, the higher the PDA concentration in photo-active hydrogel, the higher the bonding strength between the photo-active hydrogel and PEGDA structure. With 30 g/L of PDA-NPs, the bonding strength can be improved to 131 kPa, which is more than five times higher than the bonding strength (25 kPa) of sample without PDA-NPs. It is also two times greater than the fracture strength (51 kPa) of AA hydrogel with 15 mM Fe^{3+} ions. It shows that the bonding strength between the photo-active hydrogel and PEGDA 250 is large enough for demonstrating the artificial chromatophore. Also, the bonding strength between photo-active hydrogels and AA hydrogel was investigated (right half of graph in Figure 5.17). Since the bonding strength between two materials is higher than the fracture strength of AA hydrogel, fracture of AA hydrogel was found in all samples without material separation. Although the exact bonding strength between the two materials was not measured, the result shows that the interfacial bonding is sufficiently large to operate the artificial chromatophore.
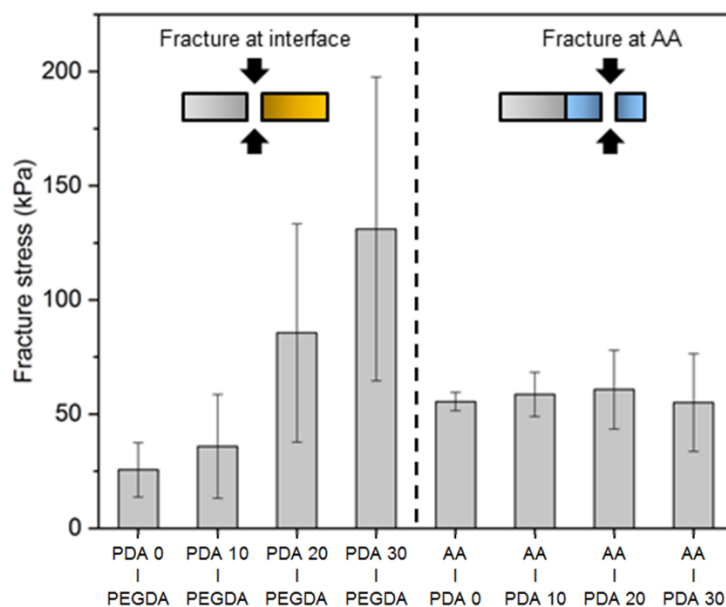
Figure 5.17. Bonding strengths between three materials, PNIPAAm with PDA-NPs, PEGDA 250, and AA with Fe^{3+} ions (15 mM)

5.3.5. 4D printing of bio-inspired adaptive camouflage skin

5.3.5.1. 4D printing of artificial chromatophore

An artificial chromatophore has been demonstrated using 4D printing approach, which is 3D printing with a programmed shape transformation in response to external energy input [25, 33, 34]. As discussed in Section 5.3.4, PEGDA 250, PNIPAAm hydrogel with 30 g/L of PDA-NPs, and AA hydrogel with 15 mM of Fe^{3+} ions were used as materials for a rectangular rigid frame, two photo-active muscles, and a stretchable sac, respectively (Figure 5.18(a)). To print the artificial chromatophore with multiple materials using MM-PµSL, we studied the light energy dosage required to cure a certain depth of each material in MM-PµSL to keep the layer thickness constant across materials (see details in sec. 5.2.15 and Figure 5.8). Based on the results from above curing depth studies, 3D printing of the artificial chromatophore with three materials was successfully achieved using MM-PµSL. First, the rigid frame was printed with length of 15 mm and width of 4.5 mm. Then, two separated photo-active muscles were created, length of 3 mm and width of 1.5 mm, to connect the muscles with the ends of the rigid frame. Finally, the stretchable sac was fabricated with the same dimension as the muscle between two separated muscles.

Since the muscles were fabricated by adding photo-thermal particles (PDA-NPs) to thermo-responsive hydrogel (PNIPAAm), the artificial chromatophore can be activated in response to two different external inputs, temperature changes and light irradiation. As discussed in Chapter 4, PNIPAAm hydrogel exhibits a large shrinkage at high temperatures. Thus, as the temperature increases, two muscle parts in the artificial chromatophore are

contracted and the sac connected with the muscles is stretched simultaneously. As shown in Figure 5.18(b), a 3D printed artificial chromatophore immersed in DI water exhibits a large shape deformation (or size changes of two parts) with changes in water temperature. When the temperature was raised to 50 $^{\circ}$C, the area of the sac (white part in the artificial chromatophore) expanded to about 40% (orange square line in Figure 5.18(c)), and the area of the muscles (black parts in the artificial chromatphore) reduced to about 55% (green circle line in Figure 5.18(c)). This increase in white area and reduction in black area effectively generate the optical effect.
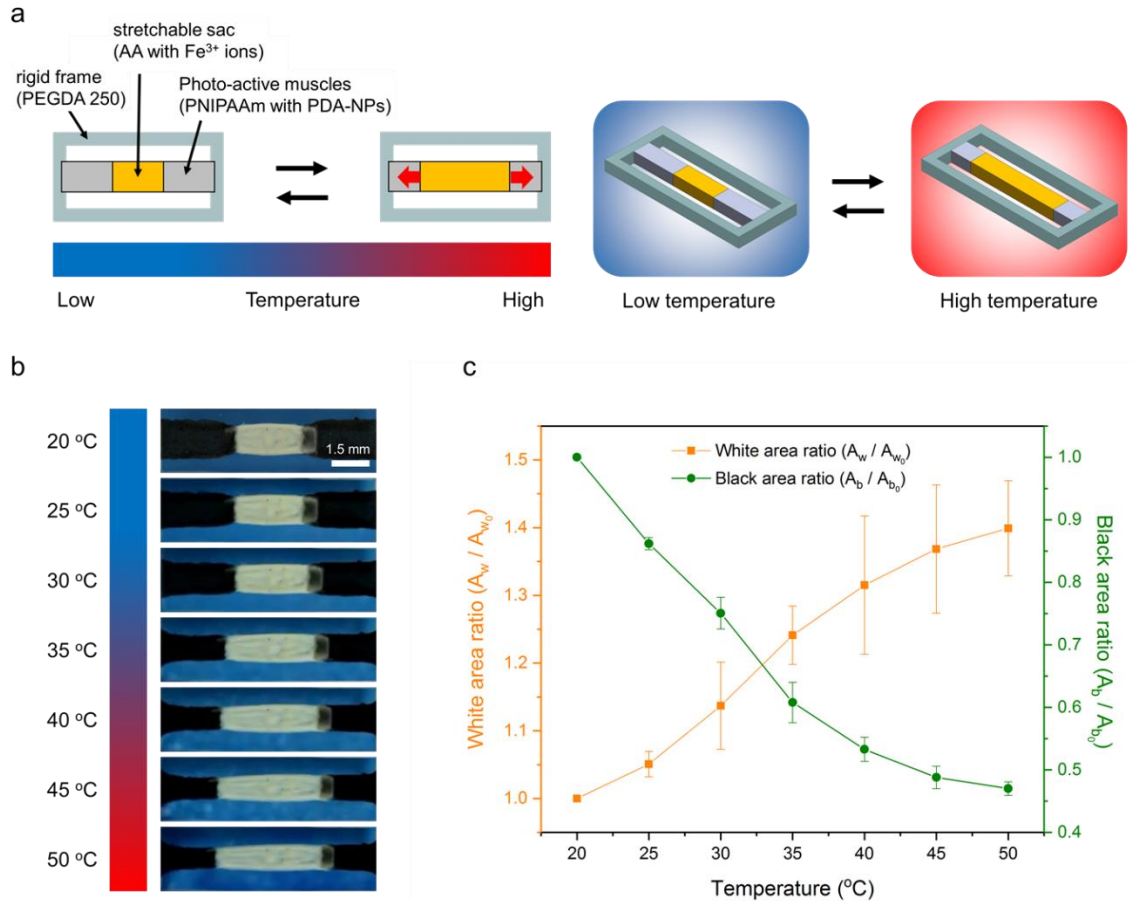
Figure 5.18. 4D printing of artificial chromatophore that respond to temperature changes. (a) Schematic illustration of the artificial chromatophore printed with three different materials. As the temperature increases, muscle contraction pulls the sac, causing an increase in the area of the sac. (b) Photo images of the artificial chromatophore at different temperatures. (c) Size changes of two different parts, sac (white area, orange square line) and muscles (black area, green circle line), at different temperatures.

5.3.5.2. Light-induced color change of artificial chromatophore

The activation of the artificial chromatophore was also achieved with light irradiation (Figure 5.19(a)). The 3D printed chromatophore structure was placed between two cover glasses with 100 μL of DI water. A white image (light intensity: 0.77 W/cm^2) was projected on the structure using a commercial beam projector, and photo images were taken using a digital camera to study the deformation of the structure. Under the light irradiation, the muscles were contracted and successfully stretched the sac up to about 40% (after 10 minutes) (Figure 5.19(b) and (c)). The figures shows that more than 95% of the total size change of the sac can be achieved with only two minutes of light irradiation. Also, we analyzed the optical effect generated by size changes of the sac using histogram of the photo images (Figure 5.20). As projection light was illuminated, the number of dark colored pixels in the photo image decreased and the number of bright colored pixels increased. It indicates that the color of the entire image is getting closer to the white image from the black-and-white blend image when light is irradiated. In consequence, our artificial chromatophores can effectively make optical effects, and be expected to create dynamic color changes using sacs of various colors.
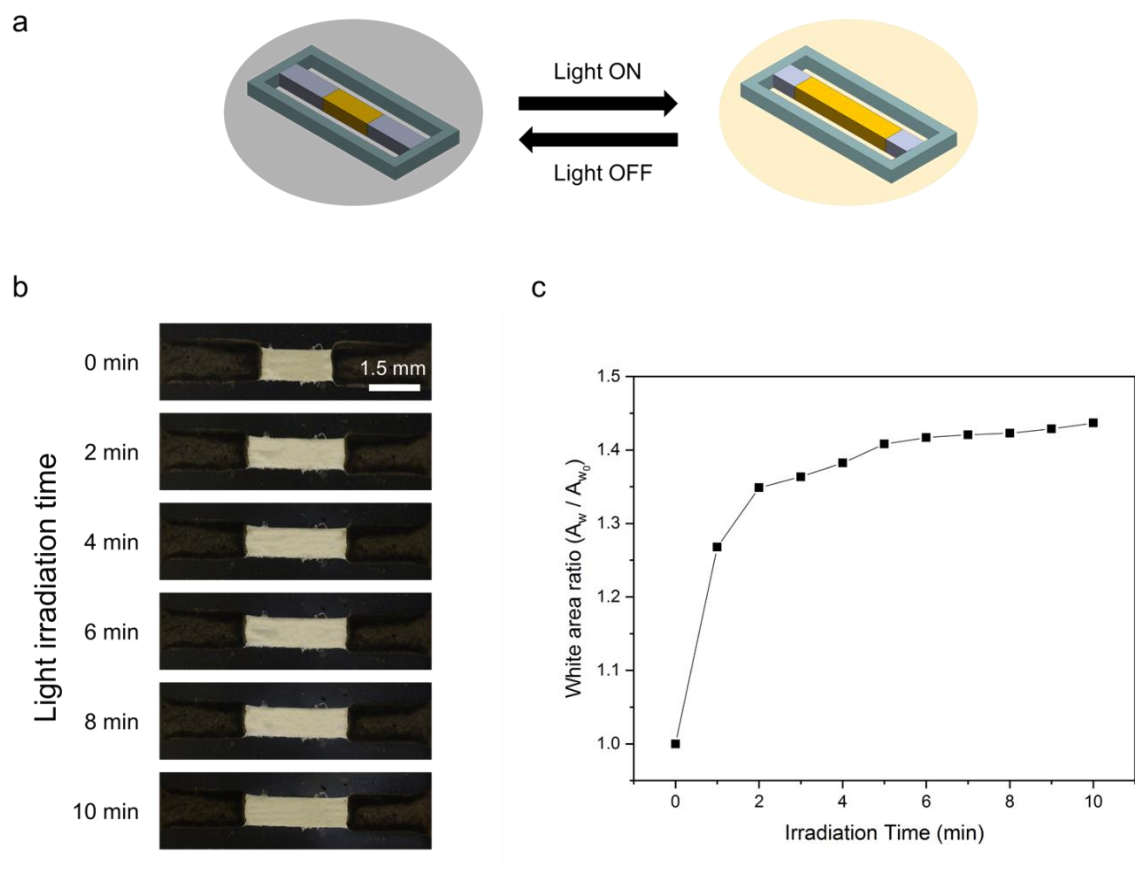
Figure 5.19. 4D printing of artificial chromatophore that respond to light irradiation. (a) Schematic illustration of the light-driven artificial chromatophore. (b) Photo images of the artificial chromatophore after light irradiation. A black paper was used as a background. (c) The changes in the size of the sac (white area) during light irradiation.
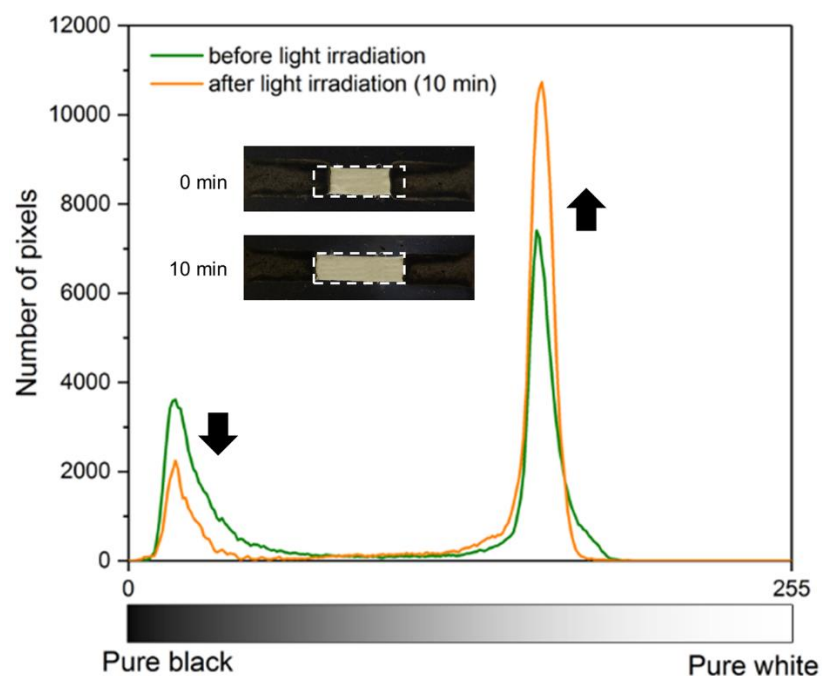
Figure 5.20. Analysis of optical effect generated by artificial chromatophore using histogram of the photo images. The histogram of selected area (white dash box) in the photo images was obtained using Image J.

5.3.5.3. Customized color patterning of bio-inspired adaptive camouflage skin

One of the amazing abilities of cephalopods is that chromatophores in their skin can be individually actuated without the brain control. Each chromatophore senses light and is quickly actuated to expand or contract its sac, allowing the creation of a variety of skin patterns according to surrounding. To demonstrate this remarkable ability, an array (3x1) of 3D artificial chromatophores was printed using MM-PµSL (Figure 5.21(a) and (b)). Then, the printed array structure was placed between two cover glasses with 300 µL of DI water. Four different light patterns (0-0-0, 0-0-1, 1-0-1, and 1-1-1) were projected on the array sample, where the first number, the second number, and the last number indicates top, middle, and bottom artificial chromatophore, respectively. Depending on the light pattern, the array sample showed different patterns of actuation. As shown in the Figure 5.21(c), only artificial chromatophores that is under light irradiation were fully stretched, indicating that the patterned projection light provides enough energy to increase the temperature of photo-active hydrogels. Artificial chromatophores next to the projection areas actuated with small degree (about 30% of fully stretched degree) because heat generated from the chromatophores under the light was transferred to the next chromatophores (Figure 5.21(d)). Although it reduces the contrast between actuated chromatophores and unactuated chromatophores, there is still a significant difference between them. It also can be resolved by changing the material or the design of the frame to reduce heat transfer between the chromatophores.
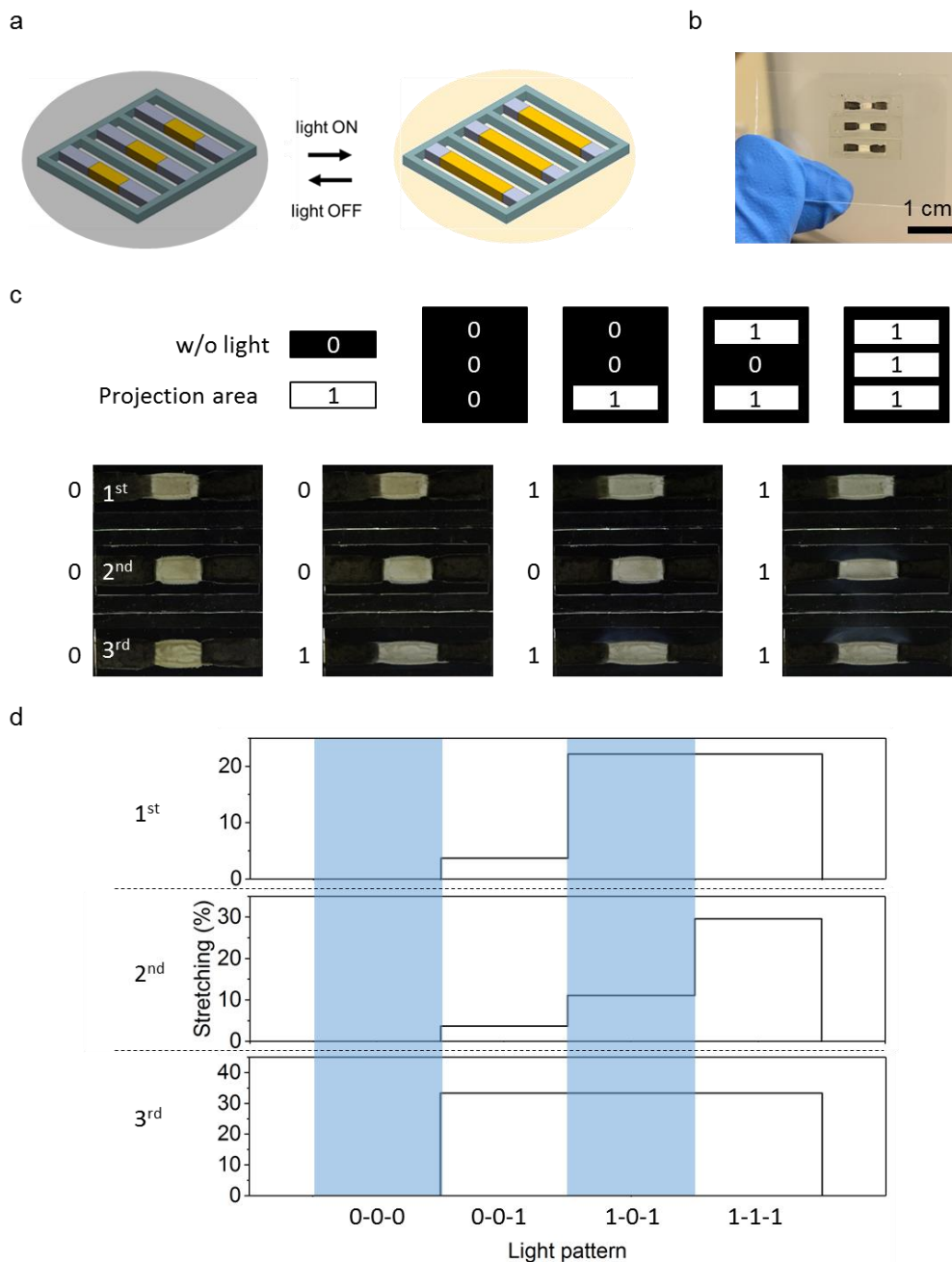
Figure 5.21. Bio-inspired adaptive camouflage skin having array of artificial chromatophores. (a) Schematic drawing for actuation mechanism of the array. (b) A 3D printed 3x1 artificial chromatophore array. (c) Four different light patterns for creating customized patterning of the array. (d) Stretching degrees of each artificial chromatophore in the array after projecting the patterns for 10 minutes.

5.4. Conclusion

In summary, we demonstrate a cephalopod-inspired adaptive camouflage skin with artificial chromatophores that can be modulated by light irradiation. The chromatophore consists of three parts: photo-active muscles, a stretchable sac, and a rigid frame. Photo-active hydrogel fabricated with PNIPAAm hydrogel including PDA-NPs used as photo-thermal effect materials. With 30 g/L of PDA-NPs, the photo-active hydrogel generated sufficient heat energy under light irradiation, resulting in volume shrinkage of the hydrogel (~30%). The stretchable AA hydrogel sac that can be stretched more than three times was achieved by forming a double network system with covalent cross-linker (PEGDA 700) and ionic cross-linker (Fe^{3+} ions). Bonding strengths between materials were enhanced by adding PDA-NPs. With these two hydrogels and PEGDA, artificial chromatophore was successfully printed using MM-PµSL, and the optical effect caused by the large area change of sac was demonstrated with light irradiation. We believe that our soft adaptive camouflage skin may lead to various applications in flexible display and electronics, bio-photonic devices, and dynamic camouflage interface.

Chapter 6

Conclusions and Future Work

6. Conclusions and Future Work

6.1. Conclusions

In this dissertation, we examined design and fabrication of multi-functional soft active devices based on an unconventional multi-material 3D printing system, multi-material projection micro-stereolithography (MM-PµSL), and soft active materials (stimuli-responsive hydrogels).

In Chapter 1, brief introduction on soft materials, systematic and comprehensive reviews on multi-material 3D printing systems and their applications, and motivations for this dissertation have been provided.

In Chapter 2, a novel multi-material 3D printing system, MM-PµSL, which provides rapid material exchange through dynamic fluidic control has been introduced. More than 95 % of the material can be exchanged in a few seconds, which confirms an order of magnitude faster performance than previously reported multi-material stereolithography techniques. Based on the results of the system characterization obtained in this study, we successfully demonstrated high-resolution 3D printing of multi-material structures.

Micro 3D printing of electroactive hydrogel (EAH) has been presented in Chapter 3. We found that the 3D printed EAH shows the largest bending deformation in an electrolyte with specific ionic strength (0.05 M PBS). The deformation is proportional to the applied electric field strength. We also identified that actuation time scale is linearly proportional to the characteristic thickness. Based on our findings, soft robotic

manipulation and locomotion were successfully achieved with 3D printed EAH devices fabricated using MM-PµSL.

Micro 3D fabrication of thermo-responsive hydrogel, PNIPAAm, has been reported in Chapter 4. We investigated the effects of various material and process parameters involved in the MM-PµSL process on the thermally responsive swelling of 3D printed PNIPAAm. We found that PNIPAAm swelling at low temperature and shrinking at high temperature can be independently controlled. We also revealed that 3D printed PNIPAAm swelling in the lateral and vertical directions is dependent on the layer thickness, through which anisotropic thermo-responsive swelling can be achieved by design. In addition, control of the swelling transition temperature of PNIPAAm was demonstrated by incorporating a hydrophilic ionic monomer. Consequently, soft thermo-responsive devices were successfully created using MM-PµSL.

Finally, a soft cephalopod-inspired adaptive camouflage skin, which employs multi-material artificial chromatophores, has been demonstrated in Chapter 5. To design the artificial chromatophore, we studied the photo-thermal effects of photo-active hydrogels, stretchability of AA hydrogels, and bonding strengths between three materials. We found that the photo-active hydrogel fabricated with 30 g/L of PDA-NPs generated sufficient thermal energy under light irradiation to make a contraction of photo-active muscle. We also found that the sac, made of AA hydrogel with two different cross-linkers, can be stretched more than three times without fracture. In addition, the enhanced bonding strengths between materials were demonstrated with PDA-NPs. Based on our findings, the adaptive camouflage skin that shows the dynamic color modulation using the actual color change mechanism of cephalopod was successfully printed using MM-PµSL.

6.2. Future work

The results of this work open a new avenue for development of multi-functional soft active devices and systems. Through the high resolution manufacturing capabilities of MM-PµSL, a variety of classes of multi-functional soft active devices can be developed with multiple soft active materials, such as stimuli-responsive hydrogels and liquid crystal elastomers. Further research can be conducted with respect to the following aspects.

6.2.1. MM-PµSL of high viscous materials with low material consumption

Our MM-PµSL provides high resolution 3D printing, rapid material exchange, and a wide range of material selection, including polymers, ceramics, and metals [166]. However, a few limitations of the current system configurations include high material consumption and difficulty of printing with high viscous materials. As the fluidic cell of the current system has only one outlet, all used materials are collected in the same waste container, which leads to a mixture of waste materials. Thus, it ends up causing high material consumption because it is impossible to recycle used materials due to the difficulty in making the mixture back to the original materials. The material consumption can be effectively minimized by using air flow to remove existing material from the cell and adding as many outlets as the number of materials being used (Figure 6.1). With this configuration, study on fluid dynamics and design of the cell could be further needed for to achieve effective material exchange. Specifically, the cell should be designed to allow the existing material to be removed efficiently without residues by airflow and the next material to be filled the cell without bubbles. Also, high viscous materials (greater than 1000 cP) could be available in

MM-PμSL by modifying the system using high power pumps and high-pressure tolerance fluidic cell and tubing to ensure adequate flow rates.
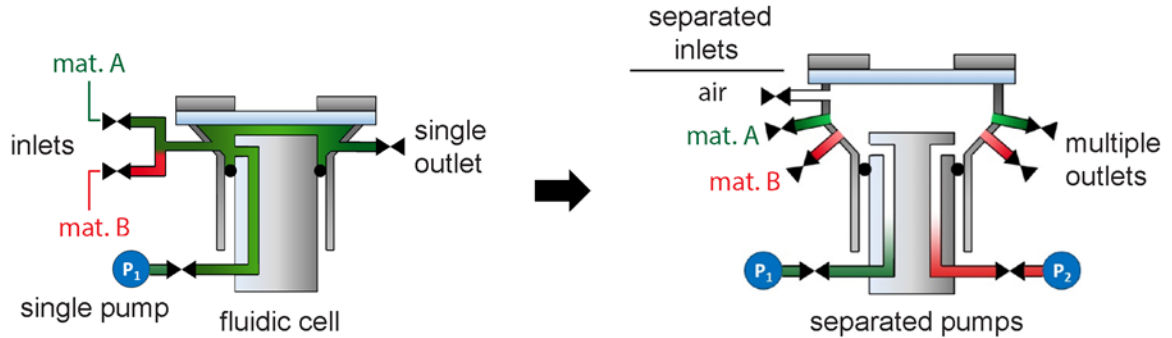
Figure 6.1. MM-PμSL with multiple outlets and separate pumps for material exchange with minimal material consumption

6.2.2. Development of bio-inspired multi-functional devices

In this dissertation, an adaptive camouflage skin has been demonstrated inspired by cephalopod. As seen, living creatures around us that show unique characteristics inspire us to develop new types of multi-functional devices, and our high resolution MM-PμSL enables the realization of these devices. For instance, mosquitoes that have a unique feeding duct with stiff jagged shafts on the sides can be used to show high tissue adhesion during the feeding process [205]. Inspired by this unique shape and function, functional devices that require high tissue adhesion can be developed, such as microneedles, medical patches, and adhesive tapes. Also, stomata on the leaf surface has a pair of guard cells that regulate the pore size. The pore is opened for gas exchange and transpiration [206]. Since this control of pore size could be easily achieved using stimuli-responsive hydrogels, MM-

PμSL would be effectively used to create stomata-inspired functional devices that control fluid flows, such as valves and pumps.
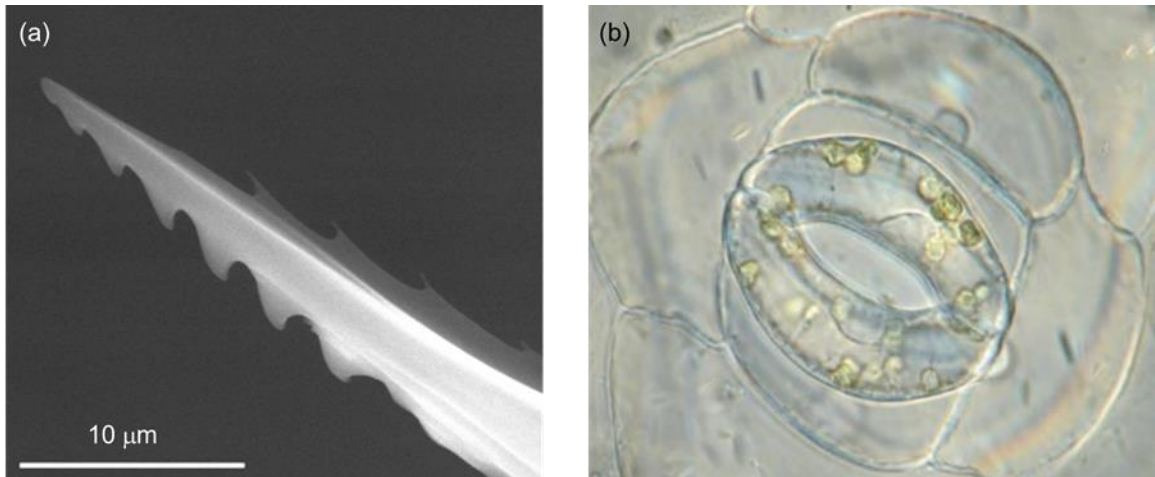
Figure 6.2. (a) The SEM image of a mosquito's fascicle with stiff jagged shafts on the sides. (b) Morphology of stomata having a pair of guard cells. The images are from [205, 206].

References

[1]   A.S. Hoffman, Hydrogels for biomedical applications, *Adv. Drug Del. Rev*. 64 (2012) 18-23.

[2]   K.Y. Lee, D.J. Mooney, Hydrogels for tissue engineering, *Chem. Rev*. 101(7) (2001) 1869-1880.

[3]   Y. Qiu, K. Park, Environment-sensitive hydrogels for drug delivery, *Adv. Drug Del. Rev*. 53(3) (2001) 321-339.

[4]   N.A. Peppas, J.Z. Hilt, A. Khademhosseini, R. Langer, Hydrogels in biology and medicine: from molecular principles to bionanotechnology, *Adv. Mater*. 18(11) (2006) 1345-1360.

[5]   G. Grassi, R. Farra, P. Caliceti, G. Guarnieri, S. Salmaso, M. Carenza, M. Grassi, Temperature-sensitive hydrogels, *Am. J. Drug Delivery* 3(4) (2005) 239-251.

[6]   D. Schmaljohann, Thermo-and pH-responsive polymers in drug delivery, *Adv. Drug Del. Rev*. 58(15) (2006) 1655-1670.

[7]   T.G. Park, Temperature modulated protein release from pH/temperature-sensitive hydrogels, *Biomaterials* 20(6) (1999) 517-521.

[8]   F.D. Jochum, P. Theato, Temperature-and light-responsive smart polymer materials, *Chem. Soc. Rev*. 42(17) (2013) 7468-7483.

[9]   I. Tomatsu, K. Peng, A. Kros, Photoresponsive hydrogels for biomedical applications, *Adv. Drug Del. Rev*. 63(14-15) (2011) 1257-1266.

[10]   D. Szabo, G. Szeghy, M. Zrinyi, Shape transition of magnetic field sensitive polymer gels, *Macromolecules* 31(19) (1998) 6541-6548.

[11]   K. Sawahata, M. Hara, H. Yasunaga, Y. Osada, Electrically controlled drug delivery system using polyelectrolyte gels, *J. Controlled Release* 14(3) (1990) 253-262.

[12]   J. Dolbow, E. Fried, H. Ji, Chemically induced swelling of hydrogels, *J. Mech. Phys. Solids* 52(1) (2004) 51-84.

[13]   M.A.C. Stuart, W.T. Huck, J. Genzer, M. Müller, C. Ober, M. Stamm, G.B. Sukhorukov, I. Szleifer, V.V. Tsukruk, M. Urban, Emerging applications of stimuli-responsive polymer materials, *Nat. Mater*. 9(2) (2010) 101.

[14]   I.Y. Galaev, B. Mattiasson, 'Smart'polymers and what they could do in biotechnology and medicine, *Trends Biotechnol*. 17(8) (1999) 335-340.

[15] S.H. Gehrke, Synthesis, equilibrium swelling, kinetics, permeability and applications of environmentally responsive gels, *Responsive gels: volume transitions II*, Springer1993, pp. 81-144.

[16] J.P. Magnusson, A. Khan, G. Pasparakis, A.O. Saeed, W. Wang, C. Alexander, Ion-sensitive "isothermal" responsive polymers prepared in water, *J. Am. Chem. Soc*. 130(33) (2008) 10852-10853.

[17] Y. Maeda, T. Higuchi, I. Ikeda, Change in hydration state during the coil− globule transition of aqueous solutions of poly (N-isopropylacrylamide) as evidenced by FTIR spectroscopy, *Langmuir* 16(19) (2000) 7503-7509.

[18] M.M. Prange, H.H. Hooper, J.M. Prausnitz, Thermodynamics of aqueous systems containing hydrophilic polymers or gels, *AlChE J*. 35(5) (1989) 803-813.

[19] F. Ilmain, T. Tanaka, E. Kokufuta, Volume transition in a gel driven by hydrogen bonding, *Nature* 349(6308) (1991) 400.

[20] J.H. Na, A.A. Evans, J. Bae, M.C. Chiappelli, C.D. Santangelo, R.J. Lang, T.C. Hull, R.C. Hayward, Programming reversibly self-folding origami with micropatterned photo-crosslinkable polymer trilayers, *Adv. Mater*. 27(1) (2015) 79-85.

[21] X. Zhang, C.L. Pint, M.H. Lee, B.E. Schubert, A. Jamshidi, K. Takei, H. Ko, A. Gillies, R. Bardhan, J.J. Urban, Optically-and thermally-responsive programmable materials based on carbon nanotube-hydrogel polymer composites, *Nano Lett*. 11(8) (2011) 3239-3244.

[22] Y. Mao, Z. Ding, C. Yuan, S. Ai, M. Isakov, J. Wu, T. Wang, M.L. Dunn, H.J. Qi, 3D printed reversible shape changing components with stimuli responsive materials, *Sci. Rep*. 6 (2016) 24761.

[23] J.C. Breger, C. Yoon, R. Xiao, H.R. Kwag, M.O. Wang, J.P. Fisher, T.D. Nguyen, D.H. Gracias, Self-folding thermo-magnetically responsive soft microgrippers, *ACS Appl. Mater. Inter*. 7(5) (2015) 3398-3405.

[24] J. Mu, C. Hou, H. Wang, Y. Li, Q. Zhang, M. Zhu, Origami-inspired active graphene-based paper for programmable instant self-folding walking devices, *Sci. Adv*. 1(10) (2015) e1500533.

[25] A.S. Gladman, E.A. Matsumoto, R.G. Nuzzo, L. Mahadevan, J.A. Lewis, Biomimetic 4D printing, *Nat. Mater*. 15(4) (2016) 413.

[26] S.E. Bakarich, R. Gorkin III, M.I.H. Panhuis, G.M. Spinks, 4D printing with mechanically robust, thermally actuating hydrogels, *Macromol. Rapid Commun*. 36(12) (2015) 1211-1217.

[27] D.G. Karis, R.J. Ono, M. Zhang, A. Vora, D. Storti, M.A. Ganter, A. Nelson, Cross-linkable multi-stimuli responsive hydrogel inks for direct-write 3D printing, *Polym. Chem*. 8(29) (2017) 4199-4206.

[28]   C.W. Hull, Apparatus for production of three-dimensional objects by stereolithography, Google Patents, 1986.

[29]   K.V. Wong, A. Hernandez, A review of additive manufacturing, *ISRN Mech. Eng.* 2012 (2012).

[30]   R.L. Truby, J.A. Lewis, Printing soft matter in three dimensions, *Nature* 540(7633) (2016) 371-378.

[31]   S.V. Murphy, A. Atala, 3D bioprinting of tissues and organs, *Nat. Biotechnol.* 32(8) (2014) 773.

[32]   D.B. Kolesky, R.L. Truby, A.S. Gladman, T.A. Busbee, K.A. Homan, J.A. Lewis, 3D bioprinting of vascularized, heterogeneous cell-laden tissue constructs, *Adv. Mater.* 26(19) (2014) 3124-3130.

[33]   S. Tibbits, 4D printing: multi-material shape change, *Archit. Design* 84(1) (2014) 116-121.

[34]   C. Yang, M. Boorugu, A. Dopp, J. Ren, R. Martin, D. Han, W. Choi, H. Lee, 4D printing reconfigurable, deployable and mechanically tunable metamaterials, *Mater. Horiz.* (2019).

[35]   M. Schaffner, J.A. Faber, L. Pianegonda, P.A. Rühs, F. Coulter, A.R. Studart, 3D printing of robotic soft actuators with programmable bioinspired architectures, *Nat. Commun.* 9(1) (2018) 878.

[36]   M.O. Saed, C.P. Ambulo, H. Kim, R. De, V. Raval, K. Searles, D.A. Siddiqui, J.M.O. Cue, M.C. Stefan, M.R. Shankar, Molecularly-Engineered, 4D-Printed Liquid Crystal Elastomer Actuators, *Adv. Funct. Mater.* 29(3) (2019) 1806412.

[37]   T.S. Wei, B.Y. Ahn, J. Grotto, J.A. Lewis, 3D printing of customized li-ion batteries with thick electrodes, *Adv. Mater.* 30(16) (2018) 1703027.

[38]   S.H. Park, R. Su, J. Jeong, S.Z. Guo, K. Qiu, D. Joung, F. Meng, M.C. McAlpine, 3D printed polymer photodetectors, *Adv. Mater.* 30(40) (2018) 1803980.

[39]   D. Joung, V. Truong, C.C. Neitzke, S.Z. Guo, P.J. Walsh, J.R. Monat, F. Meng, S.H. Park, J.R. Dutton, A.M. Parr, 3D Printed Stem-Cell Derived Neural Progenitors Generate Spinal Cord Scaffolds, *Adv. Funct. Mater.* 28(39) (2018) 1801850.

[40]   J.O. Hardin, T.J. Ober, A.D. Valentine, J.A. Lewis, Microfluidic printheads for multimaterial 3D printing of viscoelastic inks, *Adv. Mater.* 27(21) (2015) 3279-3284.

[41]   S. Zheng, M. Zlatin, P.R. Selvaganapathy, M.A. Brook, Multiple modulus silicone elastomers using 3D extrusion printing of low viscosity inks, *Addit. Manuf.* 24 (2018) 86-92.

[42]   D. Kokkinis, F. Bouville, A.R. Studart, 3D printing of materials with tunable failure via bioinspired mechanical gradients, *Adv. Mater.* 30(19) (2018) 1705808.

[43]   N. Mohan, P. Senthil, S. Vinodh, N. Jayanth, A review on composite materials and process parameters optimisation for the fused deposition modelling process, *Virtual Phys. Prototyp.* 12(1) (2017) 47-59.

[44]   D. Espalin, J. Alberto Ramirez, F. Medina, R. Wicker, Multi-material, multi-technology FDM: exploring build process variations, *Rapid Prototyp. J.* 20(3) (2014) 236-244.

[45]   I. Gibson, D.W. Rosen, B. Stucker, *Additive manufacturing technologies*, Springer2014.

[46]   M.A.H. Khondoker, A. Asad, D. Sameoto, Printing with mechanically interlocked extrudates using a custom bi-extruder for fused deposition modelling, *Rapid Prototyp. J.* 24(6) (2018) 921-934.

[47]   C.B. Sweeney, B.A. Lackey, M.J. Pospisil, T.C. Achee, V.K. Hicks, A.G. Moran, B.R. Teipel, M.A. Saed, M.J. Green, Welding of 3D-printed carbon nanotube–polymer composites by locally induced microwave heating, *Sci. Adv.* 3(6) (2017) e1700262.

[48]   Z. Ding, C. Yuan, X. Peng, T. Wang, H.J. Qi, M.L. Dunn, Direct 4D printing via active composite materials, *Sci. Adv.* 3(4) (2017) e1602890.

[49]   S. Sundaram, M. Skouras, D.S. Kim, L. van den Heuvel, W. Matusik, Topology optimization and 3D printing of multimaterial magnetic actuators and displays, *Sci. Adv.* 5(7) (2019) eaaw1160.

[50]   P. Sitthi-Amorn, J.E. Ramos, Y. Wangy, J. Kwan, J. Lan, W. Wang, W. Matusik, MultiFab: a machine vision assisted platform for multi-material 3D printing, *ACM Trans. Graph.* 34(4) (2015) 129.

[51]   J. Ledesma-Fernandez, C. Tuck, R. Hague, High Viscosity Jetting of Conductive and Dielectric Pastes for Printed Electronics, *Proceedings of the International Solid Freeform Fabrication Symposium*, 2015, pp. 40-55.

[52]   V. Chan, J.H. Jeong, P. Bajaj, M. Collens, T. Saif, H. Kong, R. Bashir, Multi-material biofabrication of hydrogel cantilevers and actuators with stereolithography, *Lab Chip* 12(1) (2012) 88-98.

[53]   J.-W. Choi, H.-C. Kim, R. Wicker, Multi-material stereolithography, *J. Mater. Process. Technol.* 211(3) (2011) 318-328.

[54]   L. Overmeyer, A. Hohnholz, O. Suttmann, S. Kaierle, Multi-material laser direct writing of aerosol jet layered polymers, *CIRP Annals* (2019).

[55]   F. Mayer, S. Richter, J. Westhauser, E. Blasco, C. Barner-Kowollik, M. Wegener, Multimaterial 3D laser microprinting using an integrated microfluidic system, *Sci. Adv.* 5(2) (2019) eaau9160.

[56]   J.R. Tumbleston, D. Shirvanyants, N. Ermoshkin, R. Janusziewicz, A.R. Johnson, D. Kelly, K. Chen, R. Pinschmidt, J.P. Rolland, A. Ermoshkin, Continuous liquid interface production of 3D objects, *Science* 347(6228) (2015) 1349-1352.

[57]   B.E. Kelly, I. Bhattacharya, H. Heidari, M. Shusteff, C.M. Spadaccini, H.K. Taylor, Volumetric additive manufacturing via tomographic reconstruction, *Science* 363(6431) (2019) 1075-1079.

[58]   D.A. Walker, J.L. Hedrick, C.A. Mirkin, Rapid, large-volume, thermally controlled 3D printing using a mobile liquid interface, *Science* 366(6463) (2019) 360-364.

[59]   C. Zhou, Y. Chen, Z. Yang, B. Khoshnevis, Digital material fabrication using mask-image-projection-based stereolithography, *Rapid Prototyp. J*. 19(3) (2013) 153-165.

[60]   Q. Ge, A.H. Sakhaei, H. Lee, C.K. Dunn, N.X. Fang, M.L. Dunn, Multimaterial 4D printing with tailorable shape memory polymers, *Sci. Rep*. 6 (2016) 31110.

[61]   D. Chen, X. Zheng, Multi-material additive manufacturing of metamaterials with giant, tailorable negative Poisson's ratios, *Sci. Rep*. 8(1) (2018) 9139.

[62]   K. Kowsari, S. Akbari, D. Wang, N.X. Fang, Q. Ge, High-Efficiency High-Resolution Multimaterial Fabrication for Digital Light Processing-Based Three-Dimensional Printing, *3D Print. Addit Manuf.* 5(3) (2018) 185-193.

[63]   N.D. Dolinski, Z.A. Page, E.B. Callaway, F. Eisenreich, R.V. Garcia, R. Chavez, D.P. Bothman, S. Hecht, F.W. Zok, C.J. Hawker, Solution Mask Liquid Lithography (SMaLL) for One-Step, Multimaterial 3D Printing, *Adv. Mater.* 30(31) (2018) 1800364.

[64]   J. Schwartz, A. Boydston, Multimaterial actinic spatial control 3D and 4D printing, *Nat. Commun.* 10(1) (2019) 791.

[65]   Y.F. Zhang, N. Zhang, H. Hingorani, N. Ding, D. Wang, C. Yuan, B. Zhang, G. Gu, Q. Ge, Fast-Response, Stiffness-Tunable Soft Actuator by Hybrid Multimaterial 3D Printing, *Adv. Funct. Mater.* 29(15) (2019) 1806698.

[66]   M. Vatani, Y. Lu, E.D. Engeberg, J.-W. Choi, Combined 3D printing technologies and material for fabrication of tactile sensors, *Int. J. Pr. Eng. Manuf.* 16(7) (2015) 1375-1383.

[67]   A.D. Valentine, T.A. Busbee, J.W. Boley, J.R. Raney, A. Chortos, A. Kotikian, J.D. Berrigan, M.F. Durstock, J.A. Lewis, Hybrid 3D printing of soft electronics, *Adv. Mater.* 29(40) (2017) 1703817.

[68]   D.J. Roach, C.M. Hamel, C.K. Dunn, M.V. Johnson, X. Kuang, H.J. Qi, The m4 3D printer: A multi-material multi-method additive manufacturing platform for future 3D printed structures, *Addit. Manuf.* 29 (2019) 100819.

[69] T. Wohlers, *Wohlers Report 2017 3D Printing and Additive Manufacturing State of the Industry Annual Worldwide Progress Report*. Fort Collins, Colorado, USA: Wohlers Associates, Inc, 2017.

[70] Y. Lu, S.N. Mantha, D.C. Crowder, S. Chinchilla, K.N. Shah, Y.H. Yun, R.B. Wicker, J.-W. Choi, Microstereolithography and characterization of poly (propylene fumarate)-based drug-loaded microneedle arrays, *Biofabrication* 7(4) (2015) 045001.

[71] F. Li, N.P. Macdonald, R.M. Guijt, M.C. Breadmore, Multimaterial 3D Printed Fluidic Device for Measuring Pharmaceuticals in Biological Fluids, *Anal. Chem.* 91(3) (2018) 1758-1763.

[72] G. Coelho, T.M.F. Chaves, A.F. Goes, E.C. Del Massa, O. Moraes, M. Yoshida, Multimaterial 3D printing preoperative planning for frontoethmoidal meningoencephalocele surgery, *Childs Nerv. Syst.* 34(4) (2018) 749-756.

[73] Cresswell-Boyes, A. Barber, D. Mills, A. Tatla, G. Davis, Approaches to 3D printing teeth from X-ray microtomography, *J. Microsc.* 272(3) (2018) 207-212.

[74] F. Ilievski, A.D. Mazzeo, R.F. Shepherd, X. Chen, G.M. Whitesides, Soft robotics for chemists, *Angew. Chem. Int. Ed.* 50(8) (2011) 1890-1895.

[75] T. Wallin, J. Pikul, R. Shepherd, 3D printing of soft robotic systems, *Nat. Rev. Mater.* 3(6) (2018) 84.

[76] C. Yuan, D.J. Roach, C.K. Dunn, Q. Mu, X. Kuang, C.M. Yakacki, T. Wang, K. Yu, H.J. Qi, 3D printed reversible shape changing soft actuators assisted by liquid crystal elastomers, *Soft Matter* 13(33) (2017) 5558-5568.

[77] D. Espalin, D.W. Muse, E. MacDonald, R.B. Wicker, 3D Printing multifunctionality: structures with electronics, *Int. J. Adv. Manuf. Tech.* 72(5-8) (2014) 963-978.

[78] W. HuangáGoh, A. HoseináSakhaei, Highly stretchable hydrogels for UV curing based high-resolution multimaterial 3D printing, *J. Mater. Chem. B* 6(20) (2018) 3246-3253.

[79] D.L. Bourell, J.J. Beaman, M.C. Leu, D.W. Rosen, A brief history of additive manufacturing and the 2009 roadmap for additive manufacturing: looking back and looking ahead, *Proceedings of RapidTech* (2009) 24-25.

[80] J.A. Lewis, Direct ink writing of 3D functional materials, *Adv. Funct. Mater.* 16(17) (2006) 2193-2204.

[81] J.A. Lewis, G.M. Gratson, Direct writing in three dimensions, *Mater. Today* 7(7-8) (2004) 32-39.

[82] Mohamed, S.H. Masood, J.L. Bhowmik, Optimization of fused deposition modeling process parameters: a review of current research and future prospects, *Adv. Manuf.* 3(1) (2015) 42-53.

[83]   B.J. De Gans, P.C. Duineveld, U.S. Schubert, Inkjet printing of polymers: state of the art and future developments, *Adv. Mater.* 16(3) (2004) 203-213.

[84]   H. Kodama, Automatic method for fabricating a three-dimensional plastic model with photo-hardening polymer, *Rev. Sci. Instrum.* 52(11) (1981) 1770-1773.

[85]   S. Maruo, O. Nakamura, S. Kawata, Three-dimensional microfabrication with two-photon-absorbed photopolymerization, *Opt. Lett.* 22(2) (1997) 132-134.

[86]   B.H. Cumpston, S.P. Ananthavel, S. Barlow, D.L. Dyer, J.E. Ehrlich, L.L. Erskine, A.A. Heikal, S.M. Kuebler, I.-Y.S. Lee, D. McCord-Maughon, Two-photon polymerization initiators for three-dimensional optical data storage and microfabrication, *Nature* 398(6722) (1999) 51.

[87]   J.W. Stansbury, M.J. Idacavage, 3D printing with polymers: Challenges among expanding options and opportunities, *Dent. Mater.* 32(1) (2016) 54-64.

[88]   W.E. Frazier, Metal additive manufacturing: a review, *J. Mater. Eng. Perform.* 23(6) (2014) 1917-1928.

[89]   H. Seitz, W. Rieder, S. Irsen, B. Leukers, C. Tille, Three-dimensional printing of porous ceramic scaffolds for bone tissue engineering, *J. Biomed. Mater. Res., Part B: An Official Journal of The Society for Biomaterials, The Japanese Society for Biomaterials, and The Australian Society for Biomaterials and the Korean Society for Biomaterials* 74(2) (2005) 782-788.

[90]   D. Isakov, Q. Lei, F. Castles, C. Stevens, C. Grovenor, P. Grant, 3D printed anisotropic dielectric composite with meta-material features, *Mater. Des.* 93 (2016) 423-430.

[91]   H.N. Chia, B.M. Wu, Recent advances in 3D printing of biomaterials, *J. Biol. Eng.* 9(1) (2015) 4.

[92]   Q. Wang, J.A. Jackson, Q. Ge, J.B. Hopkins, C.M. Spadaccini, N.X. Fang, Lightweight mechanical metamaterials with tunable negative thermal expansion, *Phys. Rev. Lett.* 117(17) (2016) 175901.

[93]   S. Babaee, J. Shim, J.C. Weaver, E.R. Chen, N. Patel, K. Bertoldi, 3D soft metamaterials with negative Poisson's ratio, *Adv. Mater.* 25(36) (2013) 5044-5049.

[94]   C.L. Ventola, Medical applications for 3D printing: current and projected uses, *Pharm. Ther.* 39(10) (2014) 704.

[95]   J.A. Lewis, B.Y. Ahn, Device fabrication: Three-dimensional printed electronics, *Nature* 518(7537) (2015) 42.

[96]   S. Bose, S. Vahabzadeh, A. Bandyopadhyay, Bone tissue engineering using 3D printing, *Mater. Today* 16(12) (2013) 496-504.

[97] S.M. Peltola, F.P. Melchels, D.W. Grijpma, M. Kellomäki, A review of rapid prototyping techniques for tissue engineering purposes, *Ann. Med.* 40(4) (2008) 268-280.

[98] S. Khalil, J. Nam, W. Sun, Multi-nozzle deposition for construction of 3D biopolymer tissue scaffolds, *Rapid Prototyp. J.* 11(1) (2005) 9-17.

[99] D. Kokkinis, M. Schaffner, A.R. Studart, Multimaterial magnetically assisted 3D printing of composite materials, *Nat. Commun.* 6 (2015) 8643.

[100] R. Melnikova, A. Ehrmann, K. Finsterbusch, 3D printing of textile-based structures by Fused Deposition Modelling (FDM) with different polymer materials, *IOP Conference Series: Materials Science and Engineering, IOP Publishing*, 2014, p. 012018.

[101] K. Wang, C. Wu, Z. Qian, C. Zhang, B. Wang, M.A. Vannan, Dual-material 3D printed metamaterials with tunable mechanical properties for patient-specific tissue-mimicking phantoms, *Addit. Manuf.* 12 (2016) 31-37.

[102] X. Mu, T. Bertron, C. Dunn, H. Qiao, J. Wu, Z. Zhao, C. Saldana, H. Qi, Porous polymeric materials by 3D printing of photocurable resin, *Mater. Horiz.* 4(3) (2017) 442-449.

[103] Q. Mu, L. Wang, C.K. Dunn, X. Kuang, F. Duan, Z. Zhang, H.J. Qi, T. Wang, Digital light processing 3D printing of conductive complex structures, *Addit. Manuf.* 18 (2017) 74-83.

[104] C. Zhou, Y. Chen, Z. Yang, B. Khoshnevis, Development of multi-material mask-image-projection-based stereolithography for the fabrication of digital materials, *Annual solid freeform fabrication symposium*, Austin, TX, 2011.

[105] H. Yun, H. Kim, Development of DMD-based micro-stereolithography apparatus for biodegradable multi-material micro-needle fabrication, *J. Mech. Sci. Technol.* 27(10) (2013) 2973-2978.

[106] C. Sun, N. Fang, D. Wu, X. Zhang, Projection micro-stereolithography using digital micro-mirror dynamic mask, *Sensor. Actuat. A-Phys* 121(1) (2005) 113-120.

[107] X. Zheng, J. Deotte, M.P. Alonso, G.R. Farquar, T.H. Weisgraber, S. Gemberling, H. Lee, N. Fang, C.M. Spadaccini, Design and optimization of a light-emitting diode projection micro-stereolithography three-dimensional manufacturing system, Rev. *Sci. Instrum.* 83(12) (2012) 125001.

[108] H. Lee, C. Xia, N.X. Fang, First jump of microgel; actuation speed enhancement by elastic instability, *Soft Matter* 6(18) (2010) 4342-4345.

[109] H. Lee, J. Zhang, H. Jiang, N.X. Fang, Prescribed pattern transformation in swelling gel tubes by elastic instability, *Phys. Rev. Lett.* 108(21) (2012) 214304.

[110] D. Han, Z. Lu, S.A. Chester, H. Lee, Micro 3D Printing of a Temperature-Responsive Hydrogel Using Projection Micro-Stereolithography, *Sci. Rep.* 8(1) (2018) 1963.

[111] D. Han, C. Farino, C. Yang, T. Scott, D. Browe, W. Choi, J.W. Freeman, H. Lee, Soft Robotic Manipulation and Locomotion with a 3D Printed Electroactive Hydrogel, *ACS Appl. Mater. Interfaces* (2018).

[112] X. Zheng, H. Lee, T.H. Weisgraber, M. Shusteff, J. DeOtte, E.B. Duoss, J.D. Kuntz, M.M. Biener, Q. Ge, J.A. Jackson, Ultralight, ultrastiff mechanical metamaterials, *Science* 344(6190) (2014) 1373-1377.

[113] Y.Y.C. Choong, S. Maleksaeedi, H. Eng, P.-C. Su, J. Wei, Curing characteristics of shape memory polymers in 3D projection and laser stereolithography, *Virtual Phys. Prototy.* 12(1) (2017) 77-84.

[114] R. Raman, B. Bhaduri, M. Mir, A. Shkumatov, M.K. Lee, G. Popescu, H. Kong, R. Bashir, High-Resolution Projection Microstereolithography for Patterning of Neovasculature, *Adv. Healthc. Mater.* 5(5) (2016) 610-619.

[115] H. Cui, R. Hensleigh, H. Chen, X. Zheng, Additive Manufacturing and size-dependent mechanical properties of three-dimensional microarchitected, high-temperature ceramic metamaterials, *J. Mater. Res.* 33(3) (2018) 360-371.

[116] J.R. Tumbleston, D. Shirvanyants, N. Ermoshkin, R. Janusziewicz, A.R. Johnson, D. Kelly, K. Chen, R. Pinschmidt, J.P. Rolland, A. Ermoshkin, Continuous liquid interface production of 3D objects, *Science* (2015) aaa2397.

[117] D. Dendukuri, S.S. Gu, D.C. Pregibon, T.A. Hatton, P.S. Doyle, Stop-flow lithography in a microfluidic device, *Lab Chip* 7(7) (2007) 818-828.

[118] F.M. White, *Fluid mechanics*, McGraw-hill, 1986.

[119] Gibson, D. Rosen, B. Stucker, Additive Manufacturing–3D Printing, *Rapid Prototyping, and Direct Digital Manufacturing*, Springer, New York, 2015.

[120] M. Mooney, The viscosity of a concentrated suspension of spherical particles, *J. colloid sci.* 6(2) (1951) 162-170.

[121] J.W. Lee, I.H. Lee, D.-W. Cho, Development of micro-stereolithography technology using metal powder, *Microelectron. Eng.* 83(4-9) (2006) 1253-1256.

[122] C. Wu, X. Wang, Globule-to-coil transition of a single homopolymer chain in solution, *Phys. Rev. Lett.* 80(18) (1998) 4092.

[123] T. Shiga, T. Kurauchi, Deformation of polyelectrolyte gels under the influence of electric field, *J. Appl. Polym. Sci.* 39(11-12) (1990) 2305-2320.

[124] R.V. Martinez, C.R. Fish, X. Chen, G.M. Whitesides, Elastomeric origami: programmable paper-elastomer composites as pneumatic actuators, *Adv. Funct. Mater.* 22(7) (2012) 1376-1384.

[125] B. Mosadegh, P. Polygerinos, C. Keplinger, S. Wennstedt, R.F. Shepherd, U. Gupta, J. Shim, K. Bertoldi, C.J. Walsh, G.M. Whitesides, Pneumatic networks for soft robotics that actuate rapidly, *Adv. Funct. Mater.* 24(15) (2014) 2163-2170.

[126] F. Ilievski, A.D. Mazzeo, R.F. Shepherd, X. Chen, G.M. Whitesides, Soft robotics for chemists, *Angew. Chem.* 123(8) (2011) 1930-1935.

[127] H. Yuk, S. Lin, C. Ma, M. Takaffoli, N.X. Fang, X. Zhao, Hydraulic hydrogel actuators and robots optically and sonically camouflaged in water, *Nat. Commun.* 8 (2017) 14230.

[128] C. Liu, H. Qin, P. Mather, Review of progress in shape-memory polymers, *J. Mater. Chem.* 17(16) (2007) 1543-1558.

[129] Y. Bar-Cohen, *Electroactive polymer (EAP) actuators as artificial muscles: reality, potential, and challenges*, SPIE press2004.

[130] Y. Osada, H. Okuzaki, H. Hori, A polymer gel with electrically driven motility, *Nature* 355(6357) (1992) 242-244.

[131] M. Shahinpoor, Y. Bar-Cohen, J. Simpson, J. Smith, Ionic polymer-metal composites (IPMCs) as biomimetic sensors, actuators and artificial muscles-a review, *Smart Mater. Struct.* 7(6) (1998) R15.

[132] M.L. O'Grady, P.-l. Kuo, K.K. Parker, Optimization of electroactive hydrogel actuators, *ACS Appl. Mater. Interfaces* 2(2) (2009) 343-346.

[133] G.H. Kwon, J.Y. Park, J.Y. Kim, M.L. Frisk, D.J. Beebe, S.H. Lee, Biomimetic soft multifunctional miniature aquabots, *Small* 4(12) (2008) 2148-2153.

[134] C. Yang, Z. Liu, C. Chen, K. Shi, L. Zhang, X.-J. Ju, W. Wang, R. Xie, L.-Y. Chu, Reduced Graphene Oxide-Containing Smart Hydrogels with Excellent Electro-Response and Mechanical Properties for Soft Actuators, *ACS Appl. Mater. Interfaces* 9(18) (2017) 15758-15767.

[135] Zolfagharian, A.Z. Kouzani, S.Y. Khoo, B. Nasri-Nasrabadi, A. Kaynak, Development and analysis of a 3D printed hydrogel soft actuator, *Sens. Actuators A: Phys.* 265 (2017) 94-101.

[136] D. Morales, E. Palleau, M.D. Dickey, O.D. Velev, Electro-actuated hydrogel walkers with dual responsive legs, *Soft Matter* 10(9) (2014) 1337-1348.

[137] S.E. Bakarich, R. Gorkin, G.M. Spinks, 4D printing with mechanically robust, thermally actuating hydrogels, *Macromol. Rapid Commun.* 36(12) (2015) 1211-1217.

[138] C.B. Highley, C.B. Rodell, J.A. Burdick, Direct 3D printing of shear-thinning hydrogels into self-healing hydrogels, *Adv. Mater.* 27(34) (2015) 5075-5079.

[139] D.P. Browe, C. Wood, M.T. Sze, K.A. White, T. Scott, R.M. Olabisi, J.W. Freeman, Characterization and optimization of actuating poly (ethylene glycol) diacrylate/acrylic acid hydrogels as artificial muscles, *Polymer* 117 (2017) 331-341.

[140] P.J. Flory, *Principles of polymer chemistry*, Cornell University Press1953.

[141] Y. Li, Y. Sun, Y. Xiao, G. Gao, S. Liu, J. Zhang, J. Fu, Electric Field Actuation of Tough Electroactive Hydrogels Cross-Linked by Functional Triblock Copolymer Micelles, *ACS Appl. Mater. Interfaces* 8(39) (2016) 26326-26331.

[142] J. Choi, M.F. Rubner, Influence of the degree of ionization on weak polyelectrolyte multilayer assembly, *Macromolecules* 38(1) (2005) 116-124.

[143] Gibson, *Additive Manufacturing Technologies 3D Printing, Rapid Prototyping, and Direct Digital Manufacturing, 2nd ed. 2015. ed*., Springer New York :, New York, NY, 2015.

[144] P.S. Bass, L. Zhang, Z.-Y. Cheng, Time-dependence of the electromechanical bending actuation observed in ionic-electroactive polymers, *J. Adv. Dielectr.* 7(02) (2017) 1720002.

[145] J. Fei, Z. Zhang, L. Gu, Bending behaviour of electroresponsive poly (vinyl alcohol)/poly (acrylic acid) semi-interpenetrating network hydrogel fibres under an electric stimulus, *Polym. Int.* 51(6) (2002) 502-509.

[146] T. Tanaka, Kinetics of phase transition in polymer gels, *Phys. A* 140(1-2) (1986) 261-268.

[147] T. Tanaka, D.J. Fillmore, Kinetics of swelling of gels, *J. Chem. Phys* 70(3) (1979) 1214-1218.

[148] C.L. Huffard, F. Boneka, R.J. Full, Underwater bipedal locomotion by octopuses in disguise, *Science* 307(5717) (2005) 1927-1927.

[149] L. Ionov, Biomimetic Hydrogel-Based Actuating Systems, *Adv. Funct. Mater.* 23(36) (2013) 4555-4570.

[150] Richter, S. Klatt, G. Paschew, C. Klenke, Micropumps operated by swelling and shrinking of temperature-sensitive hydrogels, *Lab Chip* 9(4) (2009) 613-618.

[151] F. Benito-Lopez, M. Antoñana-Díez, V.F. Curto, D. Diamond, V. Castro-López, Modular microfluidic valve structures based on reversible thermoresponsive ionogel actuators, *Lab Chip* 14(18) (2014) 3530-3538.

[152] T. Hoare, J. Santamaria, G.F. Goya, S. Irusta, D. Lin, S. Lau, R. Padera, R. Langer, D.S. Kohane, A magnetically triggered composite membrane for on-demand drug delivery, *Nano lett.* 9(10) (2009) 3651-3657.

[153] G. Fundueanu, M. Constantin, P. Ascenzi, Preparation and characterization of pH-and temperature-sensitive pullulan microspheres for controlled release of drugs, *Biomaterials* 29(18) (2008) 2767-2775.

[154] S. Schmidt, M. Zeiser, T. Hellweg, C. Duschl, A. Fery, H. Möhwald, Adhesion and mechanical properties of PNIPAM microgel films and their potential use as switchable cell culture substrates, *Adv. Funct. Mater*. 20(19) (2010) 3235-3243.

[155] Z. Liang, C. Liu, L. Li, P. Xu, G. Luo, M. Ding, Q. Liang, Double-Network Hydrogel with Tunable Mechanical Performance and Biocompatibility for the Fabrication of Stem Cells-Encapsulated Fibers and 3D Assemble, *Sci. Rep*. 6 (2016).

[156] J. Kim, J.A. Hanna, M. Byun, C.D. Santangelo, R.C. Hayward, Designing responsive buckled surfaces by halftone gel lithography, *Science* 335(6073) (2012) 1201-1205.

[157] Z. Hu, X. Zhang, Y. Li, Synthesis and application of modulated polymer gels, *Science* 269(5223) (1995) 525.

[158] E. Lee, D. Kim, H. Kim, J. Yoon, Photothermally driven fast responding photo-actuators fabricated with comb-type hydrogels and magnetite nanoparticles, *Sci. Rep*. 5 (2015).

[159] D. Kim, H.S. Lee, J. Yoon, Highly bendable bilayer-type photo-actuators comprising of reduced graphene oxide dispersed in hydrogels, *Sci. Rep*. 6 (2016).

[160] X.-Z. Zhang, X.-D. Xu, S.-X. Cheng, R.-X. Zhuo, Strategies to improve the response rate of thermosensitive PNIPAAm hydrogels, *Soft Matter* 4(3) (2008) 385-391.

[161] J. Kim, J.A. Hanna, R.C. Hayward, C.D. Santangelo, Thermally responsive rolling of thin gel strips with discrete variations in swelling, *Soft Matter* 8(8) (2012) 2375-2381.

[162] K. Williams, J. Maxwell, K. Larsson, M. Boman, Freeform fabrication of functional microsolenoids, electromagnets and helical springs using high-pressure laser chemical vapor deposition, Micro Electro Mechanical Systems, 1999. *MEMS'99. Twelfth IEEE International Conference on, IEEE*, 1999, pp. 232-237.

[163] Cohen, G. Zhang, F.-G. Tseng, U. Frodis, F. Mansfeld, P. Will, EFAB: rapid, low-cost desktop micromachining of high aspect ratio true 3-D MEMS, Micro Electro Mechanical Systems, 1999. *MEMS'99. Twelfth IEEE International Conference on, IEEE*, 1999, pp. 244-251.

[164] X. Zhang, X. Jiang, C. Sun, Micro-stereolithography of polymeric and ceramic microstructures, *Sens. Actuators, A* 77(2) (1999) 149-156.

[165] R. Gauvin, Y.-C. Chen, J.W. Lee, P. Soman, P. Zorlutuna, J.W. Nichol, H. Bae, S. Chen, A. Khademhosseini, Microfabrication of complex porous tissue engineering scaffolds using 3D projection stereolithography, *Biomaterials* 33(15) (2012) 3824-3834.

[166] D. Han, C. Yang, N.X. Fang, H. Lee, Rapid multi-material 3D printing with projection micro-stereolithography using dynamic fluidic control, *Addit. Manuf.* 27 (2019) 606-615.

[167] S.A. Chester, L. Anand, A thermo-mechanically coupled theory for fluid permeation in elastomeric materials: application to thermally responsive gels, *J. Mech. Phys. Solids* 59(10) (2011) 1978-2006.

[168] Z. Zhao, J. Wu, X. Mu, H. Chen, H.J. Qi, D. Fang, Desolvation induced origami of photocurable polymers by digit light processing, *Macromol. Rapid Commun*. 38(13) (2017) 1600625.

[169] Z. Zhao, J. Wu, X. Mu, H. Chen, H.J. Qi, D. Fang, Origami by frontal photopolymerization, *Sci. Adv*. 3(4) (2017) e1602326.

[170] Y. Hara, R. Yoshida, Influence of a Positively Charged Moiety on Aggregation‐Disaggregation Self‐Oscillation Induced by the BZ Reaction, *Macromol. Chem. Phys.* 210(24) (2009) 2160-2166.

[171] H. van der Linden, W. Olthuis, P. Bergveld, An efficient method for the fabrication of temperature-sensitive hydrogel microactuators, *Lab Chip* 4(6) (2004) 619-624.

[172] Yannas, J. Burke, D. Orgill, E. Skrabut, Wound tissue can utilize a polymeric template to synthesize a functional extension of skin, *Science* 215(4529) (1982) 174-176.

[173] J.-W. Jeong, J.G. McCall, G. Shin, Y. Zhang, R. Al-Hasani, M. Kim, S. Li, J.Y. Sim, K.-I. Jang, Y. Shi, Wireless optofluidic systems for programmable in vivo pharmacology and optogenetics, *Cell* 162(3) (2015) 662-674.

[174] S.I. Park, D.S. Brenner, G. Shin, C.D. Morgan, B.A. Copits, H.U. Chung, M.Y. Pullen, K.N. Noh, S. Davidson, S.J. Oh, Soft, stretchable, fully implantable miniaturized optoelectronic systems for wireless optogenetics, *Nat. biotechnol.* 33(12) (2015) 1280.

[175] G.M. Whitesides, The origins and the future of microfluidics, *Nature* 442(7101) (2006) 368.

[176] B.P. Casavant, E. Berthier, A.B. Theberge, J. Berthier, S.I. Montanez-Sauri, L.L. Bischel, K. Brakke, C.J. Hedman, W. Bushman, N.P. Keller, Suspended microfluidics, *Proc. Natl. Acad. Sci.* 110(25) (2013) 10111-10116.

[177] L. Dong, A.K. Agarwal, D.J. Beebe, H. Jiang, Adaptive liquid microlenses activated by stimuli-responsive hydrogels, *Nature* 442(7102) (2006) 551.

[178] M. Choi, J.W. Choi, S. Kim, S. Nizamoglu, S.K. Hahn, S.H. Yun, Light-guiding hydrogels for cell-based sensing and optogenetic synthesis in vivo, *Nat. photonics* 7(12) (2013) 987.

[179] M. Choi, M. Humar, S. Kim, S.H. Yun, Step-index optical fiber made of biocompatible hydrogels, Adv. Mater. 27(27) (2015) 4081-4086.

[180] D.-H. Kim, J.-H. Ahn, W.M. Choi, H.-S. Kim, T.-H. Kim, J. Song, Y.Y. Huang, Z. Liu, C. Lu, J.A. Rogers, Stretchable and foldable silicon integrated circuits, *Science* 320(5875) (2008) 507-511.

[181] J.A. Rogers, T. Someya, Y. Huang, Materials and mechanics for stretchable electronics, *science* 327(5973) (2010) 1603-1607.

[182] S. Xu, Y. Zhang, L. Jia, K.E. Mathewson, K.-I. Jang, J. Kim, H. Fu, X. Huang, P. Chava, R. Wang, Soft microfluidic assemblies of sensors, circuits, and radios for the skin, *Science* 344(6179) (2014) 70-74.

[183] B.C.-K. Tee, A. Chortos, A. Berndt, A.K. Nguyen, A. Tom, A. McGuire, Z.C. Lin, K. Tien, W.-G. Bae, H. Wang, A skin-inspired organic digital mechanoreceptor, *Science* 350(6258) (2015) 313-316.

[184] R.F. Shepherd, F. Ilievski, W. Choi, S.A. Morin, A.A. Stokes, A.D. Mazzeo, X. Chen, M. Wang, G.M. Whitesides, Multigait soft robot, *Proceedings of the national academy of sciences* 108(51) (2011) 20400-20403.

[185] S.A. Morin, R.F. Shepherd, S.W. Kwok, A.A. Stokes, A. Nemiroski, G.M. Whitesides, Camouflage and display for soft machines, *Science* 337(6096) (2012) 828-832.

[186] M. Fingerman, Chromatophores, *Physiol. Rev.* 45(2) (1965) 296-339.

[187] G.R. Bell, A.M. Kuzirian, S.L. Senft, L.M. Mäthger, T.J. Wardill, R.T. Hanlon, Chromatophore radial muscle fibers anchor in flexible squid skin, *Invertebr. Biol.* 132(2) (2013) 120-132.

[188] J. Rossiter, B. Yap, A. Conn, Biomimetic chromatophores for camouflage and soft active surfaces, *Bioinspir. Biomim.* 7(3) (2012) 036009.

[189] L.M. Mäthger, E.J. Denton, N.J. Marshall, R.T. Hanlon, Mechanisms and behavioural functions of structural coloration in cephalopods, *J. R. Soc. Interface* (2008) S149-S163.

[190] R.A. Cloney, E. Florey, Ultrastructure of cephalopod chromatophore organs, *Cell Tissue Res.* 89(2) (1968) 250-280.

[191] E. Kreit, L.M. Mäthger, R.T. Hanlon, P.B. Dennis, R.R. Naik, E. Forsythe, J. Heikenfeld, Biological versus electronic adaptive coloration: how can one inform the other?, *J. R. Soc. Interface* 10(78) (2013) 20120601.

[192] Q. Wang, G.R. Gossweiler, S.L. Craig, X. Zhao, Cephalopod-inspired design of electro-mechano-chemically responsive elastomers for on-demand fluorescent patterning, *Nat. Commun.* 5 (2014) 4899.

[193] Y. Liu, K. Ai, J. Liu, M. Deng, Y. He, L. Lu, Dopamine-melanin colloidal nanospheres: an efficient near-infrared photothermal therapeutic agent for in vivo cancer therapy, *Adv. Mater.* 25(9) (2013) 1353-1359.

[194] Y. Ding, M. Floren, W. Tan, Mussel-inspired polydopamine for bio-surface functionalization, *Biosurf. Biotribol.* 2(4) (2016) 121-136.

[195] Y. Wu, K. Wang, S. Huang, C. Yang, M. Wang, Near-infrared light-responsive semiconductor polymer composite hydrogels: spatial/temporal-controlled release via a photothermal "sponge" effect, *ACS Appl. Mater. Interfaces* 9(15) (2017) 13602-13610.

[196] L. Han, Y. Zhang, X. Lu, K. Wang, Z. Wang, H. Zhang, Polydopamine nanoparticles modulating stimuli-responsive PNIPAM hydrogels with cell/tissue adhesiveness, *ACS Appl. Mater. Interfaces* 8(42) (2016) 29088-29100.

[197] P. Kord Forooshani, B.P. Lee, Recent approaches in designing bioadhesive materials inspired by mussel adhesive protein, *J. Polym. Sci., Part A: Polym. Chem.* 55(1) (2017) 9-33.

[198] X. Zhao, Multi-scale multi-mechanism design of tough hydrogels: building dissipation into stretchy networks, *Soft matter* 10(5) (2014) 672-687.

[199] T. Nakajima, N. Takedomi, T. Kurokawa, H. Furukawa, J.P. Gong, A facile method for synthesizing free-shaped and tough double network hydrogels using physically crosslinked poly (vinyl alcohol) as an internal mold, *Polym. Chem.* 1(5) (2010) 693-697.

[200] J. Saito, H. Furukawa, T. Kurokawa, R. Kuwabara, S. Kuroda, J. Hu, Y. Tanaka, J.P. Gong, N. Kitamura, K. Yasuda, Robust bonding and one-step facile synthesis of tough hydrogels with desirable shape by virtue of the double network structure, *Polym. Chem.* 2(3) (2011) 575-580.

[201] Q. Chen, L. Zhu, C. Zhao, Q. Wang, J. Zheng, A robust, one-pot synthesis of highly mechanical and recoverable double network hydrogels using thermoreversible sol-gel polysaccharide, *Adv. Mater.* 25(30) (2013) 4171-4176.

[202] M.A. Haque, T. Kurokawa, G. Kamita, J.P. Gong, Lamellar bilayers as reversible sacrificial bonds to toughen hydrogel: hysteresis, self-recovery, fatigue resistance, and crack blunting, *Macromolecules* 44(22) (2011) 8916-8924.

[203] J.-Y. Sun, X. Zhao, W.R. Illeperuma, O. Chaudhuri, K.H. Oh, D.J. Mooney, J.J. Vlassak, Z. Suo, Highly stretchable and tough hydrogels, *Nature* 489(7414) (2012) 133.

[204] M. Zhong, Y.-T. Liu, X.-Y. Liu, F.-K. Shi, L.-Q. Zhang, M.-F. Zhu, X.-M. Xie, Dually cross-linked single network poly (acrylic acid) hydrogels with superior mechanical properties and water absorbency, *Soft Matter* 12(24) (2016) 5420-5428.

[205] G. Ma, C. Wu, Microneedle, bio-microneedle and bio-inspired microneedle: A review, *J. Controlled Release* 251 (2017) 11-23.

[206] A.M. Hetherington, F.I. Woodward, The role of stomata in sensing and driving environmental change, *Nature* 424(6951) (2003) 901.